Evolution of the hydrothermal system and ore mineralization in the Southwest prospect, in the vicinity of the Santo Tomas II deposit, Baguio district, Philippines

フィリピン Baguio 地域、Santo Tomas Ⅱ鉱床近傍、
Southwest 鉱徴地における熱水系の進化と鉱化作用

2020

Cirineo Avriel Venis Literal

6517102

秋田大学
Akita University

秋田大学大学院

国際資源学研究科博士後期課程

資源学専攻

Abstract

The Baguio district is a premiere gold and copper district in the Philippines known to host numerous porphyry copper, epithermal gold and skarn deposits, including the Santo (Sto.) Tomas II deposit, a 60-year old block-caving mine being operated by Philex Mining Corporation. Recent exploration activities uncovered the occurrence of porphyry-type veinlets that overprinted the complex of porphyry intrusions and breccia facies in the Southwest prospect. A yet to be established genetic connections of this porphyry-type veinlets to the Sto. Tomas II deposit may postulate the occurrence of supposedly blind porphyry copper deposits, thus it is significant to establish a genetic model of the Southwest prospect in the understanding of the porphyry copper deposits in the southern Baguio district. The prospect is located at the southwestern periphery of the Sto. Tomas II orebody, which hosts a copper-gold mineralization related to a complex of porphyry intrusions, breccia facies and overlapping porphyry-type veinlets emplaced within the basement metavolcanics rocks of the Pugo Formation and conglomerates of the Zigzag Formation.

The complex is composed of at least four broadly petrographically similar dioritic intrusive rocks that vary in texture and alteration type and intensity. Arranged in chronological order, they are the: (1) coarse-grained biotite quartz diorite (ODP – Old Diorite Porphyry), (2) fine-grained quartz diorite porphyry (EMD - Early Mineralization Diorite), (3) medium-grained porphyritic hornblende quartz diorite (LD – Late Diorite) and (4) hornblende andesite porphyry (DP – Diorite Porphyry). These intrusions were accompanied with at least five breccia facies, namely, (1) PMBx1 - Phreatomagmatic Breccia Facies 1, (2) PMBx2a - Phreatomagmatic Facies 2a, (3) PMBx2b - Phreatomagmatic Breccia Facies 2b, (4) EMDBx - Early Mineralization Diorite Breccia

and (5) DPBx - Diorite Porphyry Breccia. The breccia facies overlapped the intrusions and recorded several brecciation episodes that involved explosive brecciation induced by phreatomagmatic activities that reflected the varying pressure-temperature conditions in magmatic-hydrothermal system during the emplacement of the various intrusions. Various quartz-bearing veinlet assemblages overprinted the pre-, syn- and late-mineralization porphyry intrusions and breccia facies but are also present as quartz vein fragments in the breccia facies.

Hydrothermal alteration assemblages consisting of potassic, chlorite-magnetite, propylitic and sericite-chlorite alteration, and contemporaneous veinlet types were developed on the host rocks. Potassic alteration is characterized by secondary biotite-quartz-magnetite- anhydrite-chalcopyrite-bornite. Secondary biotite is the dominant alteration mineral present as fine disseminations in the groundmass and as polygrain aggregates completely altering former ferromagnesian minerals, such as hornblende. It is often accompanied with quartz, anhydrite, magnetite and copper iron sulfides. Chlorite-magnetite alteration overprinted the potassic alteration. It is defined by the assemblage of sericite-chlorite-carbonate- magnetite±K-feldspar and abundant chalcopyrite-magnetite-chlorite-actinolite±sericite veinlets. Propylitic alteration is exhibited by LD. It is characterized by chlorite-epidote-calcite±illite. The shallower portions dominated by the PMBx2a and PMBx2b were altered by chlorite-illite-pyrite±chalcopryite with associated quartz-gypsum cement. Elevated copper and gold grades are present in the (1) chalcopyrite-bornite assemblage in the potassic alteration in the syn-mineralization EMD and contemporaneous veinlets including the sheeted quartz veinlets and (2) chalcopyrite-rich mineralization associated with the chalcopyrite-magnetite -chlorite-

actinolite±sericite veinlets contemporaneous with the chlorite-magnetite alteration. Erratic remarkable concentrations of gold were also present in the late-mineralization LD.

High X_{Mg} of calcic amphiboles (>0.60) in the intrusive rocks indicates that the magmas have been in oxidizing conditions since the early stages of crystallization, while a gap in the of Al content between the rims and the cores of the calcic amphiboles in the EMD and LD indicates decompression during the crystallization of these intrusive rocks from the magmas. Meanwhile, X_{Mg} of secondary biotites and chlorites are also high (>0.70) with low to undetectable Cl and F contents.

Fluid inclusion microthermometry suggests the trapping of fluids that formed the potassic alteration, associated ore mineralization and sheeted quartz veinlets within the subcritical immiscible region at pressures between 50 and 30 MPa and temperatures between 554 and 436 °C, at depths between 1.9 km and 1.1 km. Temperature data from the biotite and chlorite geothermometers indicate that the chalcopyrite-rich mineralization associated with the chlorite-magnetite alteration was formed at a much lower temperature (ca. 290 °C) than the potassic alteration dominated by secondary biotite (ca. 470°C).

Evidences from the vein off-setting matrix suggest multiple intrusions within the EMD, despite the K-Ar ages of the potassic alteration in EMD and hornblende in the LD to be of about the same age at 3.5±0.3 Ma. The K-Ar age of the potassic alteration was likely to be thermally reset, as a result of the overprinting hydrothermal activities. Alternatively, these may also indicate that the two events occurred within short time interval. The constrained K-Ar ages also indicate an earlier, if not co-eval intrusive rocks in the Southwest prospect with that of the earliest “dark diorite” intrusion in the Sto. Tomas II. In addition, the range of $\delta^{34}S$ of sulfide minerals from +1.8 ‰ to +5.1 ‰ in the

Southwest prospect closely overlaps with those of the Sto. Tomas II, Clifton and Bumolo porphyry copper deposits and epithermal vein prospects within the vicinity, indicating a homogeneous source of sulfur.

Table of Contents

List of Tables

List of Figures

Acknowledgements

My endless gratitude to my supervisors, Prof. Akira Imai and Prof. Ryohei Takahashi, whose diligent efforts and patience helped me throughout the fulfillment of this study. I would like to express my sincerest gratitude to the Philex Mining Corporation for the permission, logistical support and meaningful discussion throughout the conduct of this study. I am also very thankful to Prof. Andrea Agangi, the Economic Geology Laboratory members and Dr. Hinako Sato for the support during analyses, the kind encouragement and discussion. I am also grateful to the New Frontier Leader Program for Rare-metals and Resources, Akita University, and the Japanese Government Monbukagakusho (MEXT) Scholarships for the funds provided to conduct the analyses. This work was supported by JSPS KAKENHI Grant-in-Aid Number 17K06982, Japan Mining Promotive Foundation, and the Society of Resource Geology.

1 Introduction

1.1 Background

The Baguio district is a major copper and gold producer located in the Northwestern Luzon Island, Philippines with total estimated resource of more than 35 million ounces of gold and 2.7 million tons of copper, accounting for about 97% of all the copper reserves of the Philippines (Clark, 1994; Bureau of Mines and Geosciences, 2004; Waters et al., 2011; Cirineo, 2017). It is well known for its various well-studied hydrothermal ore deposits, such as epithermal gold and skarn deposits, as well as, porphyry copper-gold deposits, which include the Sto. Tomas II deposit (Imai, 2001; Baluda & Galapon, 2005; Waters et al., 2011). However, despite the presence of numerous ore deposits, the Baguio district remains underexplored particularly for porphyry copper type deposits and carries great potential for new discoveries (Water et al., 2011).

Recent efforts by exploration by Philex Mining Corporation (PMC) in the southern tip of the Baguio District unveiled the occurrence of overprinting relationship between the intrusive rocks, diatreme-breccias and porphyry-type veinlets in the Southwest prospect, located within the vicinity of the Sto. Tomas II porphyry copper and gold deposit, a 60-year old block-caving mine being operated my PMC (Philex Mining Corporation, 2017). Such relationship is well-known in the giant Grasberg deposit, the main deposit in the world-class Ertsberg district (MacDonald & Arnold, 1994; Pollard et al., 2005). The complex relationships of intrusive rocks and breccias, and alteration and mineralization were elucidated by several workers (MacDonald & Arnold, 1994, Pollard & Taylor, 2002), and it was argued that the gigantic copper and gold reserves present in the Ertsberg district is due to the emplacement of several short-lived cycles of intrusions,

and one of them is the group of Grasberg intrusions that host the deposit (Pollard et al., 2005).

This work examines the key features of the overlapping intrusive rocks, diatreme-breccias and porphyry-type veinlets and elucidate their spatial and temporal relationships along with the newly presented geochronological data. We conducted fluid inclusion, sulfur isotope and mineral chemistry analyses for the better understanding on fluid evolution and formation of porphyry copper mineralization in the Southwest prospect.

1.2 Geologic outline

The Philippine archipelago is one of the most tectonically active sites in the world, where the Philippine Sea Plate, the Eurasian Plate and the Indo-Australian Plate in the Southeast Asian Margin are actively interacting. Surrounding it is a complex system of subduction zones, collision zones and marginal sea basins, which control the distribution and nature of the belts of insular arcs, ophiolitic rocks, and continental rocks of Eurasian affinity scattered in the archipelago (Aurelio, 2000; Aurelio & Peña, 2004). The oppositely dipping subduction zones surrounding the archipelago are the Manila, Negros, Sulu and Cotabato Trenches, which are situated at the western side, and the Philippine Trench and the East Luzon Trough, situated at the eastern side (Fig. 1). Ancient magmatic arcs are present in various parts of the archipelago. These, however, cannot be connected to any activity of the present-day subduction zones, indicating that magmatism has long been active throughout the Cenozoic. (Aurelio & Peña, 2004). Magmatism has been attributed to the eastward consumption of the Eurasian Plate under the Manila Trench since the late Oligocene (Hollings et al., 2011), which led to the emplacement of intrusive complexes with intermediate to acidic compositions composing the ancient western Luzon magmatic arc (Mitchell & Leach, 1991; Imai, 2001, 2002; Queaño et al., 2007;

Hollings et al., 2011). Porphyry copper deposits and epithermal gold deposits make up most of the gold districts in the Philippines, typically coinciding with the magmatic arcs, such as in the northwestern portion of the Luzon island, wherein a belt of porphyry copper deposits (Sillitoe & Gappe, 1984; Imai, 2000a, 2000b) that includes the porphyry copper deposits in the Mankayan and Baguio Districts, in the central western Luzon, such as the Dizon deposit (Malihan, 1982; Imai, 2005) and in southwestern Luzon, such as the Taysan deposit (Wolfe et al., 1978; Imai, 2000a, 2000b, 2001) was formed (Fig.1).

The northwest-ward oblique convergence of the Philippine Sea Plate and east margin of the Eurasian Plate resulted in an interpreted collision suture represented by a group of left-lateral strike-slip faults that traverses the axis of Luzon down to Mindanao for more than 1200km termed as the Philippine Fault or Philippine Fault Zone (PFZ) (Rangin, 1991, Aurelio, 2000).

The Baguio District hosts a number of porphyry copper, epithermal and skarn deposits and mineralization (Fig. 2). A few notable examples are the Sto. Tomas II, Bumolo, Black Mountain and Ampucao porphyry copper deposits, Mexico and Thanksgiving skarn deposits and Acupan and Baguio Gold epithermal deposits. Moreover, porphyry copper deposits are observed to be overlapped by epithermal deposits in the Baguio District as a result of rapid uplift and unroofing (Imai, 2000b, 2001; Waters et al., 2011). Waters et al. (2011) described that the rapid uplift was caused by the transpression on the major retraining bend of the PFZ situated south of Baguio, enhanced by the compressional tectonism that occurred when the subduction is shallowing in the Manila Trench. Rapid uplift is also the reason of the scarcity of volcanic landforms in the district (Imai, 2000a, 2001).

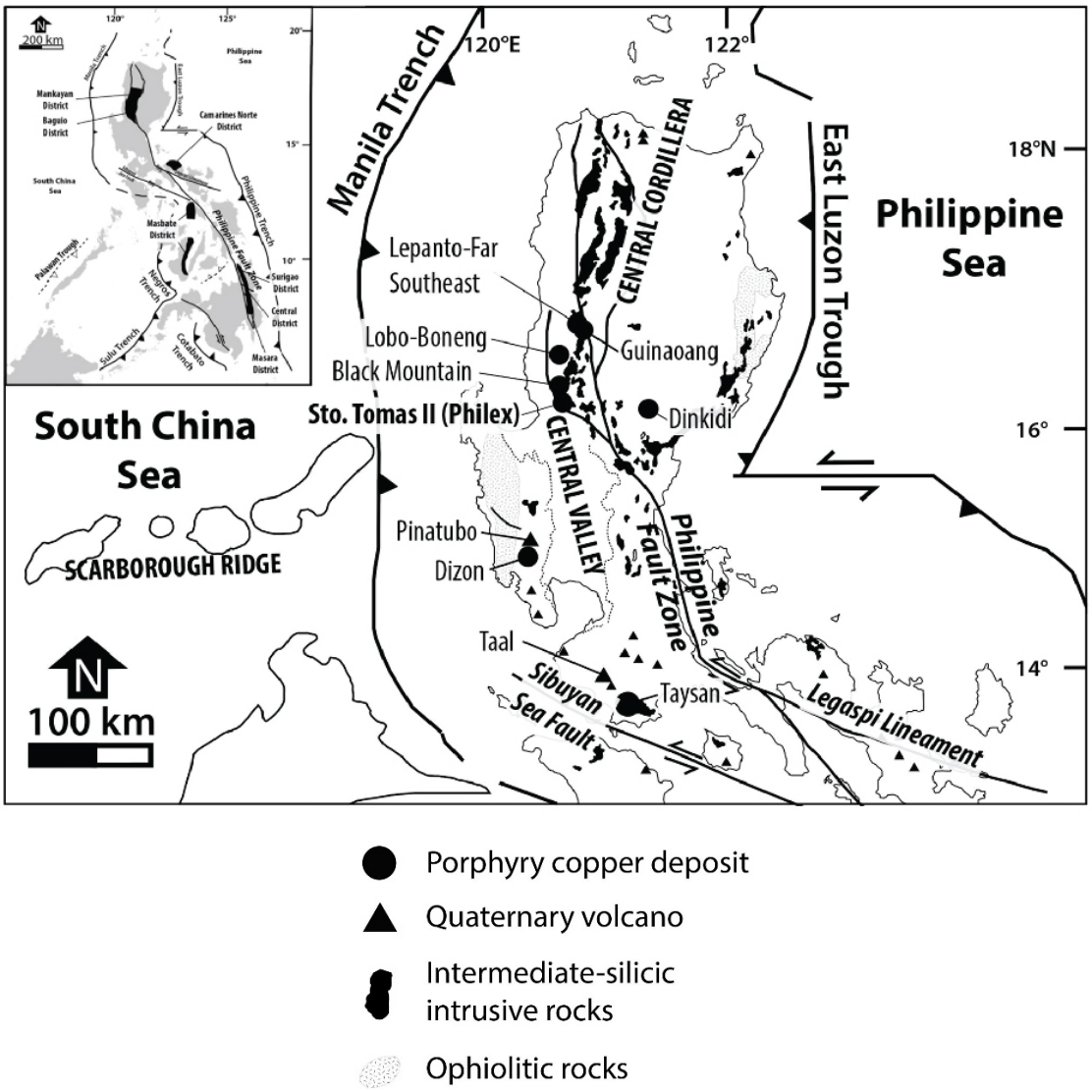

Fig. 1 Map showing the location of the porphyry copper deposits associated with intermediate-silicic intrusive rocks in the northern Luzon, as well as the distribution of major structures, quaternary volcanoes and ophiolitic complexes. Inset shows the location of the major gold districts in the Philippines that host numerous epithermal and other gold deposits are also shown. Modified after Mitchelle and Leach (1991), Mines and Geosciences Bureau (2004), Imai (2001).

The Baguio District is underlain by the basement rocks composed of mafic to intermediate volcaniclastic, volcanic and sedimentary rocks that had undergone greenschist facies metamorphism (Fig. 2). These rocks constitute the Eocene to Oligocene Pugo Formation (Serafica & Baluda, 1977; Aurelio, 2000; Peña, 2008). It is overlain uncomformably by sedimentary sequences consisting of (1) the Oligocene to middle Miocene Zigzag Formation composed of conglomerates, sandstones, shales and andesitic lavas, (2) early to middle Miocene Kennon Formation composed of massive gray biothermal limestones, (3) middle Miocene Klondye Formation consisting of conglomerates with interbedded finer grained sedimentary and volcaniclastic rocks, and lastly by (4) Miocene to Pliocene Mirador Limestone (Fig. 2) (Peña, 2008).

At least two major magmatic events resulted in the emplacement of intrusive complexes scattered all over the district. The batholithic early Miocene Central Cordillera Diorite Complex (CCDC), flanked at the eastern edge of the district (Fig. 2) was generated by the eastward subduction of the South China Sea plate, and is coeval with the potassic and calc-alkaline plutons further to the east, in the back-arc basin of the Cagayan Valley (Hollings et al., 2011; Wolfe & Cooke, 2011). This eastward subduction is inferred to have been initiated by the northeastward propagation of the North Borneo-Manila Trench at approximately 40 Ma (Aurelio, 2000). The CCDC represents the ancient magmatic arc that was overlapped by present-day volcanic arc in the Baguio District, along with intrusions with copper mineralization dated 14.9±0.5Ma in the Tapaya prospect (Mitani, 2013) and porphyry copper deposits located north of the Baguio District, such as the Lobo-Boneng (10.5±0.4Ma) and Santo Niño (9.5±0.3Ma) (Imai, 2002). This magmatism was ceased temporarily by the supposed flattening of a down-going slab in the subduction zone (Hollings et al., 2011).

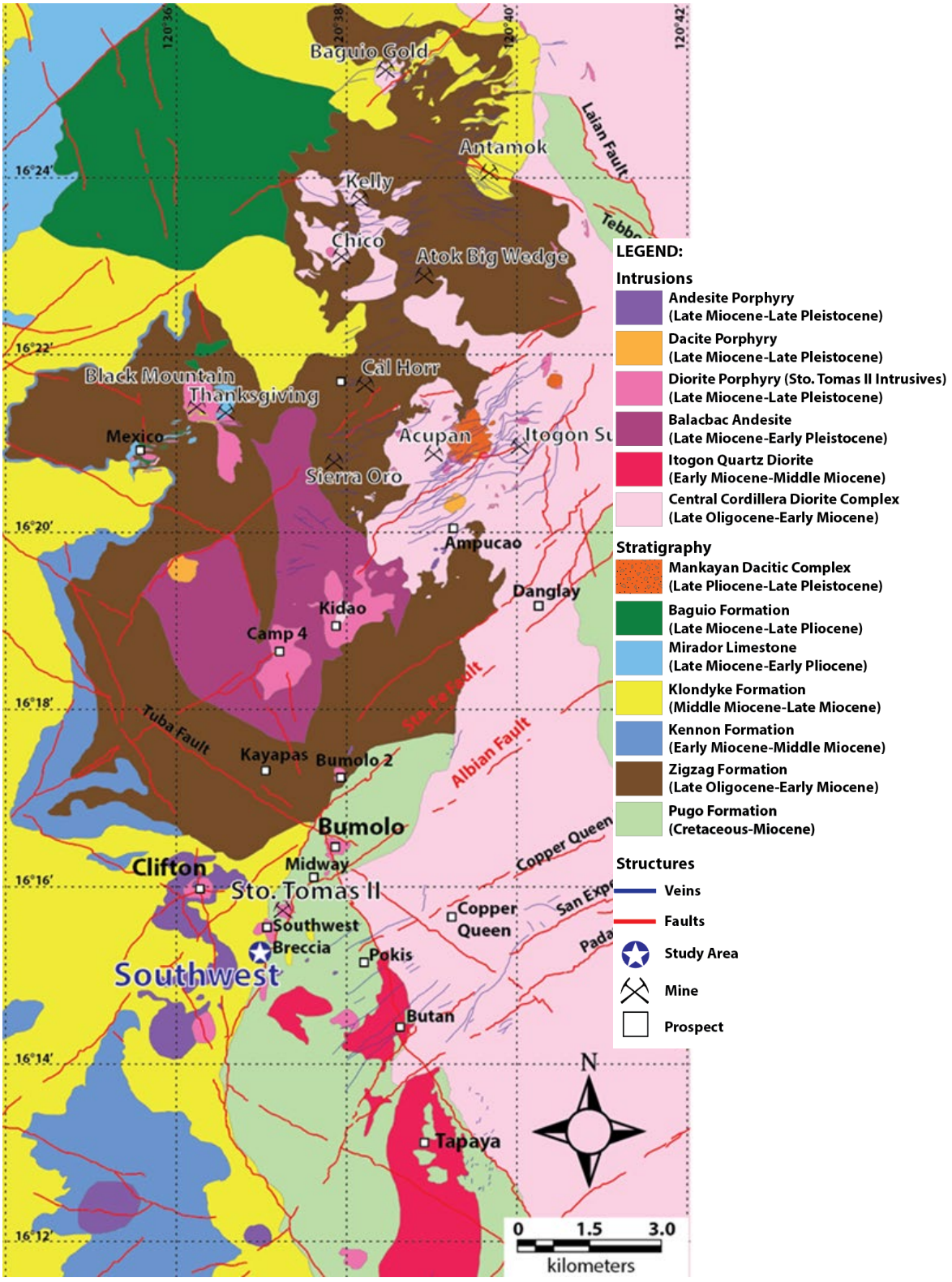

Fig. 2 Geologic Map of the Baguio District. Modified from Waters et al. (2011), Philex Mining Corporation (Unpublished). Location of the Southwest prospect is indicated by the "star" symbol and red font color.

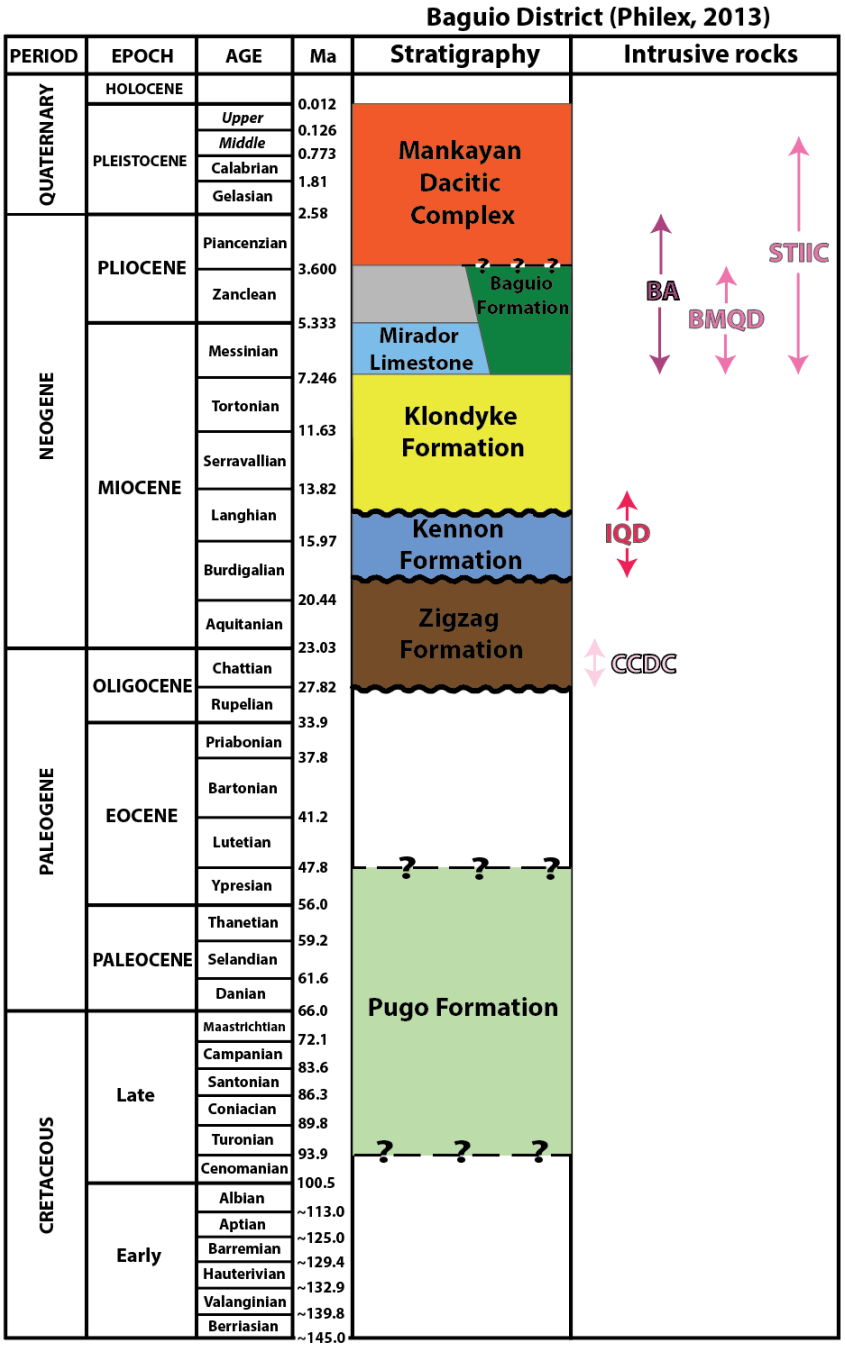

Note:
CCDC - Central Cordillera Diorite Complex;
IQD - Itogon Quartz Diorite;
BA - Balacbac Andesite;
BMQD - Black Mountain Quartz Diorite;
STIIC - Sto. Tomas II Cluster

Fig. 3 Generalized stratigraphic column of the Baguio District modified from Aurelio and Pena, 2014 and adopted from Philex Mining Corporation (Unpublished).

Intrusion of smaller porphyry stocks during the middle Miocene to Pleistocene succeeded the cessation of magmatism (Fig., 3; Imai, 2002; Hollings et al., 2011; Water et al., 2011). Some of these intrusive rocks are thought to the causative intrusions of porphyry copper mineralization (Balce, 1979; Balce et al., 1980; Serafica et al., 1977; Mitchell & Balce, 1990). Results from various radiometric dating methods indicated that copper-gold mineralization related to these intrusions initially occurred between 3.2 and 2.6 Ma (Waters et al., 2011). These intrusions are also thought to be responsible for the initiation of the Plio-Pleistocene epithermal systems and associated advanced argillic alteration in the district (e.g. Mitchell & Balce, 1990; Aoki et al., 1993; Imai, 2002). Nevertheless, several workers have also invoked the possibility of younger porphyry copper-gold systems beneath the district to initiate the hydrothermal systems at the shallow levels (Waters et al., 2011; Cooke et al., 2011). Notable examples provided were the occurrence of "intermediate sulfidation calcite-quartz veins" overprinting the high temperature "quartz-magnetite-sulfide veins" at the Baguio Gold deposit, and the widespread and extensive potassic alteration at the deep portions in the vicinity of the Ampucao prospect and potassic-altered diorite porphyry clasts in the Balatoc Diatreme (Cooke et al., 2011).

1.3 Structural controls on porphyry copper mineralization

The interplay of the branches of the PFZ, Tebbo and Tuba Faults, play a major role in the emplacement of copper and gold deposits in the Baguio District (Balce, 1979; Fernandez & Damasco, 1979). The Baguio District is situated in a zone just above the northward bending of the northern arm of the PFZ, and directly northeast of the intersection of the Scarborough Ridge and Manila Trench (Cooke & Berry, 1996; Aurelio et al., 2009; Waters et al., 2011). It was explained that the dominant trans-compressional

stress that was caused by the eastward subduction of the South China Sea Plate under the Manila Trench created a trans-tensional relay zone in between two branches of the PFZ, the Tebbo and Tuba Faults (Aurelio, 2006, 2007a, b, c; Aurelio et al., 2009). Second order NE-trending steeply dipping normal faults with strike slip components became the conduits of mineralized porphyry intrusions, particularly at fault terminations, such as the emplacement of the Sto. Tomas II orebody along the horsetail branches of the Albian Fault, and fault intersections, such as the site of the Clifton prospect along the Sta. Fe and Binang Fault intersection (Fig. 4; Baluda & Galapon, 2005).

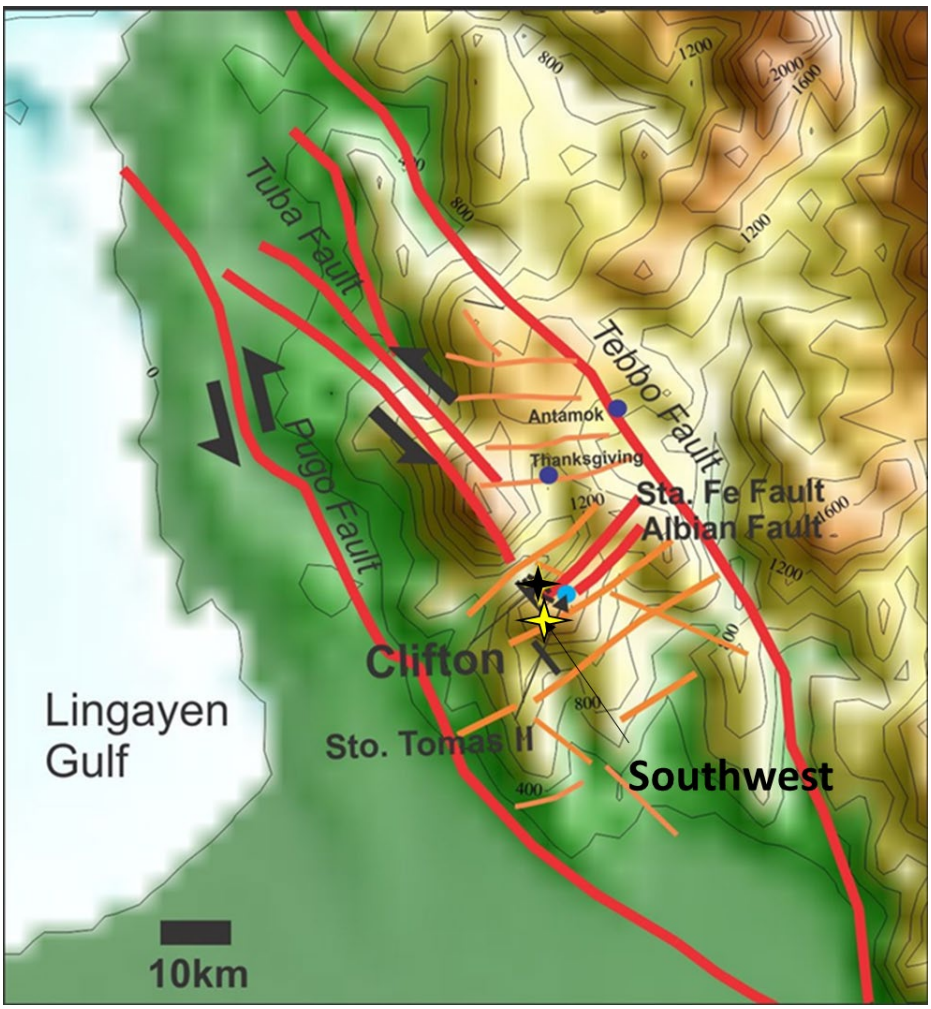

Fig. 4 Composite map of the Baguio District showing the intersecting NW-NE faults related to the NW trending faults of the left lateral Philippine fault. Modified from Philex Mining

Corporation (Unpublished), Wessel and Smith (1991), Sandwell and Smith (1991) and Cirineo (2017). Yellow star indicates the location of the Southwest prospect.

1.4 Porphyry copper-gold mineralization at the Sto. Tomas II vicinity

1.4.1 Sto. Tomas II deposit

Porphyry copper and gold mineralization of the Sto. Tomas II deposit is centered in the potassic altered zone enveloping the main stage intrusive rock that is thought to be the "ore-bringer" termed as the "dark diorite" (Serafica & Baluda, 1977; Imai, 2001; Obial & Cinco; 2013). It was described in petrography as the "ore generating hornblende andesite porphyry" (Imai, 2001). A succession of pulses of intrusion followed and are termed as follows: (1) inter-mineral quartz diorites termed as "clear diorite" or "medium-grained quartz diorite porphyry", (2) the low copper intrusive rock interpreted to be emplaced in the waning stage of porphyry copper emplacement termed as the "andesite porphyry" and "clinopyroxene-bearing hornblende andesite porphyry", (3) and the post-ore "hornblende andesite" that was only observed at the top portion of the deposit (Serafica & Baluda, 1977, Imai, 2001, Obial & Cinco, 2013). This developed concentric ore zones: a doughnut-shaped bornite and chalcopyrite zone accompanied with gold, silver, gold-silver tellurides and palladium-platinum bearing minerals that zone outwards to chalcopyrite-pyrite dominated assemblage, and then to a pyrite-rich fringe. The central portion of the orebody, on the other hand, was intruded by the "andesite porphyry" and resulted to a low copper but gold-bearing zone (Serafica & Baluda, 1977; Tarkian & Koopmann, 1995; Imai, 2001; Obial & Cinco, 2013). A post-mineralization "tonalite" presumably truncated the ore body at depth, resulting in the dilution of the copper and gold grades (Sillitoe & Gappe, 1984). This is exposed at around 900ML of the underground block caving mine and was described as "porphyritic quartz diorite" or "QD"

(Obial & Cinco, 2013). Exploration drilling below the lowest mining level (773ML) recognized another intrusion, termed as "CD2" or "clear diorite phase 2", which is interpreted to as a late-mineralization intrusion distinguished by its chlorite-magnetite±epidote alteration and association with late-stage gold-bearing veinlets (Masangcay et al., 2018).

Reported K-Ar ages on the "dark diorite" are 5.9±1.6 Ma (least altered), 3.8±1.1 Ma (altered) by Togashi et al. (1990), while 1.5±0.4 Ma (least altered) and 1.2±0.3 Ma (altered) by Imai (2001). Waters et al. (2011) reported the age of the hydrothermal biotite in the "intra-mineralization diorite" and "intra-mineralization andesite porphyry" by $^{40}Ar/^{39}Ar$ at 1.48±0.05 Ma and 1.47±0.05 Ma, respectively. Unpublished report on the "porphyritic quartz diorite" indicates an age of 1.06±Ma, placing it the youngest in the succession of intrusive stocks in the Sto. Tomas II deposit. (Obial and Cinco, 2013, Masangcay et al., 2018)

Bornite-chalcopyrite is the principal ore-mineral assemblage in the hydrothermal biotite zone associated with the "dark diorite" and "clear diorite" as described by Serafica and Baluda (1979), Tarkian and Koopmann (1995) and Imai (2001). It is often accompanied with gold, silver, gold-silver tellurides and palladium-platinum bearing minerals. Zoning outwards, mineralization becomes dominated by chalcopyrite-pyrite assemblage, and then to a pyrite-rich fringe. The central portion of the orebody, on the other hand, is intruded by the "andesite porphyry" and results to a low copper but gold bearing zone. Downward zoning along the orebody shows a termination of copper and gold mineralization (Serafica and Baluda, 1977).

Stockwork and sheeted quartz-magnetite veins and veinlets followed the initial hydrothermal biotitization in the Sto. Tomas II deposit and these have been well-developed in between the contacts of the syn- and intra-mineralization intrusions (Imai, 2001). Abundant magnetite grains are accompanied with the quartz veinlets along with scarce chalcopyrite and bornite. Estimated formation temperatures of these veinlets point out near magmatic temperatures on the initial deposition (Imai, 2001). Abundant copper-iron sulfides are associated with anhydrite veinlets that crosscut the stockwork and sheeted quartz-magnetite veinlets, while scarce molybdenite mineralization associated with quartz veinlet and hydrothermal chlorite are present in the central portion of the deposit (Imai, 2001). Gold-rich mineralization closely associated with pyrite hosted in quartz-pyrite-magnetite-chlorite±gypsum veinlets with sphalerite, galena and chalcopyrite, termed as "V3" was recognized below 773ML (Masangcay et al., 2018). Homogenization temperatures of fluid inclusions in quartz range from 300°C to 400°C. This led to the interpretation that these veinlets were deposited during the waning stages of the porphyry mineralization (Masangcay et al., 2018).

1.4.2 Clifton prospect

Porphyry copper and gold mineralization at Clifton is centered on the intrusive complex consisting of at least three intrusive rocks intruding through the basement consisting of volcanic rocks of the Pugo Formation (MA), namely: (1) the Early Andesite Porphyry (EAP), (2) the Intra-mineral Diorite Porphyry (IMD), and (3) the Late Andesite Porphyry (LAP) (Cirineo, 2017). The EAP is equivalent to the hornblende andesite porphyry, the IMD to the hornblende quartz diorite porphyry with medium-grained groundmass and porphyritic hornblende quartz diorite with coarse-grained groundmass, and the LAP to the clinopyroxene-hornblende andesite porphyry of Imai (2001). They

have similar mineralogical compositions and are distinguished through the differences in the textures observed, particularly the size of the groundmass, degree of alteration and density of veinlets. Chalcopyrite and bornite are the principal ore minerals associated with the potassic alteration, which is well-developed in the EAP and its contacts with the metavolcanics rocks. It is accompanied with pervasive hydrothermal biotitization, disseminated grains of magnetite with ilmenite-hematite and sphene, and associated wavy quartz veinlets. Sheeted quartz veinlets with scarce copper-iron sulfide mineralization are recognized in the Clifton prospect. They are abundant in the stockwork zone, located at the central deeper portion of the prospect where the various intrusive phases are intersected (Cirineo, 2017).

1.4.3 Bumolo prospect

The Bumolo prospect also manifests a copper and gold mineralization centered on an intrusive complex consisting of at least two phases of quartz diorites recognized through petrography as the 1) hornblende quartz diorite porphyry and 2) clinopyroxene-bearing porphyritic hornblende quartz diorite with coarse-grained groundmass (Imai, 2001). These intrusive phases are broadly similar texturally and mineralogically to the intra-mineralization intrusions of Sto. Tomas II deposit (Imai, 2001). An andesite porphyry stock most likely similar to that of the “clinopyroxene-bearing hornblende andesite porphyry” was also recognized by drillcore logging, nevertheless, the “ore generating hornblende andesite porphyry” or “dark diorite” was not encountered (Obial & Cinco, 2013). Company reports indicated that the southern part of the prospect was extremely diluted in terms of copper and gold grades by late-mineralization intrusive phases, a case similar to what was being observed in the deeper (below 900ML) of the Sto. Tomas II deposit (Obial & Cinco, 2013; Sillitoe, 2011). However, the northern

portion of the prospect remains open and indicate copper and gold mineralization related to stockwork veining of "ribbon quartz" (Philex Mining Corporation, 2017).

1.4.4 Southwest prospect

The Southwest prospect has been revisited due to its potential to host a copper-gold mineralization. It is located at the southwestern periphery of the Sto. Tomas II deposit, previously known as the Southwest Sto. Tomas II. It was initially composed of the Southwest area and the Southwest Breccia, both of which host supposed diatreme breccia bodies commonly found at the peripheries of a porphyry copper deposit (Obial & Cinco, 2013). Exploration on these areas was only recently opened due to the access restrictions albeit the proximity to the existing Sto. Tomas II mine. Nevertheless, a closer examination on the Southwest Breccia determined that the diatreme breccia body was instead an altered conglomerate layer overlying the basement MA. This led to the redirection of exploration activities to the Southwest area. The diatreme breccia body is composed of a rock flour matrix with potassic alteration accompanied with low copper and gold grades. The clasts are made up of andesite volcanic rocks, and various diorite and andesite porphyries (Sillitoe, 2011; Obial & Cinco, 2013).

Results from the recent exploration activities resulted in the further characterization in the Southwest prospect as overlapping phases of intrusive rocks, breccia units, and mineralized quartz veins. Its footprint of copper and gold mineralization is positioned in between approximately 1400masl and 850masl, roughly at the same elevation as that of Sto. Tomas II deposit. The overlapping intrusive rocks, breccia units and mineralized quartz veins were emplaced in the conglomerate, which is believed to be a member of the Zigzag Formation due to the absence of carbonaceous clasts and meta-volcanic rocks of Pugo Formation.

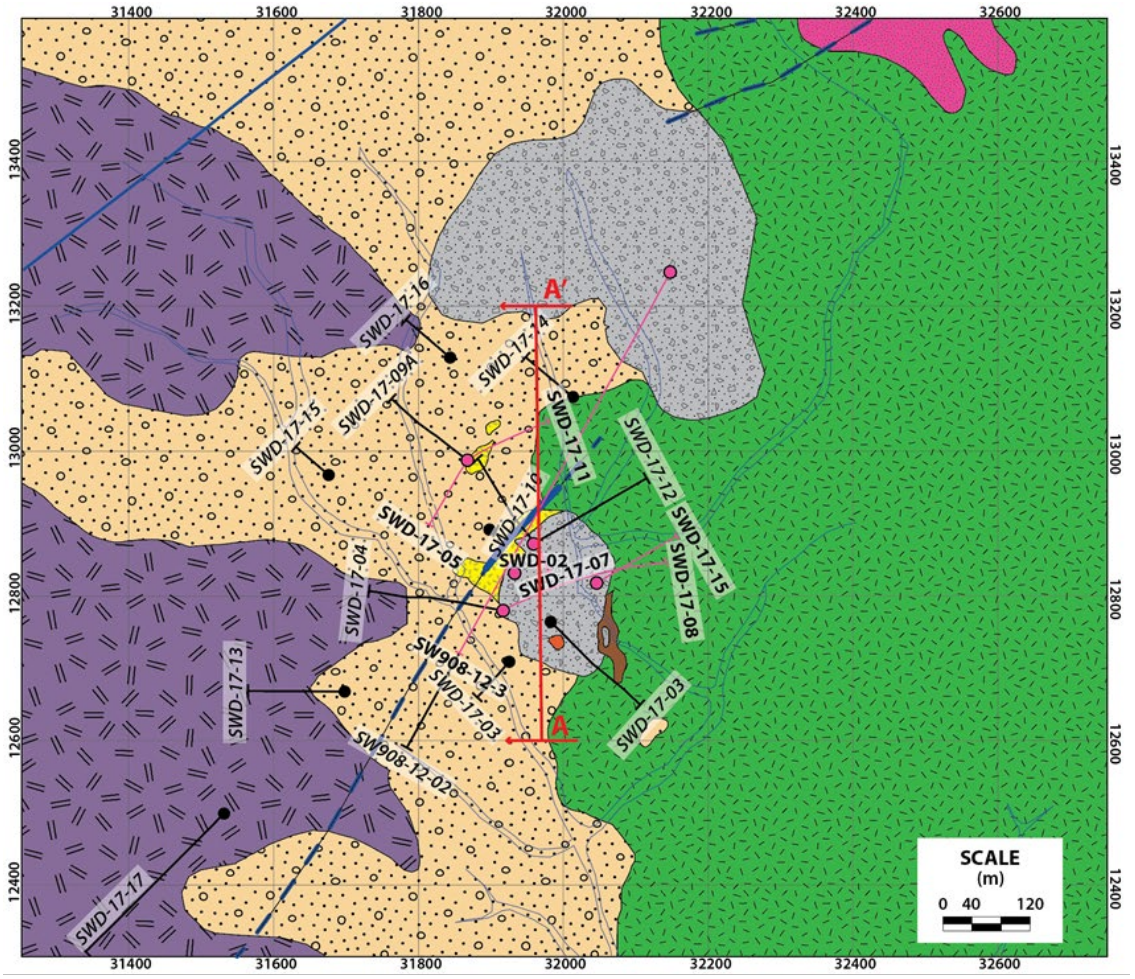

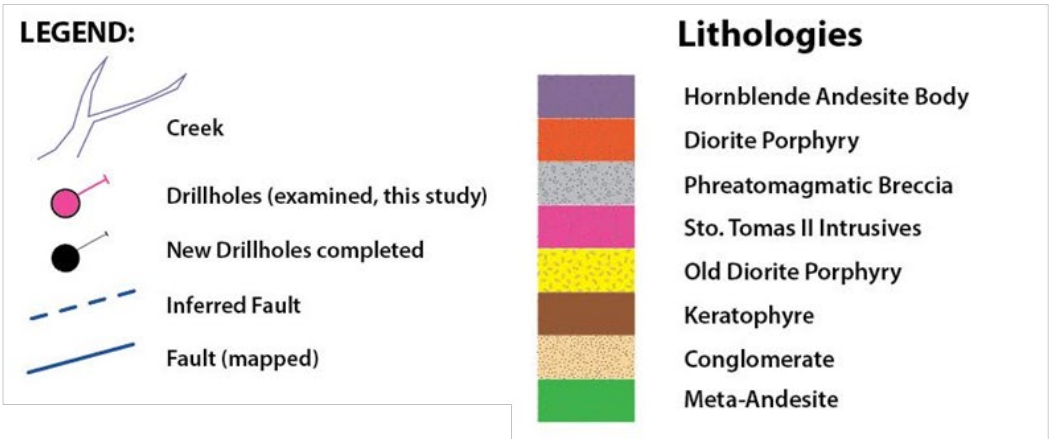

Fig. 5 Geologic Map of the Southwest prospect. Drillhole collar locations and traces are also plotted and those observed for this study are marked in pink. Red line defines the vertical profile line A-A', while the dashed lines perpendicular to it indicates the section line buffer (50m), and the arrows indicate the view of the cross-section. Modified from Philex Mining Corp. (Unpublished).

1.5 Exploration Activities in the Southwest prospect

Drilling activities in the Southwest prospect began in the 1980's with sinking of nine vertical drillholes with significant copper and gold grades, while four drillholes were drilled in the northwestern periphery known as the "Southwest Breccia" (Philex Mining Corporation, 2017). Rock types that were encountered by the drill holes were composed of breccias with clasts of quartz diorites and andesite porphyries, andesitic volcanic rocks (Sillitoe, 2011; Obial & Cinco, 2013). In 2011, the copper and gold footprints and geology of the prospect were confirmed by the Philex Mining Exploration group by several reconnaissance mapping activities and by drilling three holes from the exploration tunnel of the 908ML of the Sto. Tomas II deposit, despite the limited exposure of the breccias and intrusive rocks in these drillholes (Coderis, 2011). In 2017, a total of 10,311m of diamond drill core from 18 drillholes was drilled in the prospect (Philex Mining Corporation, 2017). This scout drilling program concluded in the following year, sinking the last two drill holes with a total meterage of 208m (Philex Mining Corporation, 2018).

1.6 Scope of the study

1.6.1 Thesis problems and objectives

In light of the discovery of the porphyry copper type veinlets crosscutting the breccia units in the Southwest prospect, this thesis raised the question on the origin of these veinlets and its significance to the evolution of porphyry copper deposits and related epithermal deposits in the southern Baguio District. The occurrence of these veinlets increased potential of a discovery of blind deposits within the vicinity of the Santo Tomas II deposit.

In this regard, the objectives of this thesis include providing a comprehensive description of the lithologic units, alteration types and ore mineralization of the Southwest

prospect and the elucidation of the nature of ore-forming fluids, the processes of ore-formation and their implications to the formation of ore deposits in the Southern Baguio District.

This work is an important contribution in the further understanding of the porphyry copper mineralization in the Baguio District that would help progress the academic studies and exploration currently being undertaken in the district, and possibly elsewhere with similar ore deposits.

1.6.2 Methods

Field data were gathered through a reconnaissance survey conducted on the roadcuts that were excavated by the construction of access roads for the exploration activities. Detailed core logging was conducted on selected intervals of drillholes SWD-17-02, SWD-17-07, SWD-17-08 and SWD-17-15 (Fig. 5).

Microscopic analyses coupled with Scanning Electron Microscope Energy Dispersive Spectroscope (SEM-EDS) were carried out using a Nikon ECLIPSE LV100N POL microscope and a JEOL JSM-IT300 with Oxford detector X-MaxN (SEM-EDS) installed in Akita University. Analyses with SEM-EDS were carried out in high vacuum condition at working distance of 10mm, accelerated voltage of 15kV and beam current of 2.20 nA.

The mineral identification was also backed up by X-ray Diffraction (XRD) analyses particularly for clay minerals present in the wallrock and vein samples. The clay minerals were oriented by hydraulic elutriation before they were subjected to XRD analyses. Ethylene glycol and hydrochloric acid treatment were also applied.

Hornblende concentrates and biotite concentrates were prepared for K-Ar age dating. The samples were selected on the basis of delineating the syn-mineralization and late-mineralization K-Ar ages. Hornblende concentrates were collected by binocular stereomicroscope assisted manual picking of the hornblende grains after the sample was lightly crushed, sieved and subjected to heavy liquid separation process using the mixture of sodium tungstate adjusted to specific gravity of 2.7 g/cm3. Biotite concentrates were collected using a combination of (1) repeated hydraulic elutriation of a highly biotitized rock to collect biotite and other clay samples before subjected to (2) heavy liquid separation processes using the mixture of Sodium Tungstate adjusted to specific gravity of 2.7 g/cm3 as well. Biotite grains were also manually picked to achieve the weight of 1 g. K-Ar dating was outsourced to Activation Laboratories, Ltd., Ontario, Canada.

Heating experiments on both the polyphase brine and vapor-rich fluid inclusions were conducted using a Linkam 10016 Heating Stage that is installed on a Nikon ECLIPSE LV100N POL polarizing microscope stationed at Akita University to determine the homogenization temperatures of the fluid inclusions.

Chemical compositions of the amphibole and chlorite grains were determined using a JEOL JXA-8800, wavelength dispersive electron microscope microanalyzer installed at Akita University. Acquisition time for each element were 5 seconds, at their characteristic X-ray, and the background counted for 3 seconds each. Measurements were done at 15kV. Amphibole geobarometer and chlorite geothermometer were applied to determine the conditions of formations of the different amphibole and chlorite phases. These data were compared with the interpreted results of the fluid inclusion microtherometry on the fluid inclusions hosted in quartz veinlets.

Sulfur isotopic ratios of sulfide grains associated with various veinlets and alteration were analyzed to determine the source of sulfur of the sulfide minerals associated with porphyry copper mineralization. Sulfide grains were handpicked using a pair of tweezers under a Nikon SMZ 1500 binoculars. The sulfides were decomposed by HNO_3 and Br_2 and were precipitated as $BaSO_4$. The converted $BaSO_4$ was packed with V_2O_5 in a tin foil and was heated in a vacuumed quartz-glass combustion tube to about 1020°C to liberate the SO_2 gas. Sulfur isotopic ratios were measured using a Thermo Fisher Scientific Delta-V Advantage mass spectrometer combined with a Thermo Fisher Scientific Flash 2000 elemental analyzer. Results were converted in the conventional $\delta^{34}S_{CDT}$ per mil (‰) expression through the equation:

$$\delta^{34}S\text{sample} = \{((^{34}S/^{32}S)_{sample}/(^{34}S/^{32}S)_{CDT})\} \times 1000$$

where $^{34}S/^{32}S$ of the Cañon Diablo Troilite has an assigned value of 0.0450045 (Ault & Jensen, 1963; Ohmoto & Rye, 1979). These were calibrated based on regression line calculated from the results of the reference materials from the International Atomic Energy Agency (IAEA) of barium sulfates (IAEA-SO-5 and IAEA-SO-6) and sea water barium sulfate (IAEA-NBS-127). Accuracy of the determinations is estimated to be within ±0.2‰.

2 Lithologic units in the Southwest prospect

2.1 Intrusive rocks

We identified at least four types of intrusive rocks intruding through the MA and sedimentary sequences in the Southwest prospect. In terms of mineralogical composition, the intrusive rocks are similar. The classification scheme was based on the differences in the texture, phenocrystic minerals abundance and textures, and composition of groundmass, crosscutting relationships and degree of alteration. Based on the current work, the intrusive rocks are: (1) Coarse-grained biotite quartz diorite porphyry, (2) Fine-grained quartz diorite porphyry, (3) Medium-grained hornblende quartz diorite porphyry and (4) Hornblende andesite porphyry (Table 1). This study adopts the terminologies used by the exploration team of PMC to conveniently distinguish one intrusive phase from the other. The abbreviations ODP (Old Diorite Porphyry), EMD (Early Mineralization Diorite), LD (Late Diorite) and DP (Diorite Porphyry) have been assigned, respectively. An older diorite was previously recognized as PMD (Pre-mineralization Diorite) to a quartz diorite porphyry, however, the stock of this rock type was not yet found neither by drilling or field mapping and was only recognized in the Southwest prospect as clasts in the breccias. Texturally and compositionally, the PMD shows close affinity with the LD. Thus, only four types are described in this manuscript. Figure 6 shows the vertical profile along section line A-A' (Fig. 5.) with the interpreted geology that was based on the corelogs of the drillholes (Fig. 7).

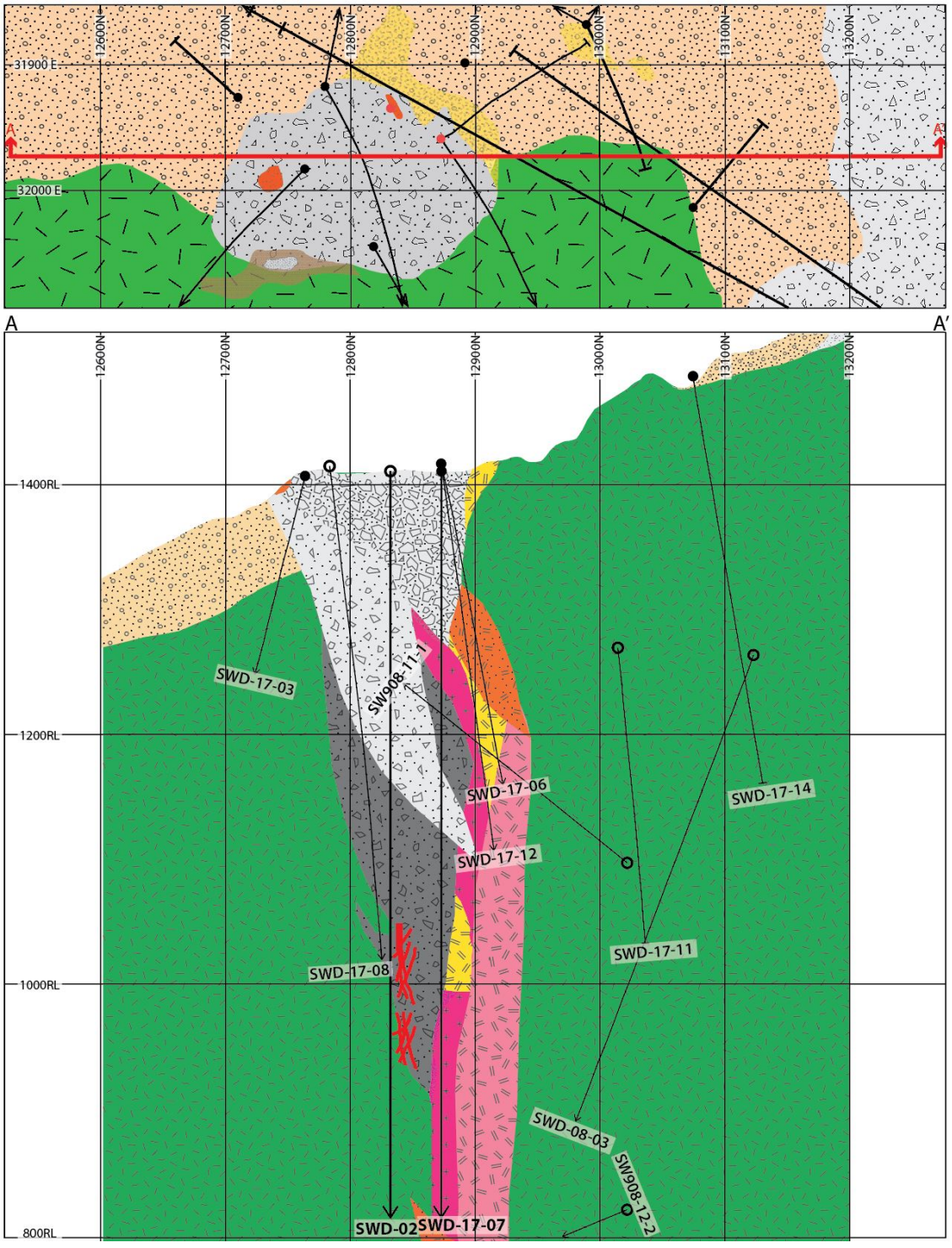

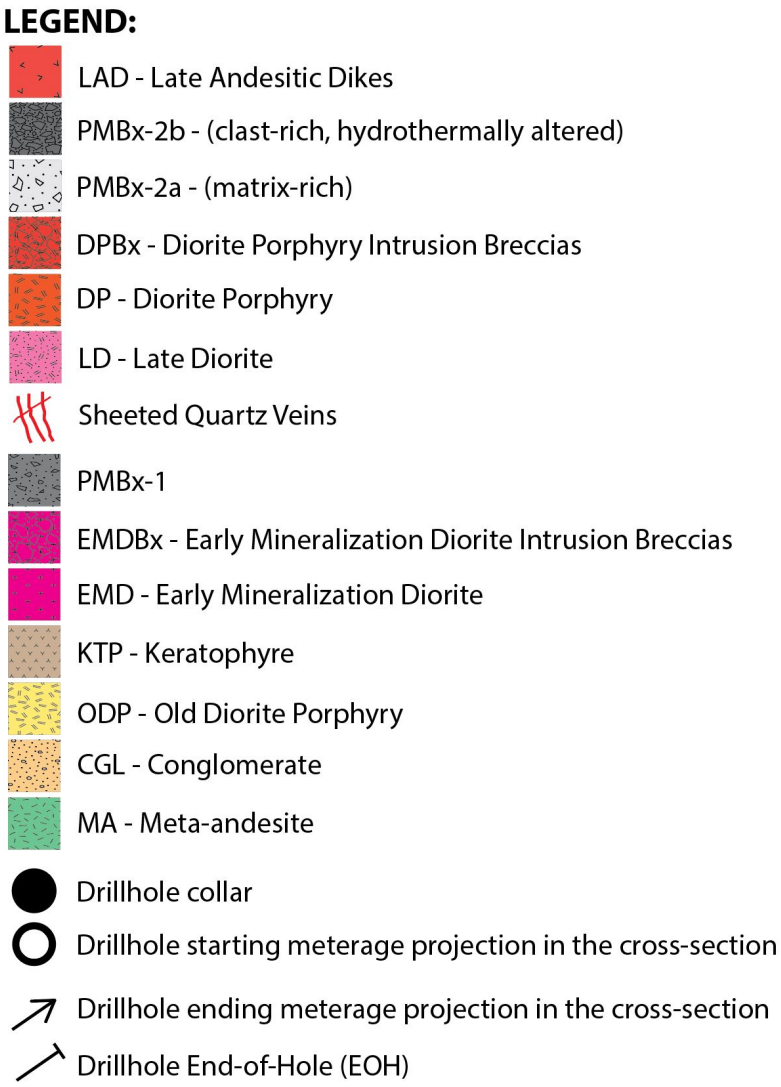

Fig. 6 Vertical profile along A-A' (from Figure 5) showing the spatial and temporal relationships of the various intrusive and breccia units as observed in the drillcores and outcrop. Solid black lines indicate the drillholes studied, while the thin black lines show the other drillholes sunk at the prospect. Graphic logs of drillholes SWD-17-02 and SWD-17-07 are also shown. Thick red lines on the graphic logs indicate the porphyry-type veinlets. Modified from Philex Mining Corporation (Unpublished).

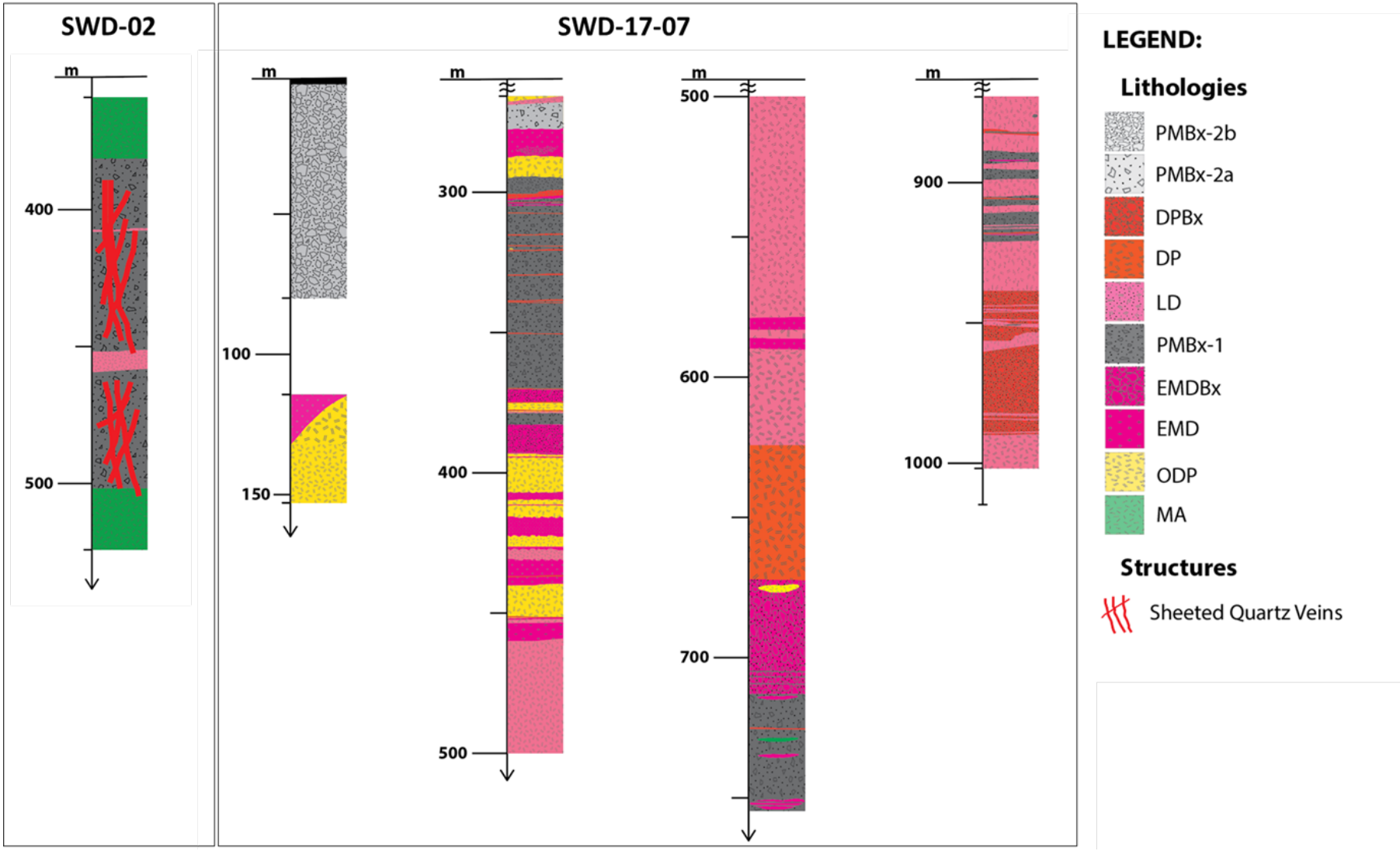
SWD-02
SWD-17-07
m
400
500
100
150
300
500
600
700
900
1000
LEGEND:
Lithologies
PMBx-2b
PMBx-2a
DPBx
DP
LD
PMBx-1
EMDBx
EMD
ODP
MA
Structures
Sheeted Quartz Veins

Fig. 7 Corelogs of SW-02 and SW-17-07, Modified from Philex Mining Corporation (Unpublished). Abbreviations denote: MA – Meta-andesite, ODP – Old Diorite Porphyry, EMD – Early Mineralization Diorite, EMDBx – Early Mineralization Diorite Breccia, PMBx-1 – Phreatomagmatic Breccia Facies – 1, LD – Late Diorite, DP – Diorite Porphyry, DPBx – Diorite Porphyry Breccia, PMBx-2a – Phreatomagmatic Breccia Facies – 2a, PMBx-2b – Phreatomagmatic Breccia Facies – 2b.

2.1.1 Coarse-grained biotite quartz diorite porphyry (ODP – Old Diorite Porphyry)

Drill core sample of the ODP displays typical salt and pepper texture (Fig. 8a). The ODP is exposed on the surface and near-surface with weak weathering, but oxidized. Mafic minerals are decomposed and reddish-brown oxide minerals, such as goethite occur along fractures. Fracture and vein density of the ODP is very low, except for the shallow drillcore samples in the northwestern portion of the prospect, wherein the ODP is densely crosscut by different types of quartz veinlets.

The ODP consists of abundant phenocrysts of euhedral to subhedral grains of plagioclase with grain size greater than 5mm, minor amounts of subhedral biotite and rare hornblende prisms with grain size between 3 and 5mm. The texture exhibited by this rock type is porphyry to seriate, with the phenocrystic minerals consisting more than 50% by volume. The groundmass is mainly composed of anhedral quartz less than 2mm and finer-grained subhedral plagioclase. Some of the phenocrystic biotite and plagioclase grains are weakly altered to chlorite, calcite and sericite (Fig. 8b).

2.1.2 Fine-grained quartz diorite porphyry (EMD – Early Mineralization Diorite)

Drill core samples of the EMD suffered from intense hydrothermal biotite alteration resulting in their dark brownish-gray color (Fig. 8c). The groundmass of the

EMD also appears to be dark gray in color due to abundant magnetite. Fine-grained sulfides such as chalcopyrite and bornite are disseminated. The EMD was sparsely distributed in the shallow portions of the prospect and is observed only as clasts in the breccias, mostly at the central portion intersected by drillhole SWD-02 and SWD-17-07. In the central deeper portion of the prospect it is also found to have clear crosscutting relationship with the breccias (Fig. 8b). In this portion, the EMD is densely crosscut by various types of quartz veinlets, as well as biotite and magnetite stringers.

The EMD also exhibits a porphyry to seriate texture. The phenocrystic minerals consist primarily of euhedral to subhedral plagioclase of less than 5mm, minor anhedral phenocrystic quartz with grain size less than 1mm, and subhedral hornblende phenocrysts with size less than 3mm. Minute accessory zircon grains are included in the hornblende phenocrysts. The EMD evidently suffered from intense hydrothermal biotitization accompanied with quartz, magnetite, bornite, chalcopyrite with or without chlorite, sericite and epidote (Fig. 8d). The less altered rocks display cores of hornblende phenocrysts altered by biotite, magnetite, chalcopyrite, bornite and titanite, and rimmed by chlorite.

Table 1 Petrographic characteristics of the intrusive rocks at the Southwest prospect.

Rock Type	Phenocryst (abundance and size, mm)					Groundmass (size, mm)	Remarks	Abbreviation
	plagioclase	hornblende	biotite	quartz	opaque			
coarse-grained biotite quartz diorite porphyry	+++ (>5.0)	+/-(3.0-5.0)	+(3.0-5.0)	++ (<2.0)	+ (<2.0)	coarse-grained (<0.7)	biotite altered to chlorite	ODP (Old Diorite Porphyry)
fine-grained quartz diorite porphyry (bt)	+++ (<5.0)	+(<3.0)	+ (<0.2)	++ (<1.0)	+ (<2.0)	fine-grained (<0.2)	ferromagnesian minerals altered to secondary biotite (shredded)	EMD (Early Mineralization Diorite)
medium-grained hornblende quartz diorite porphyry	++ (3.0-5.0)	+ (3.0-5.0)		++ (<2.0)	+ (<2.0)	medium-grained (<0.5)	chlorite-epidote-calcite alteration	LD (Late Diorite)

hornblende andesite porphyry	+++ (<3.0)	+(2.0-3.0)	+/- (<0.2)	+ (<2.0)	cryptocrystalline (<0.1)	no alteration noted	DP (Diorite Porphyry)

Note: semi-quantitative abundance of the phenocrysts:

+++ abundant (>30%volume), ++ major (30-10% volume), + minor (10-1%), +/- rare (<1%)

(bt) denotes hydrothermally biotitized sample.

2.1.3 Medium-grained hornblende quartz diorite porphyry (LD – Late Diorite)

The LD also exhibits salt and pepper texture encountered at drillhole meterage of 458.80m of SWD-17-07 corresponding to the central deeper portion of the prospect. The LD is typically strongly propylitic altered (Fig. 8e), where it is in contact with the older rocks, particularly with EMD and MA. On the other hand, strong chlorite-magnetite and sericitic alteration overprinted when in contact with the PMBx1. This is accompanied with dense overprinting of veins from high to low temperature assemblages that will be discussed in detail in the succeeding sections. Furthermore, as observed in the drillcore, the LD is crosscut by centimeter scale PMBx2a dikelets, while at the larger exposures of the PMBx2 breccia facies, the LD occurs as comminuted clasts.

Phenocrystic minerals of the LD consist of plagioclase and hornblende prisms of 3-5mm set in a groundmass composed mostly of anhedral quartz, finer grained subhedral plagioclases and opaque minerals mainly magnetite. The less altered samples show hornblende phenocrysts faintly rimmed by tremolite. The grains of the groundmass are between 1 and 3mm. Plagioclase and hornblende phenocrysts are weakly altered to sericite-calcite and chlorite-epidote, respectively (Fig. 8f).

2.1.4 Hornblende andesite porphyry (DP –Diorite Porphyry)

Drillcore samples of the DP exhibit a darker gray color similar to that of the "andesite porphyry" of the Sto. Tomas II deposit (Serafica & Baluda, 1977; Imai, 2001; Baluda & Galapon, 2005) and the "LAP" of the Clifton prospect (Cirineo, 2017). Rounded plagioclase phenocrysts, as well as, the hornblende needles are distinct in the extremely fine-grained groundmass (Fig. 8g). The DP was encountered at the central shallower portions at about 1,200 masl crosscutting the LD. The DP, however, was in turn

crosscut by the PMBx2 breccia facies as indicated by its occurrence as clasts in the PMBx2 breccia facies.

The DP is mainly composed of plagioclase phenocrysts with grain sizes ranging between 1 and 3mm, minor hornblende phenocrysts and anhedral opaque minerals, mostly magnetite and minor pyrite set in cryptocrystalline groundmass. The plagioclase prismoids are euhedral to subhedral, nonetheless, occasionally exhibits “broken” phenocrysts. Among the intrusive rocks in the Southwest prospect, the DP is the least-hydrothermally altered, indicating a late to post-mineralization timing in the Southwest prospect (Fig. 8h).

2.2 Breccia facies

At least five facies of breccias were recognized and interpreted to represent at least five brecciation events overlapping with intrusive events in the Southwest prospect (Table 2). The breccias were distinguished based on composition of clast, size, shape and distribution, matrix composition and cement composition. Three of them (PMBx1, PMBx2a, PMBx2b) are equivalent to the “phreatomagmatic breccia” of Sillitoe (1985), “diatreme breccia” of Baker et al. (1986) or “endogenous phreatomagmatic breccia” of Lawless and White (1990). The other two facies (EMDBx and DPBx) are equivalent to the “intrusion breccias” of Sillitoe (1985).

Table 2 Characteristics and Interpretation of the Breccias.

Facies	Description	Timing Relationships	Interpretation (s)
PMBx1	Consolidated with chaotic mixture of polymictic clasts consist of MA, ODP and EMD; high degree of rounding of clasts and comminution to rock flour; presence of juvenile tuffaceous matrix and quartz vein fragments; dominantly matrix-rich; overprinted by vein quartz	**Syn-mineral**	Phreatomagmatic breccia
PMBx2a	Consolidated with chaotic mixture of polymictic clasts consist of MA, ODP, EMD, LD and DP; high degree of rounding of clasts and comminution to rock flour; presence of juvenile tuffaceous matrix and quartz vein fragments; dominantly matrix-rich; not overprinted by vein quartz	**Late-mineral**	Phreatomagmatic breccia
PMBx2b	Consolidated clast-rich breccia exhibiting "jigsaw-puzzle" fit; clasts consist of mainly ODP; localized at the fringes and top portion of the breccia pipe; cemented by chlorite-pyrite-gypsum	**Late-mineral**	Phreatomagmatic breccia

EMDBx	Clast-supported breccia localized along the margins of the contact of EMD with MA, transitions to PMBx1; reaction rims commonly observed in the clasts, crystalline matrix	**Syn-mineral**	Intrusion breccia
DPBx	Clasts-supported breccia localized at the contacts of DP with other lithologic units; crystalline matrix; limited exposure	**Late-Mineral**	Intrusion breccia

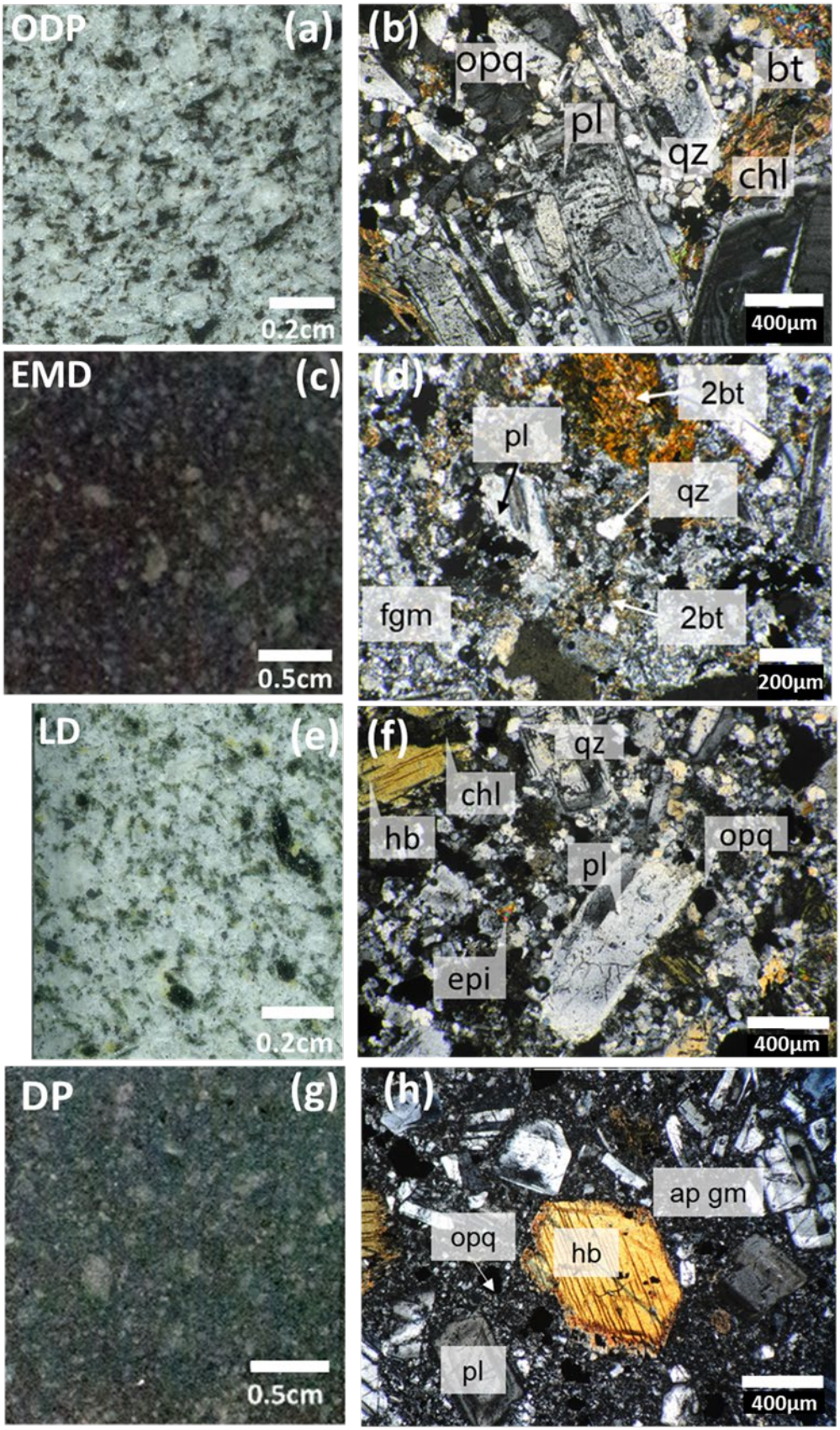

Fig. 8 Hand specimens and photomicrographs of the representative samples of intrusive rocks in the Southwest prospect. (a) Coarse-grained biotite quartz diorite porphyry (ODP, 05-151.55m): seriate to granular texture composed of mainly of plagioclase feldspar, minor quartz and relatively abundant mafic phenocrysts and; (b) coarse-grained biotite quartz diorite porphyry (ODP, 05-151.55m) viewed XPL: same sample as (a), minor dusting of sericite on plagioclase laths, quartz in the interstices of plagioclase, and biotite altering to chlorite; (c) fine-grained quartz diorite porphyry (EMD, 02-390m): fine-grained plagioclase phenocrysts set in a dark brown matrix composed of secondary biotite dissemination; (d) fine-grained quartz diorite porphyry (EMD, 02-390m) in XPL: former mafic phenocrysts completely altered to secondary biotite, abundant sericite dusting accompanied by calcite; (e) medium-grained porphyrytic hornblende quartz diorite (LD, 07-458.80m); porphyrtic texture is distinct, plagioclase is easily distinguishable as coarser-grained laths, while quartz constitute most of the groundmass, chlorite partially alters hornblende; epidote is present; and (f) medium-grained porphyrytic hornblende quartz diorite (LD, 458.80m) viewed in XPL: minor sericite dusting in plagioclase accompanied by epidote and minor calcite, (g) hornblende andesite porphyry (DP, 02-59.70m): distinct porphyry texture, coarse-grained subrounded plagioclase phenocrysts, which are coarser than (a) and (b) are set in a very fine grained matrix, and (h) hornblende andesite porphyry (DP, 02-59.70m): broken plagioclase phenocrysts set in a glassy matrix, not affected by hydrothermal alteration. Abbreviations denote: ODP – Old Diorite Porphyry, EMD – Early Mineralization Diorite, LD – Late Diorite, DP – Diorite Porphyry, ap gm – aphanitic groundmass, fgm – fine grained groundmass, opq – opaque mineral, pl – plagioclase, qz – quartz, chl – chlorite, 2bt – secondary biotite, XPL – view in cross polars.

2.2.1 PMBx1 (Phreatomagmatic Breccia Facies 1)

PMBx1 (Phreatomagmatic Breccia Facies 1) is a consolidated breccia with a chaotic mixture of various clasts, thus polylithologic or polymictic. Clasts size varies from millimeter-sized pebbles to meter-sized blocks and bombs. Most of the clasts are significantly rotated, while comminution to rock flour is also often observed (Fig. 9a). While some clasts are significantly rounded, most of the clasts are subangular. The presence of juvenile tuffaceous matrix is diagnostic in this type of breccia (Fig. 9b), and this is what distinguishes it from the breccia facies of the metavolcanic rocks of Pugo Formation and the later intrusion breccias. Exposures in drillcores often display clast-supported texture, particularly at the central deeper portion of the prospect where stockworks of quartz veining are observed. In addition, matrix-supported texture is also a common occurrence, particularly when the PMBx-1 is observed to truncate the intrusive rocks. There are abundant biotitized and potassic-altered rocks among the clasts, identified as EMD fragments, consisting of more than 50% of the clasts. Basaltic and andesitic rocks of the Pugo Metavolcanics are also common, consisting about 30% of the clasts, while ODP fragments are also observed, comprising about 10 to 15% of clasts. Occurrences of quartz vein fragments are also common. The PMBx1 is interpreted to be an intra-mineralization breccia based on the presence of quartz vein fragments and at the same time overprinted by various types of quartz veins and veinlets.

2.2.2 PMBx2a (Phreatomagmatic Breccia Facies 2a)

PMBx2a (Phreatomagmatic Breccia Facies 2a) is also a consolidated breccia with a chaotic mixture of various clasts in terms of size, distribution and degree of roundness (Fig.9c). Rock flour and juvenile tuff component are abundant in the matrix. In drillcore, the PMBx2a exhibits matrix-supported texture. Various lithologic units are contained as

clasts, which include the basaltic and andesitic rocks, as well as silicified fragments of the Pugo Metavolcanics. Fragmented intrusive rocks of the EMD, ODP, LD (Fig.9d) and DP, are also a common occurrence, and some fragments of breccias interpreted to be the PMBx1. Dominant clast components vary depending on the spatial characteristics of the PMBx2a, nonetheless, rough approximation indicates that PMBx2a in situated in the deeper levels (<1350ML) are dominated by basaltic and andesitic fragments (35%) and LD fragments (25%). EMD is also common component of the clasts with approximate abundance of 10%. ODP and DP fragments are present but are not abundant. In contrast, the clasts of the PMBx2a at the shallower levels (>1350ML) are dominated by EMD (35%) fragments. Other clasts components are the basaltic and andesitic rocks of Pugo Formation (20%), LD (15%), DP (10%) and ODP (10%) fragments. Various quartz vein fragments are also present, nevertheless, the PMBx2a was not observed to be overprinted by quartz veins and veinlets.

2.2.3 PMBx2b (Phreatomagmatic Breccia Facies 2b)

PMBx2b (Phreatomagmatic Breccia Facies 2b) is a sub-facies of the PMBx2a that exhibits clast-supported matrix instead (Fig. 9e). Clast distribution is also chaotic but becomes less chaotic at the fringes and top portion of the breccia pipe. Clast sizes are dominated by fragments larger than cobble size, while significant rounding and grinding to smaller fragments along the margins of the larger clasts are common features. Rock flour and juvenile tuff component in the matrix are still diagnostic, similar with that of the other PMBx facies. However, the dominant clast components in this facies are the ODP (50%) clasts. KTP fragments are also major components (35%), and basaltic and andesitic fragments of the Pugo Metavolcanics (15%). In the shallower portions, chlorite-pyrite cementing is common.

2.2.4 EMDBx (Early Mineralization Diorite Breccia)

EMDBx (Early Mineralization Diorite Breccia) is a breccia facies situated along the contact with the EMD with the Pugo Metavolcanics and the PMBx1. The EMDBx commonly exhibits a clast-supported texture (Fig. 9g). Clast components are chiefly made up of the EMD (90%) itself, while the matrix is comminuted EMD, cemented by hydrothermal minerals, mostly by quartz, biotite and magnetite (Fig. 9h). Basaltic and andesitic rocks of Pugo Formation are minor clast components (about 5%) but increases in volume towards the basement rock. Reaction rim is commonly observed among the clasts. In the central deeper portion, at the 770m intercept of drillhole SWD-17-07, EMDBx was observed as a transition between the EMD and PMBx1.

2.2.5 DPBx (Diorite Porphyry Breccia)

DPBx (Diorite Porphyry Breccia) is a breccia facies localized at the contacts of the DP with the other lithologic units. Similar with the EMBx, DPBx also has a clast-supported texture and clasts components consisting of the DP (90%). The rest of the clasts are composed of the earlier formed intrusive rocks, EMD and LD, and the basaltic and andesitic rocks of the Pugo Formation. Exposures of the DPBx are limited and are localized along the margins of the DP.

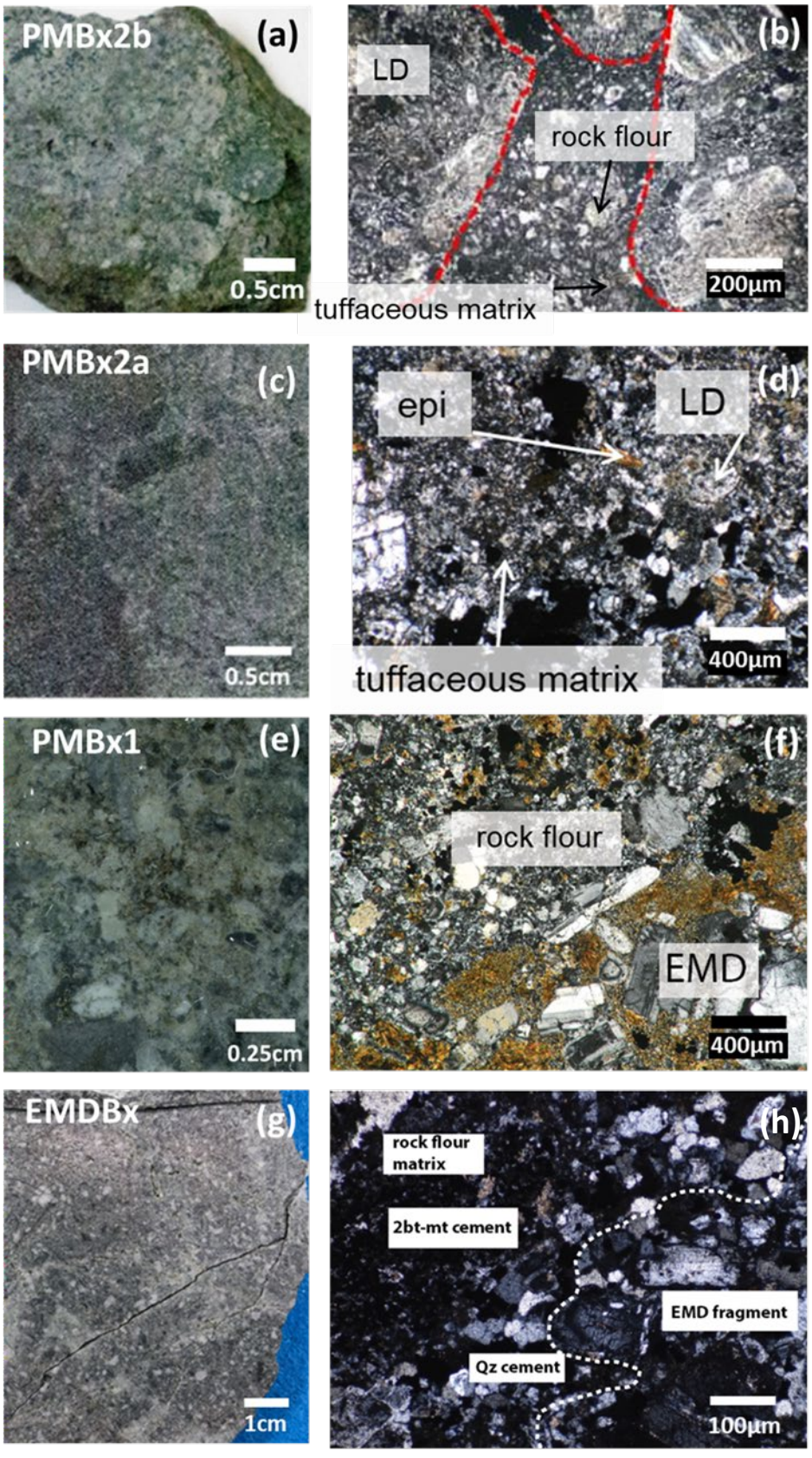

Fig. 9 Hand specimens and photomicrographs of the representative samples of phreatomagmatic breccias: (a) Phreatomagmatic Breccia Facies 2b (PMBx2b, 02-53.70m), poorly sorted clast-rich breccia, clasts include variably altered rocks consisting of LD (Late Diorite) and metavolcanic rocks (b) Phreatomagmatic Breccia Facies 2b (PMBx2b, 02-53.70m) in XPL showing the rock flour matrix; (c) Phreatomagmatic Breccia Facies 2a (PMBx2a, 02-459.40m): matrix rich breccia (d) Phreatomagmatic Breccia Facies 2a (PMBx2a, 02-459.40m) in XPL and (e) Phreatomagmatic Breccia Facies 1 (PMBx1, 02-395.10m) showing breccia fine-grained comminuted clasts and (f) Phreatomagmatic Breccia Facies 1 (PMBx1, 02-395.10m) in XPL with EMD clast; (g) Early Mineralization Diorite Breccia (EMDBx, 02-390.00m) showing hydrothermally cemented breccia by quartz and secondary biotite and magnetite, and (h) Early Mineralization Diorite Breccia (EMDBx) in XPL with EMD clast and secondary biotite and magnetite cement. Abbreviations denote: epi – epidote, XPL – view in cross polars.

2.3 Basement rocks

2.3.1 MA (Meta-andesite)

Meta-andesite (MA) refers to the Eocene-Oligocene basement rocks of the Pugo Formation in the Baguio District (Peña, 2008; Serafica & Baluda; 1977; Baluda & Galapon, 2005). In the Southwest prospect, drillcore intercepts are mostly consist of intercalated sequence of basaltic and andesitic volcanic and tuffaceous rocks of various textures ranging from aphanitic to medium-grained porphyritic. Volcanic breccias are also present, containing clasts of silicified and tuffaceous rocks. In the shallow northern periphery of the prospect, the MA is intensely crosscut by quartz vein stockworks consisting of granular quartz veinlets and sheeted quartz veinlets and biotite and magnetite stringers. The sheeted quartz veinlets found at the shallow intervals of SWD-17-05 153.55m, which will be referred to as shallow sheeted quartz veinlets throughout

the text, are hosted in a tuffaceous rock of the MA and was crosscut by a medium-grained hornblende quartz diorite, presumed to be the LD. The MA hosting the sheeted quartz veinlets suffered from localized silicification. At the deeper levels of the prospect, the MA suffered from pervasive biotitization, particularly along the margins of the contact with the EMD. The potassic alteration envelope affecting the MA also includes the occurrence of hairline quartz-biotite veinlets with chlorite selvages and biotite-chlorite stringers.

2.3.2 CGL (Conglomerate)

Conglomerate (CGL) outcrops at the exploration roadcuts and was also intersected in the shallow intervals of SWD-17-11 and SWD-17-18 at the northern periphery of the prospect. The conglomerate is poorly-sorted, but is well-cemented. The clasts are composed of sub-rounded to well-rounded fragments of basaltic and andesitic lavas, silicified volcanic rocks, zeolite-altered volcanic rocks and variably oxidized volcanic rocks. The absence of carbonaceous clasts is also notable and may indicate correlation with the Zigzag Formation (Peña, 2008). The CGL is also crosscut by centimeter-scale unconsolidated pebble dikes and stockworks composed of granular quartz with scarce sulfides.

2.3.3 KTP (Keratophyre)

The term Keratophyre (KTP) was based on the Keratophyre series of Fernandez and Damasco (1979) that was used to name the volcanic rocks older than Miocene in the Baguio District. The KTP in the Southwest prospect is composed of flow-banded dacitic tuff that is in contact with the CGL at the surface exposures. It is similar with dacite flows intercalated with thick sedimentary layers of ferruginous volcanic conglomerates, which are poorly sorted but are well-cemented (Fernandez & Damasco, 1979). The KTP also

crosscuts the ODP, a pre-mineralization diorite at the shallow portions of the Southwest prospect. No age estimate is available for the ODP, as well as for the KTP, thus, it is difficult to construct an exact stratigraphic correlation. Nonetheless, crosscutting relations place both at the pre-mineralization stage in the Southwest prospect. Exposures of the KTP show flow-banded texture of alternating dark and light colored tuffaceous materials, which are frequently variably rotated, indicating affinity to a probably former volcanic edifice of composite volcano or a rhyolitic dome (Gill, 2010). The KTP also occurs as clasts in the PMBx1. KTP is generally unaltered with localized weakly silicified portions.

3 Porphyry type veinlets and hydrothermal alteration

3.1 Potassic alteration

Potassic alteration in the Southwest prospect is characterized by an assemblage of secondary biotite-quartz-magnetite-chalcopyrite-bornite. It is well-developed in the EMD and andesitic clasts of Pugo Metavolcanics in the breccia facies. It is also well-developed at the deeper central portion of the prospect, affecting the adjacent EMDBx and PMBx1 (Fig. 10).

In the EMD, secondary biotite is mostly present as polygrain aggregates completely altering former ferromagnesian minerals, mainly hornblende. This alteration is often accompanied with quartz, magnetite and copper-iron sulfides and trace anhydrite. The EMD has also suffered from micro-fracturing that was filled by secondary biotite-magnetite with occasional chalcopyrite and bornite. Occasional chlorite, sericite and epidote, as well as trace K-feldspar are present in the assemblage, altering the plagioclase grains.

Potassic alteration in the MA is usually present as stringers of magnetite, quartz and bornite with scarce sulfides consisting mainly of chalcopyrite and trace bornite that are usually selvaged by biotite, chlorite and sericite, at the contacts with EMD in the central deeper part of the prospect. In contrast, potassic alteration in the EMDBx is exhibited as secondary biotite, magnetite, quartz, scarce chalcopyrite and bornite in the matrix. Clasts of the EMD in the EMDBx are also heavily biotitized, as well as the clasts of the EMD and MA in the PMBx1.

The veinlet types magnetite-biotite and magnetite±quartz represent the earliest among the veinlets in the potassic alteration in the Southwest prospect. They are

characterized as hairline streaks of magnetite with biotite, with or without quartz and are sometimes accompanied with chalcopyrite.

Quartz-bearing vein assemblages are also contemporaneous with the potassic alteration in the Southwest prospect. The EMD, in particular, hosts abundant wispy quartz veinlets, sheeted quartz veinlets (Fig. 11a), quartz±K-feldspar veinlets (Fig. 11h), granular quartz veinlets (Fig. 11a) and banded gray quartz veinlets (Fig. 11b; Fig. 12). These are also usually overlapped by hairline streaks of magnetite-chalcopyrite and trace amounts of bornite, while some are "center-lined". Chalcopyrite and bornite typically display micrographic texture (Fig. 11f). At the central deeper portion, where the PMBx1 and LD are in contact, these veinlets pervasively cut through the PMBx1 (Fig. 11c), and are sinuous and crenulated, even the sheeted quartz veinlets, which are usually planar in other deposits in the vicinity (e.g. Sto. Tomas II, Clifton; Imai, 2001; Cirineo, 2007). Sheeted quartz veinlets are also subvertical. Sheeted quartz veinlets at the shallow northern periphery hosted in the volcanic breccia of the MA are also sinuous (Fig. 11d). These are, however, distinct from the other veinlets found at the shallower peripheries of the prospect, which are composed of the granular quartz and sheeted quartz veinlets that crosscut the meta-andesite and basalt of the MA and CGL that show planar morphology (Fig. 11e). Some of the veinlets from this type are selvaged by narrow chlorite-sericite envelopes and to a lesser degree, K-feldspar envelopes. Gray banded quartz veinlets have the widest sericitic envelope. Plagioclase in the host rocks are preserved. Furthermore, fragments of those quartz veinlets are also observed as clasts in the PMBx1.

3.2 Chlorite-magnetite alteration

Chlorite-magnetite alteration consisting of the assemblage of chlorite-magnetite-sericite-carbonates (mostly calcite) ± actinolite overprinted the earlier potassic alteration

specifically on the PMBx1. Magnetite-chlorite is the dominant alteration assemblage in the wallrocks at the portion adjacent to the contact between the PMBx1 and LD at the central deeper portion of the prospect (Fig. 10). This grades to a more dominant chlorite-sericite alteration with decreasing depth and increasing distance away from the zone of intense quartz vein stockworks and subparallel sheeted quartz veinlets.

Contemporaneous veinlets include a quartz-free assemblage of chlorite-magnetite (Fig. 11b), chlorite-sericite and the chlorite-magnetite-actinolite±sericite stringers (Fig. 12). The veinlets are characterized as sinuous hairline streaks, similar to the early biotite veinlets. The chlorite-magnetite-actinolite±sericite stringers are accompanied with abundant chalcopyrite with trace amounts of bornite, typically overlapping the subvertical sinuous sheeted quartz (Fig. 11b and 11g) in the PMBx1. Moreover, this represents the zone of highest copper and gold grades in the Southwest prospect. On the other hand, chlorite-magnetite stringers and chlorite-sericite stringers are typically sulfide poor, but are accompanied with chalcopyrite±pyrite and pyrite±chalcopyrite, respectively.

3.3 Sericite-chlorite alteration

The sericite-chlorite alteration overprinted the PMBx1 and intrusive stocks such as the EMD, DP and ODP at the shallower portions of the prospect and cements the martices of the PMBx2a and PMBx2b (Fig. 10). It is usually accompanied with pyrite cubes. Overprinting is usually manifested as veinlets consisting of 1-2 cm sericite-chlorite and pyrite-filled chlorite veinlets enveloped by sericite and K-feldspar destructive alteration (Fig. 11h). XRD analysis on air dried samples suggests the occurrence of chlorite and sericite indicated by the peaks at 10.0Å and 14.7Å.

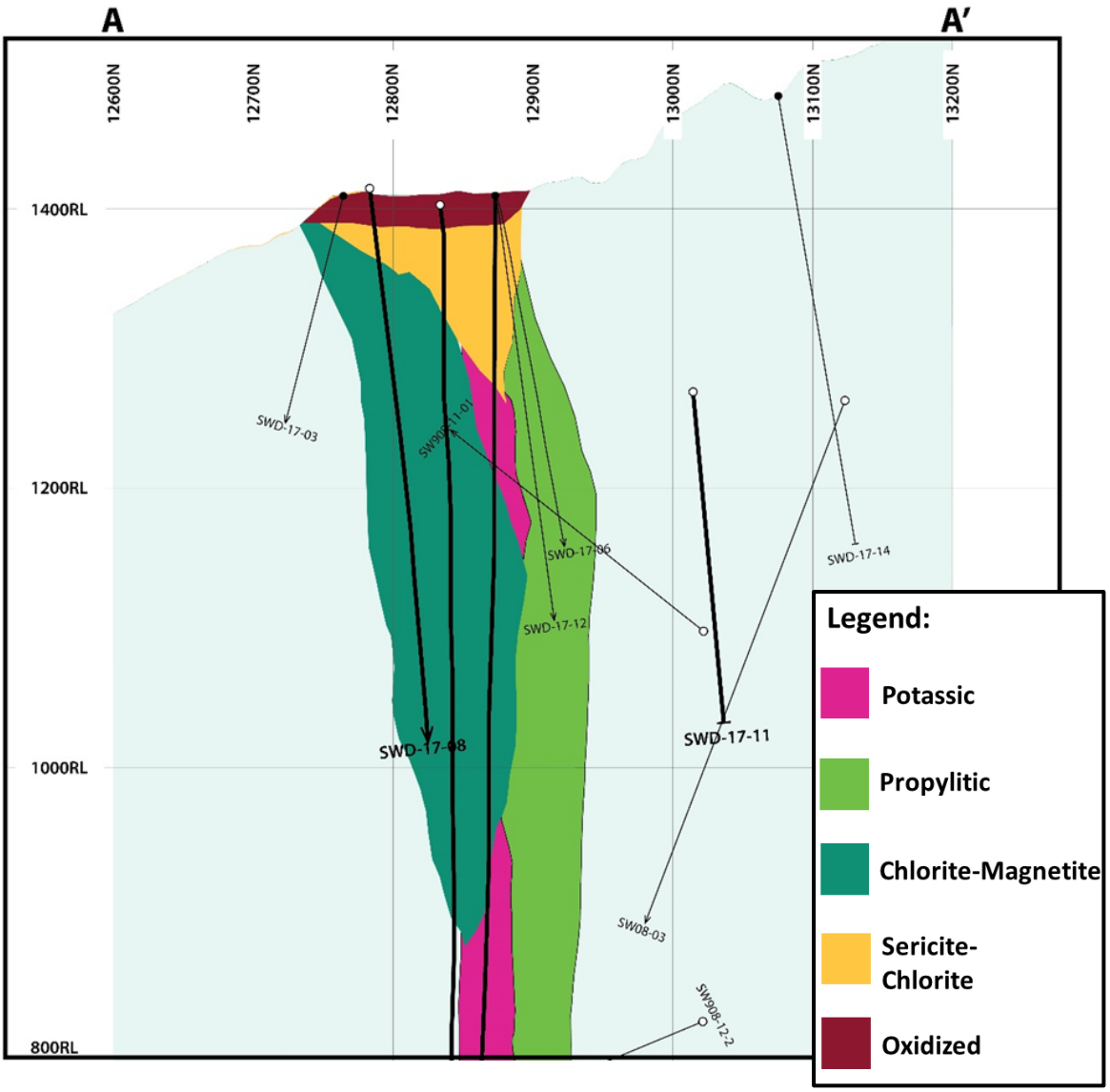

Fig. 10 Vertical profile along A-A' (from Figure 5) showing the spatial distribution of the alteration assemblages in the Southwest prospect. Modified from Philex Mining Corporation (Unpublished).

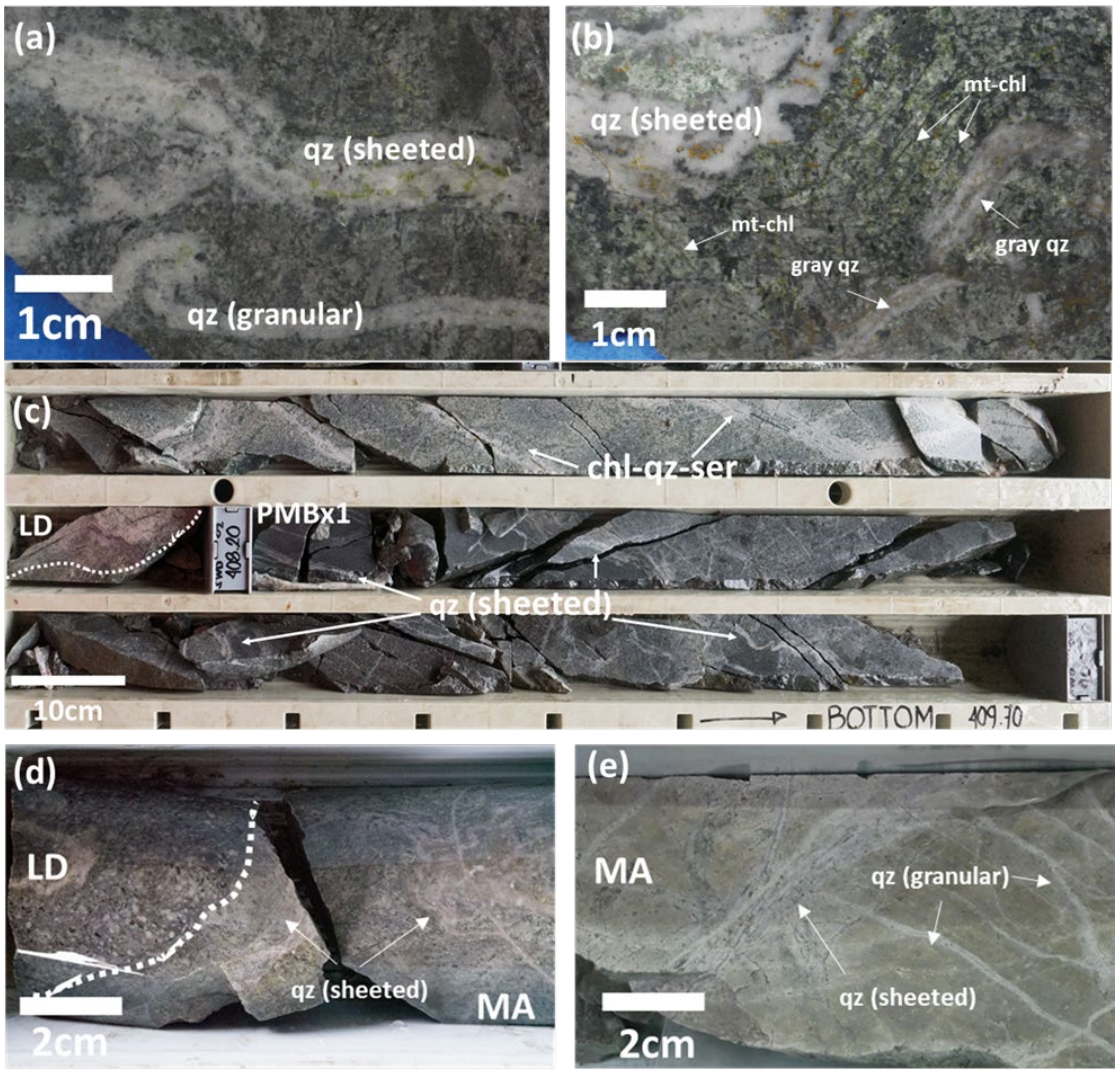

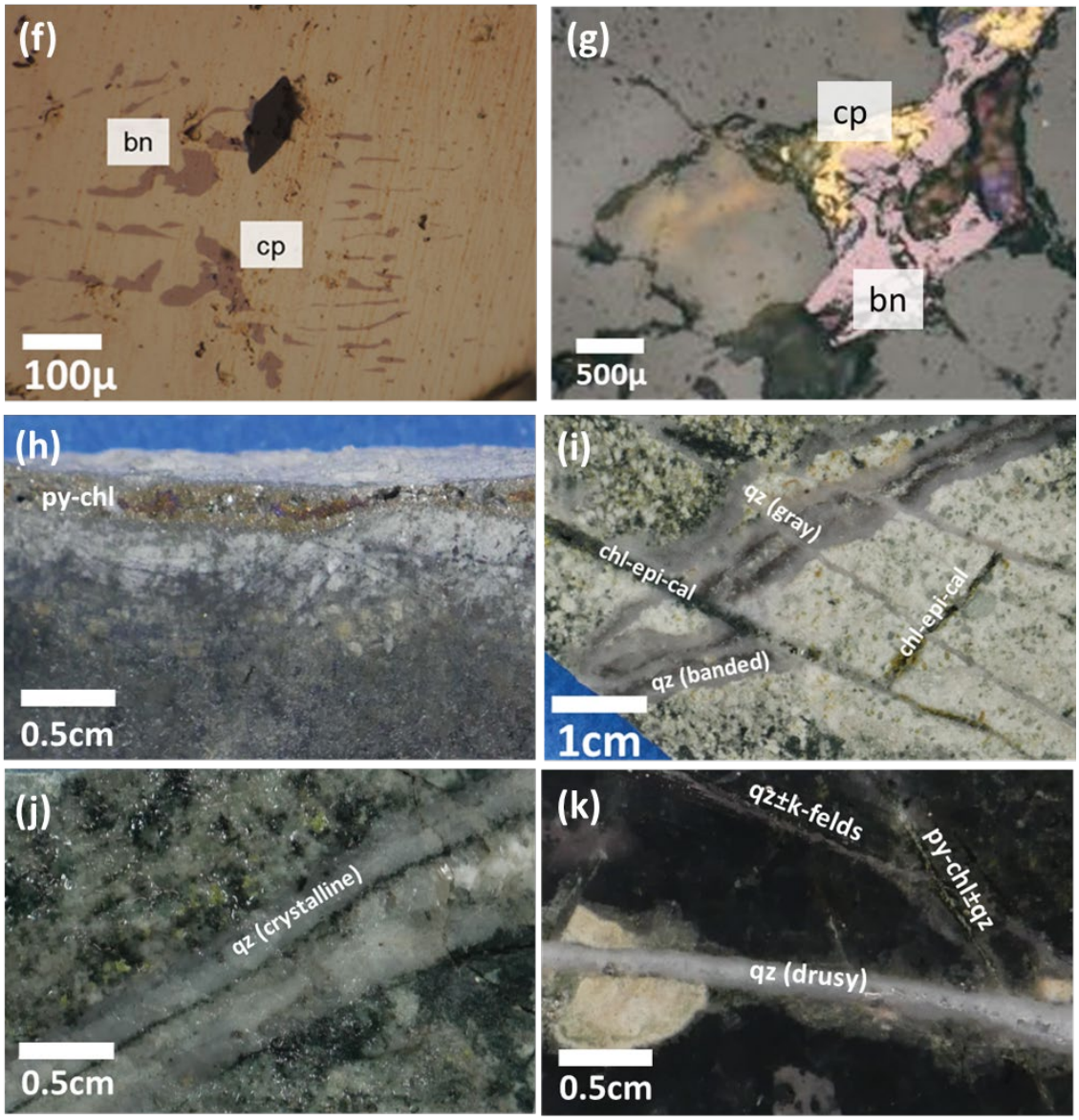

Fig. 11 Samples of veins contemporaneous with the hydrothermal mineral assemblages: (a) sinous sheeted quartz and granular quartz contemporaneous with potassic alteration hosted in the Early mineralization diorite breccia (EMDBx), sheeted quartz and granular quartz are accompanied with magnetite and scarce chalcopyrite±bornite, sheeted quartz is overlapped by the greenish hairline streaks of chlorite-actinolite-magnetite±chalcopyrite (02-436.15) (b) crenulated sheeted quartz hosted in LD and gray quartz hosted vein fragment; strong overprint of chlorite-magnetite alteration accompanied with sericite and overlapping chlorite-magnetite veinlets (02-396.95); (c) core photo showing the crosscutting relations between the LD, PMBx-1and sheeted quartz veinlets at the central deeper level of the prospect at drillhole SWD-02 (407m to 409.70m); (d) core photo showing the crosscutting relations between LD, MA and sheeted quartz veinlets in the northern shallow periphery of

the prospect at drillhole SWD-17-05 (153.35-153.55m); (e) core photo showing the planar sheeted and granular quartz veinlets hosted in MA at drillhole SWD-17-11 (117.50-117.70m); (f) chalcopyrite and magnetite showing micrographic texture in biotite stringer potassic alteration (02-197), (g) chalcopyrite-bornite assemblage in sheeted quartz (02-398.65), (h) pyrite-chlorite veinlet contemporaneous sericite-chlorite alteration, accompanied by a feldspar-destructive sericitic alteration envelope (02-177.25), (i) banded gray quartz veinlet offset by chlorite-epidote-calcite veinlet (02-408), (j) crystalline quartz contemporaneous with propylitic alteration hosted in LD (02-489.85), (k) offsetting relationship between quartz±K-feldspar associated with potassic alteration by pyrite-chlorite±quartz and later drusy quartz veinlet, which is accompanied by chlorite±pyrite (02-380.30). Abbreviations denote: qz – quartz, mt – magnetite, chl – chlorite, bn – bornite, cp – chalcopyrite, py – pyrite, cal – calcite, epi – epidote, K-felds – K-feldspar; LD – Late Diorite, PMBx-1 – Phreatomagmatic Breccia Facies 1, MA – Meta-andesite.

3.4 Propylitic alteration

Propylitic alteration is characterized by an assemblage of chlorite-epidote-calcite±sericite, and commonly affected the margins of the LD. The degree of alteration is strongest at the portion of the supposed apex of the intrusion but decreases inward in the intrusion (Fig. 10). The assemblage also altered the peripheral wallrock mainly MA. Plagioclase grains are usually dusted by sericite accompanied with calcite and epidote, while hornblende phenocrysts are partially altered to chlorite.

Propylitic alteration is accompanied with chlorite-epidote-calcite (Fig. 11i), crystalline quartz veinlets (Fig. 11j), and vuggy quartz veinlets (Fig. 11k), and calcite veinlets (Fig. 12). These veinlets are typically sulfide-poor, but occasional pyrite fills the cavities in the veins. Pyrite is rarely accompanied with chalcopyrite. These veinlets are also typically planar in morphology. Moreover, vuggy quartz typically occupies the re-opened spaces in earlier formed quartz veinlets.

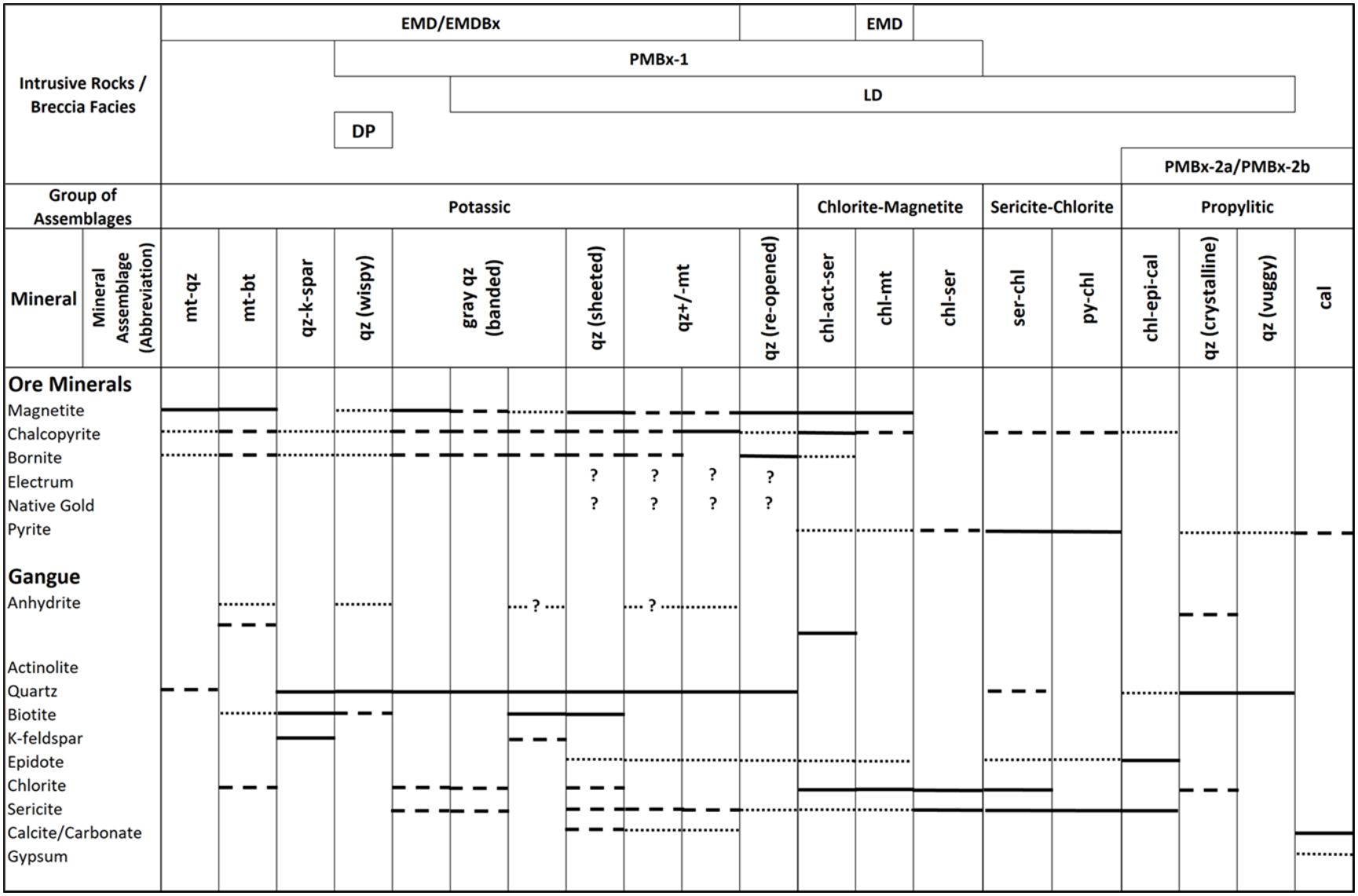
Intrusive Rocks / Breccia Facies
EMD/EMDBx
EMD
PMBx-1
LD
DP
PMBx-2a/PMBx-2b
Group of Assemblages
Potassic
Chlorite-Magnetite
Sericite-Chlorite
Propylitic
Mineral
Mineral Assemblage (Abbreviation)
mt-qz
mt-bt
qz-k-spar
qz (wispy)
gray qz (banded)
qz (sheeted)
qz+/-mt
qz (re-opened)
chl-act-ser
chl-mt
chl-ser
ser-chl
py-chl
chl-epi-cal
qz (crystalline)
qz (vuggy)
cal
Ore Minerals
Magnetite
Chalcopyrite
Bornite
Electrum
Native Gold
Pyrite
Gangue
Anhydrite
Actinolite
Quartz
Biotite
K-feldspar
Epidote
Chlorite
Sericite
Calcite/Carbonate
Gypsum

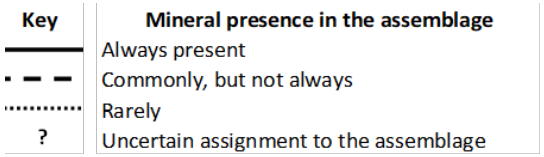

Fig. 12 Summary of the abundance of alteration mineral associated with the contemporaneous veinlet. Abbreviations mean: mt – magnetite; bt – biotite; qz – quartz; K-felds – K-feldspar; chl – chlorite; act- actinolite, ser – sericite; py – pyrite, chl – chlorite, epi – epi; gyp-gypsum.

3.5 Ore mineralization

Copper and gold mineralization in the Southwest prospect occur as (1) chalcopyrite and bornite associated with the potassic alteration, and (2) overlapping veinlets associated with the chalcopyrite-magnetite-chlorite-actinolite±sericite veinlets contemporaneous with the chlorite-magnetite alteration (Fig. 12). These are controlled by lithology, but are more strongly influenced by structures, particularly by fractures and veinlets as corroborated by the correlation and distribution of copper and gold grades represented by the 3-m interval of fire assay results on the drill cores on holes SWD-02, SWD-17-07, SWD-17-05, SWD-17-08 and SWD-17-11.

Among the intrusive rocks, the syn-mineralization EMD has consistent copper and gold grades of greater than 0.10 % and 0.20 ppm, respectively. Copper and gold grades are positively correlated. Despite the late-mineralization timing of the LD, copper and gold grades are elevated in the LD, ranging from 0.20 % Cu and 0.30 ppm Au to as high as 0.43% Cu and about 1.00 ppm Au, showing a linear trend similar to that of the syn-mineralization EMD (Fig. 13a). Nevertheless, the correlation between copper and gold grades in the LD is obscure at grades less than 0.20 % Cu and 0.30 ppm Au, as well as with the other intrusive rocks, such as the ODP and DP (Fig. 13a). The correlation of copper and gold grades in the breccia facies, such as the PMBx1 and PMBx2a are positively correlated, nonetheless, the obvious difference in the concentration of the metals (Fig. 13a). The copper and gold grades of most of the PMBx1 samples are greater than 0.10 % Cu and 0.10 ppm Au. In contrast, the copper and gold grades of PMBx2a samples are mostly lower than 0.10 % Cu and 0.10 ppm Au. No clear trend is observed in the copper and gold grades of the samples of PMBx2b. The copper and gold grades of the basement rocks, MA and CGL, are significantly greater than 0.20 % Cu and 0.20 ppm

Au (Fig. 13a). The copper and gold grades of CGL are correlated as in the EMD. Such occurrence is more likely due to the influence of potassic alteration in the CGL rocks. On the other hand, copper and gold grades of the MA samples are dispersed in the very low grades of less than 0.10 % Cu and 0.10 ppm Au, while, elevated copper and gold grades that reached greater than 0.50 % Cu and 1.00 ppm Au are also present, the biotitized portions along the contact zones with the EMD.

In terms of the distinction in alteration types, elevated copper and gold grades are intimately associated with the chlorite-magnetite alteration, and to a lesser degree, potassic alteration (Fig. 13b). The copper and gold grades in the sericite-chlorite and propylitic alteration are both below by the 0.20 % Cu and 0.30 ppm Au (Fig. 13b). Anomalously elevated copper and gold grades are intimately associated with sheeted quartz veinlets, localized at the contacts of the EMD, PMBx1 and LD at depths between 380m and 500m of the hole SWD-02 (Fig. 13c). The sheeted quartz veinlets localized in this portion are overlapped by chalcopyrite-chlorite-magnetite-actinolite-sericite veinlets. This occurrence is also observed in the shallow portions of the CGL and MA that are cross-cut by quartz vein stockworks and sheeted quartz veinlets.

Mineral associations in the chalcopyrite and bornite-rich mineralization consist mostly of the assemblage of the potassic alteration. This corresponds to the potassic-altered EMD samples that show grades greater than 0.20% Cu and 0.20 ppm Au. Partly altered hornblende grains in the less altered EMD samples show conversion to secondary biotite accompanied with opaque minerals mainly composed of magnetite, bornite and chalcopyrite. These grains are also rimmed by chlorite. Chalcopyrite and bornite also occur as disseminated grains and veinlet and fracture infills accompanied with biotite, magnetite and quartz.

On the other hand, the mineral assemblage of the chalcopyrite-rich mineralization overlapping the earlier formed sheeted quartz veinlets and host rocks such as PMBx1 and EMD consist of chalcopyrite-magnetite-chlorite-actinolite±sericite. Magnetite grains are mostly subhedral grains without oscillatory zoning. In contrast, the magnetite grains contained in the sheeted quartz veinlets in the Sto. Tomas II deposit show oscillatory zoning (Imai, 2001). On the other hand, chalcopyrite grains are mostly anhedral that form mutual curving boundaries with magnetite. Minute blebs of chalcopyrite are also included in magnetite. Magnetite and chalcopyrite are supposed to have formed contemporaneously (Fig. 14b & 14c) Minute native gold globules are also occurring as small blebs within the chalcopyrite grains (Fig. 14d). The atomic percentage of gold (Au/[Au+Ag]) was 83%. The other constituents are chlorite, actinolite and rare sericite, which occur along the interstices between magnetite and chalcopyrite. Among the samples that were analyzed, gold was only found in this occurrence.

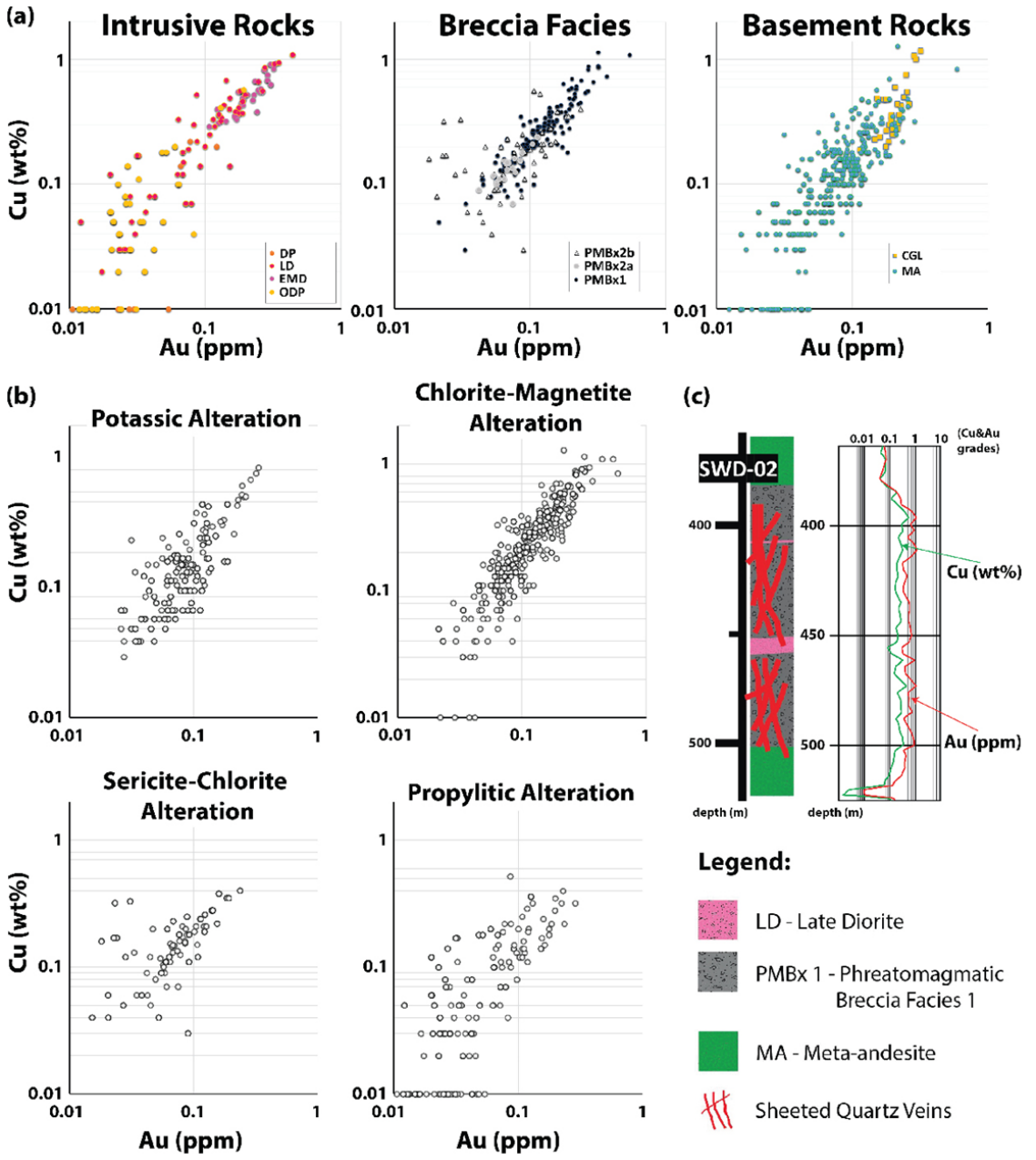

Fig. 13 Plots of copper and gold grades. **(a)** scatter plot of copper and gold grades of the different lithologies in weight percent (wt%) and parts per million (ppm), respectively; **(b)** scatter plot of copper and gold grades of the alteration types in weight percent (wt%) and parts per million (ppm), respectively; **(c)** lithologic and structural plot of drillhole SWD-02 compared with the line graph of copper and gold grades in weight percent (wt%) and parts per million (ppm), respectively. Copper and gold assay data from Philex Mining Corporation (Unpublished).

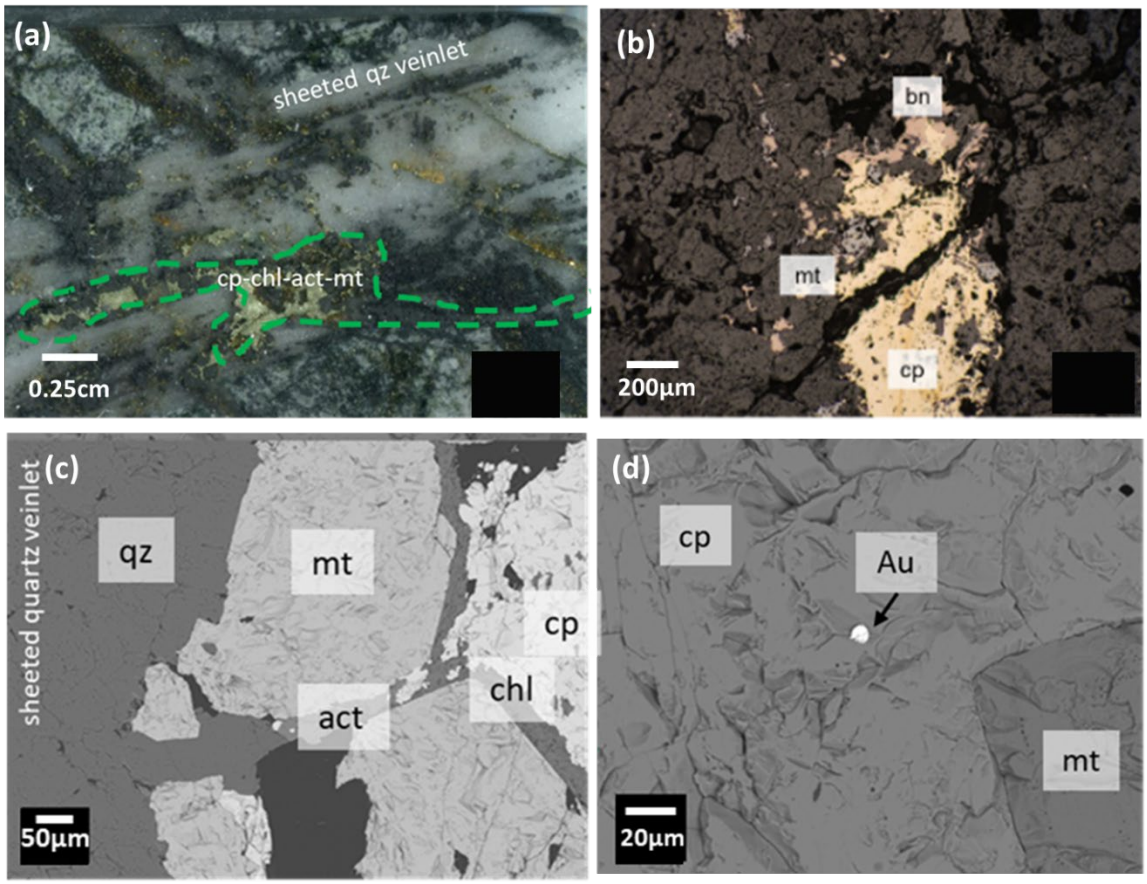

Fig. 14 Occurrence of gold in the Southwest prospect (02-395.10m). (a) overprinting chalcopyrite-rich chlorite-actinolite-magnetite veinlet; (b) association of bornite, chalcopyrite and magnetite in the chalcopyrite-rich veinlet; (c) backscatter image of the chalcopyrite-rich veinlet showing the association of chalcopyrite-magnetite with actinolite and chlorite; (d) backscatter image of the minute gold grain in chalcopyrite.

4 Mineral Chemistry

4.1 Amphibole

Chemical compositions of the amphibole grains from the various intrusive rocks in the Southwest prospect, as well as the actinolite grains occurring with the overlapping chalcopyrite-magnetite-chlorite-actinolite±sericite veinlets were determined (Table 3). The formula units were calculated on the basis of 23 oxygens (Leake et al., 1997), and FeO was considered as total Fe. The amphiboles contain significant Ca ranging between 10.3 and 12.1 wt%, equating to formula units of $Ca_B \geq 1.50$, thus the Ca-amphibole discrimination based on Si contents and X_{Mg} (Mg/[Mg+Fe] atomic) (Leake et al., 1997) was applied (Fig. 15). In general, the cores of the hornblende phenocrysts in all of the intrusive rock types plot in the magnesiohornblende field. These include the cores of the partly altered hornblende phenocrysts rimmed by biotite, actinolite and chlorite in the EMD and faintly rimmed hornblende phenocrysts with large cores in the LD, as well as the cores of hornblende phenocrysts in the ODP and DP. The cores of the hornblende phenocrysts in all of the intrusive rock types consistently have high X_{Mg} values (>0.60) and low Si contents. In contrast, the rims of the hornblende phenocrysts in the EMD and LD plotted in the actinolite field in the Ca-amphibole discrimination diagram (Leake et al., 1997), attributed to the higher Si contents and high X_{Mg} values (>0.60). Chemical compositions of the actinolite associated with the chalcopyrite-chlorite-magnetite-actinolite±sericite were also determined and showed high X_{Mg} values (>0.7), which are slightly higher than those of the hornblende phenocrysts and actinolite rims in the intrusive rocks, as well as high Si content.

Table 3 Chemical composition of amphiboles from the various intrusive rocks in the Southwest prospect.

Sample ID	05-153		02-192.10				02-554.40				02-211		02-395.10	
Lithology	ODP		EMD				LD				DP		cp-mt-chl-act±ser	
Description	core		core		rim		core		rim		core		core	
Number of Analysis	20		5		5		18		17		8		16	
	ave	(±σ)	ave	(±σ)	ave	(±σ)	ave	(±σ)	ave	(±σ)	ave	(±σ)	ave	(±σ)
SiO_2 (wt%)	44.11	(0.58)	43.48	(0.42)	51.43	(4.96)	44.67	(1.77)	50.72	(2.65)	44.24	(0.79)	51.98	(2.09)
TiO_2	1.62	(0.15)	1.64	(0.02)	0.27	(0.42)	1.69	(0.16)	0.97	(0.27)	1.61	(0.18)	0.53	(0.27)
Al_2O_3	9.72	(0.50)	9.68	(0.12)	2.97	(1.63)	9.35	(1.90)	4.52	(2.17)	8.98	(0.53)	1.86	(0.39)
FeO	11.43	(0.41)	14.66	(0.29)	12.26	(0.91)	13.26	(0.93)	9.93	(0.85)	13.16	(0.42)	9.87	(1.14)
MnO	0.50	(0.05)	0.49	(0.06)	0.76	(0.13)	0.46	(0.12)	0.67	(0.16)	0.51	(0.04)	0.32	(0.10)
MgO	12.31	(0.28)	12.11	(0.41)	14.06	(1.10)	13.28	(0.65)	17.04	(1.18)	13.21	(0.45)	17.14	(1.02)
CaO	11.43	(0.07)	10.48	(0.22)	12.80	(0.78)	11.18	(0.38)	10.49	(0.74)	10.95	(0.19)	11.73	(0.42)
Na_2O	1.87	(0.09)	1.83	(0.08)	0.47	(0.35)	2.08	(0.20)	1.20	(0.38)	1.70	(0.14)	0.44	(0.12)
K_2O	0.31	(0.02)	0.30	(0.05)	0.41	(0.06)	0.32	(0.07)	0.24	(0.05)	0.29	(0.03)	0.08	(0.04)
Cl	0.06	(0.01)	0.00	(0.00)	0.00	(0.03)	0.09	(0.03)	0.09	(0.03)	0.09	(0.02)	0.05	(0.03)
=O	0.01		0.00		0.00		0.02		0.02		0.02		0.01	
F	0.09	(0.07)	0.00	(0.00)	0.00	(0.02)	0.13	(0.05)	0.10	(0.05)	0.09	(0.07)	0.00	(0.00)
=O	0.04		0.04		0.00		0.05		0.04		0.04		0.00	
H_2O_{calc}	1.93		1.96		1.95		1.92		1.99		1.91		2.00	
Total	98.10		96.65		98.24		98.30		97.86		96.66		95.83	
cation (O=23)														
Si	6.638	(0.077)	6.646	(0.005)	7.642	(1.957)	6.740	(0.137)	7.455	(0.194)	6.713	(0.084)	7.700	(0.121)
Al_T	1.724	(0.091)	1.744	(0.037)	0.519	(0.665)	1.551	(0.168)	0.694	(0.161)	1.606	(0.101)	0.345	(0.045)
Al_{IV}	1.339	(0.063)	1.354	(0.025)	0.508	(0.459)	1.220	(0.116)	0.629	(0.111)	1.258	(0.069)	0.388	(0.031)
Ti	0.183	(0.018)	0.189	(0.001)	0.030	(2.129)	0.191	(0.019)	0.102	(0.023)	0.183	(0.02)	0.060	(0.031)
Fe	1.790	(0.051)	1.874	(0.054)	1.523	(0.943)	1.683	(0.096)	1.195	(0.094)	1.671	(0.06)	1.295	(0.176)

Mn	0.064	(0.007)	0.063	(0.008)	0.096	(0.064)	0.063	(0.005)	0.086	(0.016)	0.066	(0.005)	0.047	(0.021)
Mg	2.762	(0.062)	2.758	(0.070)	3.115	(2.141)	2.950	(0.134)	3.742	(0.174)	2.987	(0.093)	3.709	(0.283)
Ca	1.843	(0.012)	1.717	(0.021)	2.039	(1.871)	1.773	(0.042)	1.625	(0.116)	1.781	(0.036)	1.830	(0.092)
Na	0.546	(0.028)	0.544	(0.020)	0.135	(0.090)	0.591	(0.046)	0.316	(0.066)	0.501	(0.043)	0.128	(0.029)
K	0.059	(0.005)	0.059	(0.009)	0.077	(0.045)	0.057	(0.005)	0.042	(0.007)	0.056	(0.007)	0.017	(0.002)
Cl	0.015	(0.003)	0.000	(0)	0.000	(0)	0.025	(0.005)	0.006	(0.001)	0.023	(0.005)	0.013	(0.007)
F	0.045	(0.031)	0.000	(0)	0.000	(0)	0.062	(0.026)	0.024	(0.006)	0.045	(0.035)	0.000	(0.000)
X_{Mg}	0.607		0.595		0.672		0.637		0.758		0.641		0.741	

Note: FeO – total Fe content is expressed as FeO; X_{Mg} - atomic Mg/(Mg+Fe); ODP – old diorite porphyry; EMD – Early Mineralization Diorite; LD – Late Diorite; DP – Diorite Porphyry; cp – chalcopyrite; mt – magnetite; chl – chlorite; act – actinolite; ser – sericite.

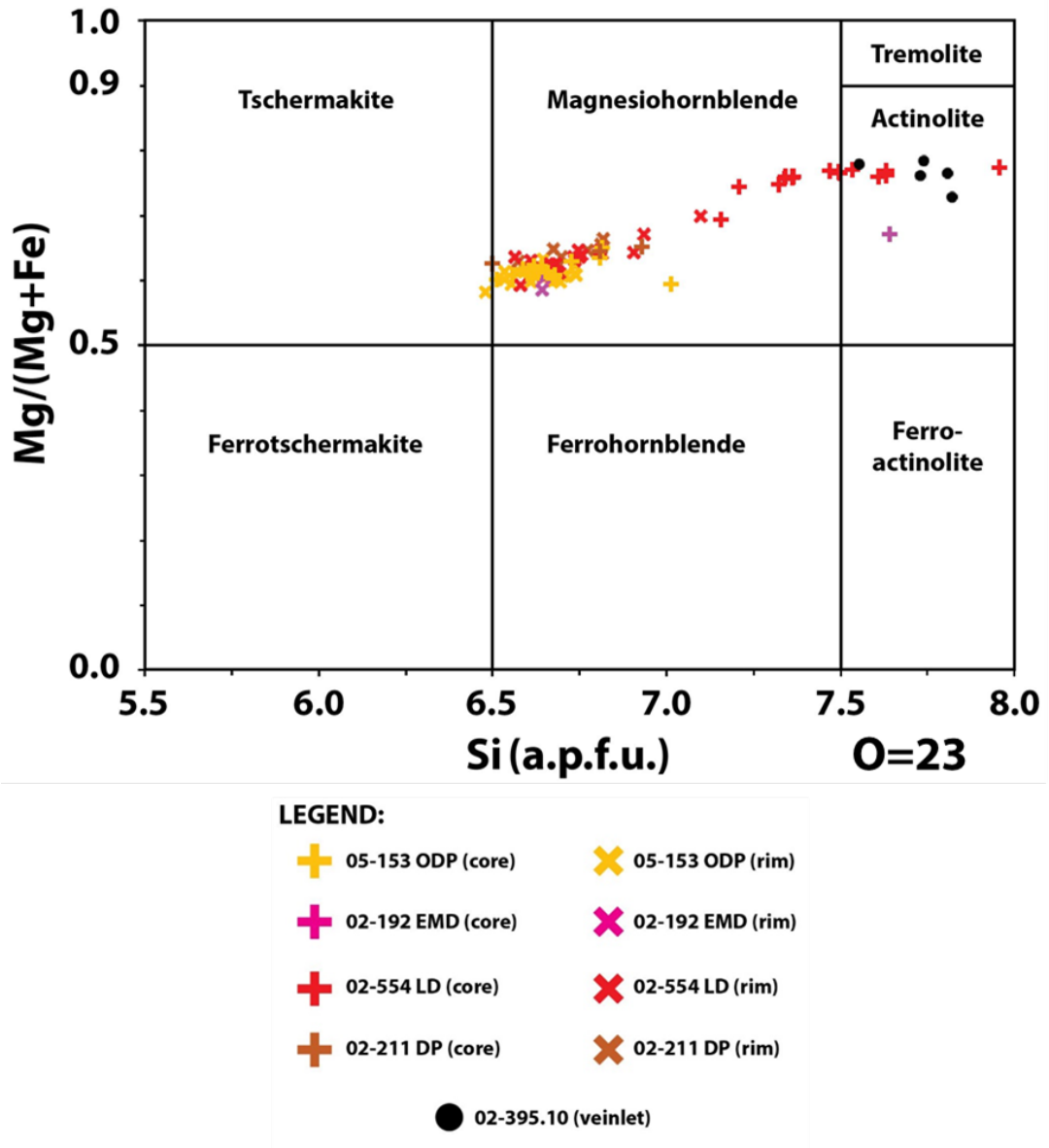

Fig. 15 Chemical compositions of amphibole phenocrysts and cores from the various intrusive rocks in the Southwest prospect plotted in the classification of calcic-amphiboles of Leake et al. (1997).

The significant difference in the Si contents and X_{Mg} values between the cores and rims in the EMD and LD is also observed in the "ore-generating andesite porphyry" of the Sto. Tomas II deposit (Fig. 16; Imai, 2001), as well as, in the intrusive hosts of porphyry copper deposits in Papua New Guinea (Mason, 1978), Solomon Islands (Chivas, 1981) and Mamut, Sabah, Malaysia (Imai, 2000a). This difference was explained by Imai (2001) as an evidence of the decompression that was responsible for exsolution of magmatic fluids out of the hydrous silicate melt (Burnham, 1979; Imai, 2001). Amphibole geobarometer of Hammarstrom and Zen (1986) was applied on the hornblende taking into consideration that Al_T (total Al) content of hornblende is controlled by pressure presuming that hornblende coexist with plagioclase, quartz, magnetite and other rock forming minerals of calc-alkaline rocks (Hammarstrom & Zen, 1986). Al_{IV} (aluminum occupancy in the tetrahedral site) is negatively correlated with Si contents. And Al_{IV} is correlated with Al_T, thus difference in Si contents are correlated with the difference with Al_T content. Amphibole geobarometer applied on the on the cores of hornblende phenocrysts in intrusive rocks in Southwest indicates a formation at maximum pressures of 400MPa or lower during the formation of the igneous calcic amphiboles in the EMD and LD (Fig. 17).

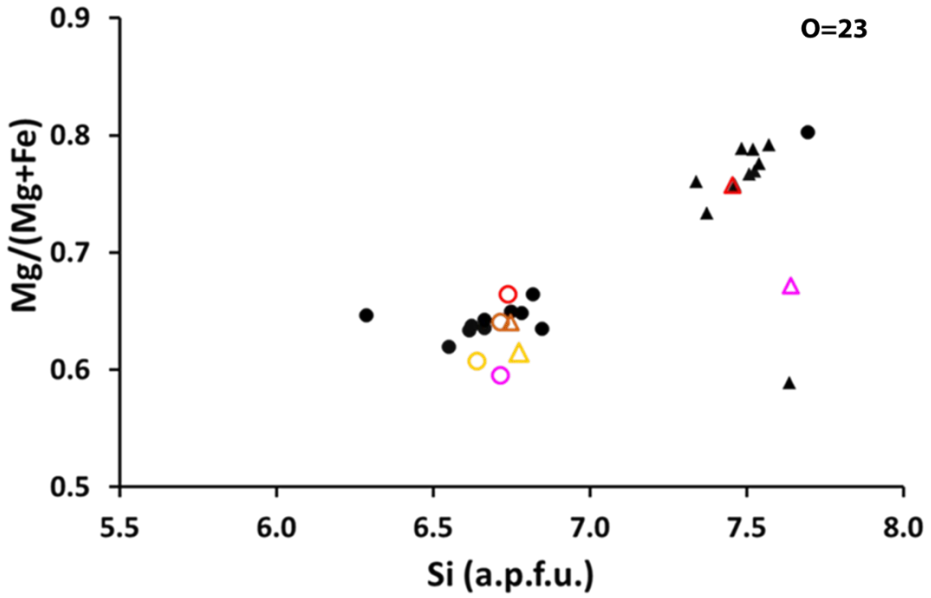

Fig. 16 Scatter plot of the X_{Mg} (atomic Mg/(Mg+Fe) ratios) vs the atomic Si contents per half unit cell of amphibole stoichiometry. Data of Sto. Tomas II cluster (black triangles and circles) from Imai (2001). Note: a.p.f.u. – atoms per formula unit, O=23

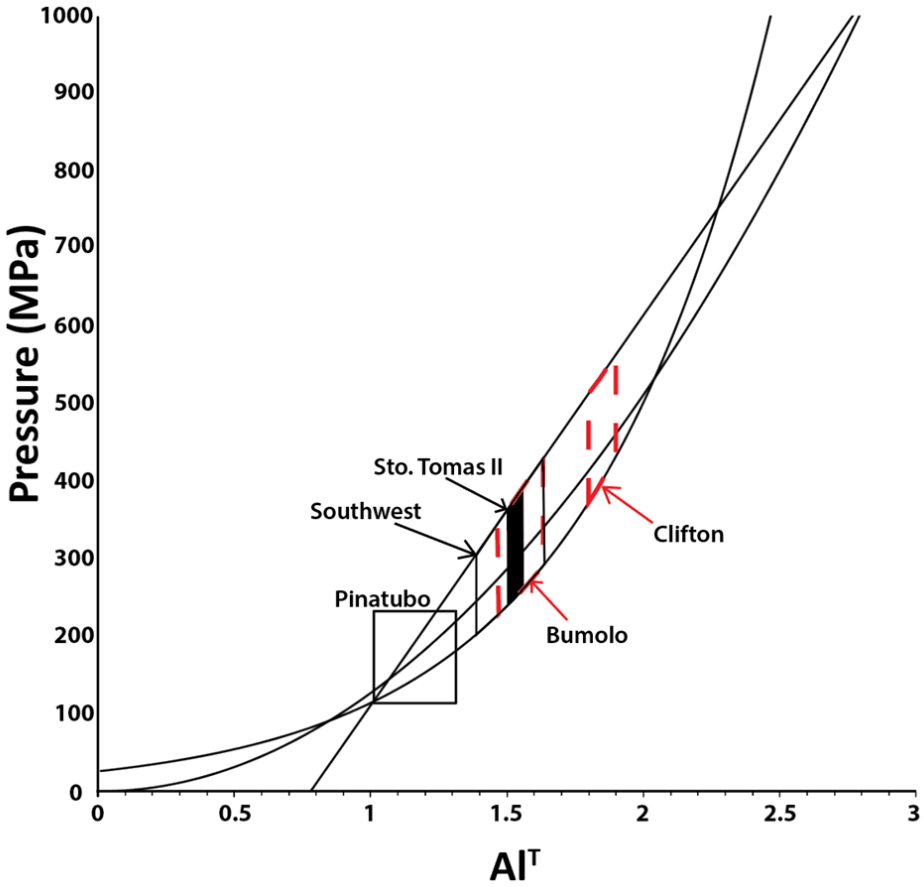

Fig. 17 Amphibole geobarometer (Hammarstrom and Zen, 1986) applied on the cores of the amphiboles of the Southwest prospect, compared with the intrusive rocks of the Sto. Tomas II deposit, Bumolo deposit, Clifton prospect (Imai, 2001) and Mt. Pinatubo (Imai, 1993).

4.2 Biotite

Chemical compositions of the biotites from the potassic alteration that enveloped the EMD and PMBx1 in the Southwest prospect were determined (Table 4). The formula units were calculated on the basis of 22 oxygens, and FeO was considered as total Fe. Recalculation of the mole fractions of phlogopite, proton-deficient oxyannite and annite, and ferric and ferrous iron estimations were done using the Mica^{+} program (Yavuz, 2003). Temperature of formation of the biotites were also estimated using this software on the basis of the biotite geothermometer formulated by Beane (1974).

Results show that the biotites in the potassic alteration are characterized with high Mg contents plotting in between the field of phlogophite and Mg-biotite (Fig. 18) based on the discrimination diagram of Foster (1960).

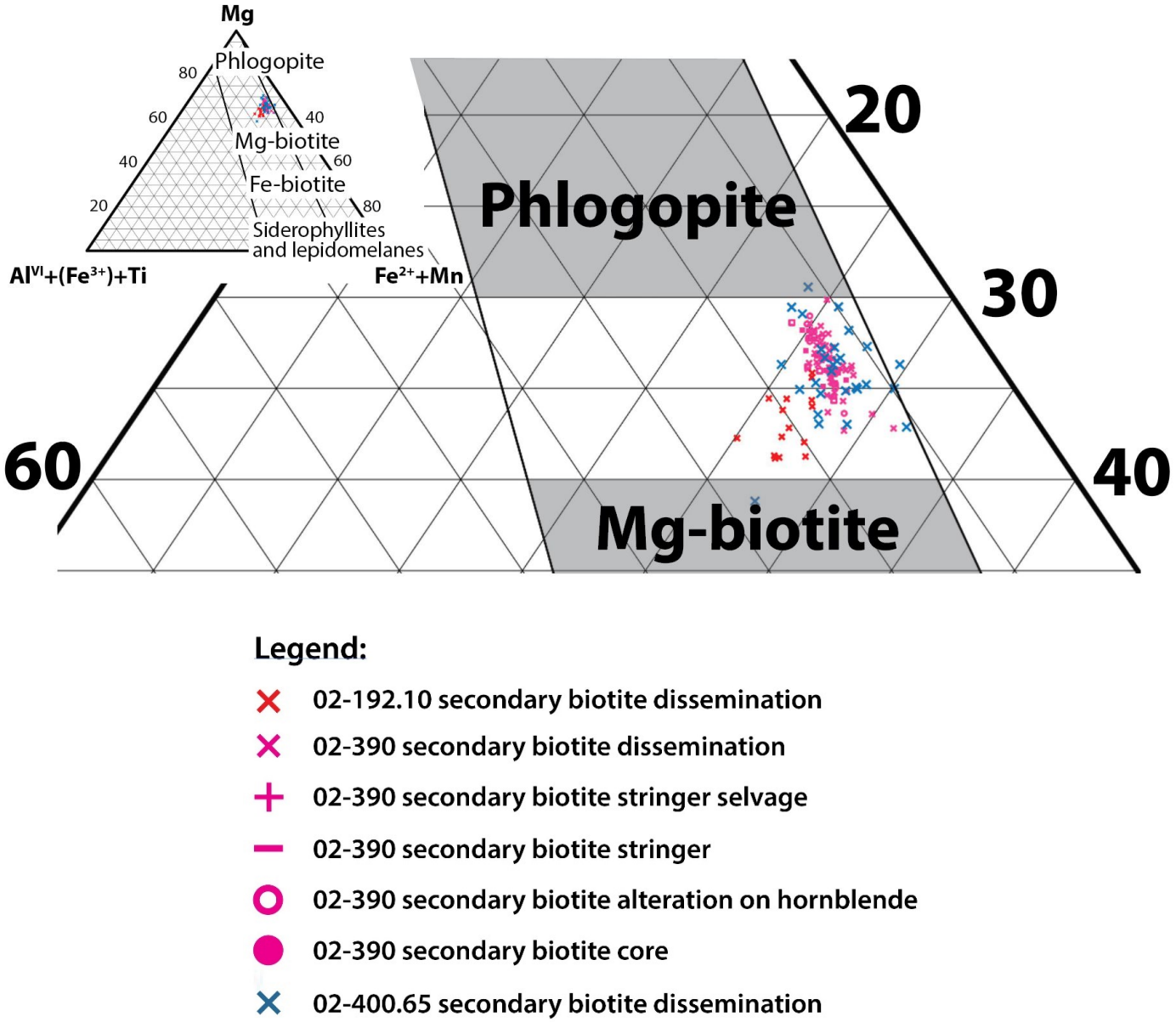

Fig. 18 Chemical compositions of biotites from the potassic alteration in the Southwest prospect plotted in the discrimination diagram of Foster (1960).

Table 4 Chemical composition of biotites in the potassic alteration in the Southwest prospect and biotite geothermometry results.

Sample ID	02-196				02-390								02-400.65	
Lithology	EMD						EMD						PMBx1	
Alteration	2bt dissemination		biotite core		2bt dissemination		2bt alteration on hb		2bt stringer		2bt vein selvage		2bt dissemination	
Number of Analysis	15		17		42		8		3		8		5	
	ave	(±σ)	ave	(±σ)	ave	(±σ)	ave	(±σ)	ave	(±σ)	ave	(±σ)	ave	(±σ)
SiO_2	38.46	(0.92)	38.78	(0.64)	38.82	(0.59)	39.29	(0.71)	38.64	(1.08)	39.06	(0.80)	38.60	(1.38)
Al_2O_3	13.31	(0.33)	12.32	(0.38)	12.26	(0.32)	12.04	(0.43)	13.08	(0.47)	12.16	(0.43)	12.77	(0.46)
TiO_2	3.54	(0.47)	3.69	(0.28)	3.61	(0.32)	3.72	(0.28)	3.61	(0.11)	3.72	(0.26)	3.17	(0.40)
FeO	12.16	(0.54)	12.52	(0.50)	12.54	(0.55)	12.12	(0.48)	12.31	(0.02)	12.44	(0.71)	12.25	(0.78)
MnO	0.32	(0.08)	0.23	(0.09)	0.24	(0.08)	0.25	(0.08)	0.26	(0.02)	0.23	(0.09)	0.18	(0.07)
MgO	16.51	(0.60)	17.71	(0.52)	17.72	(0.56)	17.77	(0.49)	17.38	(0.58)	17.92	(0.53)	17.10	(1.86)
CaO	0.22	(0.25)	0.11	(0.13)	0.11	(0.10)	0.20	(0.05)	0.16	(0.14)	0.14	(0.09)	0.43	(0.20)
Na_2O	0.31	(0.09)	0.27	(0.06)	0.24	(0.06)	0.29	(0.06)	0.30	(0.02)	0.23	(0.04)	0.46	(0.55)
K_2O	5.93	(0.88)	9.27	(0.49)	9.20	(0.55)	8.94	(0.33)	9.25	(0.49)	9.13	(0.44)	7.05	(0.47)
Cr_2O_3	0.00	(0.01)	0.01	(0.01)	0.01	(0.01)	0.01	(0.01)	0.02	(0.01)	0.00	(0)	0.01	(0.01)
P_2O_5	0.01	(0.01)	0.01	(0.06)	0.01	(0.01)	0.00	(0.01)	0.01	(0)	0.00	(0)	0.01	(0.01)
Cl	0.23	(0.02)	0.22	(0.02)	0.22	(0.02)	0.22	(0.01)	0.23	(0.03)	0.22	(0.02)	0.20	(0.03)
=OH(Cl)	0.05	(0)	0.05	(0)	0.05	(0)	0.05	(0)	0.05	(0.01)	0.05	(0)	0.05	(0.01)
F	0.00	(0)	0.00	(0)	0.00	(0)	0.00	(0)	0.00	(0)	0.00	(0)	0.00	(0)
=OH(F)	0.00	(0)	0.00	(0)	0.00	(0)	0.00	(0)	0.00	(0)	0.00	(0)	0.00	(0)
$H_2O_{(recal.)}$	3.90	(0.07)	3.99	(0.04)	3.99	(0.04)	4.00	(0.04)	4.00	(0.10)	4.00	(0.02)	3.93	(0.02)
Total	94.81	2.11	99.03	(0.95)	98.86	(0.99)	98.73	(0.77)	99.15	(2.56)	99.17	(0.46)	96.07	(0.83)
cation (O=22)														
Si	5.819	(0.086)	5.745	(0.065)	5.758	(0.059)	5.812	(0.068)	5.710	(0.002)	5.768	(0.096)	5.813	(0.20)

Al_T	2.374	(0.067)	2.152	(0.069)	2.143	(0.057)	2.099	(0.079)	2.278	(0.020)	2.117	(0.082)	2.268	(0.09)
Ti	0.403	(0.050)	0.412	(0.031)	0.403	(0.036)	0.413	(0.031)	0.401	(0.004)	0.413	(0.030)	0.359	(0.04)
Fe	1.538	(0.058)	1.551	(0.067)	1.556	(0.070)	1.500	(0.066)	1.523	(0.044)	1.537	(0.094)	1.543	(0.10)
Mn	0.040	(0.010)	0.029	(0.011)	0.030	(0.011)	0.031	(0.010)	0.032	(0.002)	0.029	(0.011)	0.023	(0.01)
Mg	3.725	(0.126)	3.911	(0.104)	3.919	(0.115)	3.918	(0.091)	3.829	(0.031)	3.945	(0.104)	3.840	(0.42)
Ca	0.036	(0.042)	0.017	(0.020)	0.018	(0.017)	0.032	(0.007)	0.025	(0.022)	0.021	(0.014)	0.070	(0.03)
Na	0.091	(0.026)	0.078	(0.017)	0.070	(0.019)	0.082	(0.018)	0.086	(0.008)	0.067	(0.011)	0.135	(0.16)
K	1.143	(0.159)	1.752	(0.090)	1.741	(0.099)	1.688	(0.071)	1.744	(0.074)	1.719	(0.085)	1.353	(0.08)
Cr	0.001	(0.001)	0.001	(0.001)	0.001	(0.001)	0.001	(0.001)	0.002	(0.002)	0.000	(0)	0.001	(0)
P	0.015	(0.001)	0.014	(0.001)	0.014	(0.001)	0.014	(0.001)	0.014	(0.001)	0.014	(0.001)	0.013	(0)
Cl	0.030	(0.002)	0.028	(0.003)	0.028	(0.002)	0.027	(0.002)	0.028	(0.003)	0.028	(0.002)	0.201	(0.03)
F	0.000	(0)	0.000	(0)	0.000	(0)	0.000	(0)	0.000	(0)	0.000	(0)	0.000	(0)
X_{Mg}	0.708		0.716		0.716		0.723		0.716		0.720		0.719	
Xphl	0.708		0.716		0.716		0.723		0.716		0.720		0.719	
Xann	0.285		0.314		0.317		0.335		0.278		0.325		0.278	
Xsid	0.130		0.073		0.069		0.051		0.109		0.060		0.099	
Biotite geothermometer (°C)	433		471		471		472		470		472		486	

Note: FeO – total Fe content is expressed as FeO; X_{Mg} – atomic Mg/(Mg+Fe); X_{phl} – mole fraction of phlogopite; X_{dPoxy} – mole fraction of proton-deficient oxyannite; X_{an} – mole fraction of annite

4.3 Chlorite

Chemical compositions of chlorites existing as stringers and vein infill materials contemporaneous with the chlorite-magnetite and propylitic alteration, as well as the chlorites occurring as alteration products of igneous hornblende and secondary biotite representing the propylitic overprint were analyzed. Samples 02-395.10 (magnetite-rich) and 02-408.35 (magnetite-poor) contain abundant chlorite grains that represent the chalcopyrite-chlorite-actinolite±magnetite±sericite veinlets overlapping sheeted quartz veinlets and are contemporaneous with the chlorite-magnetite alteration. Sample 02-471.10, meanwhile, represents the chlorite overprinted over biotite stringers in a banded quartz veinlets in the LD. Chlorites in 02-192.10 overprinted on the biotites of the potassic alteration on the EMD. On the other hand, chlorites in 02-211.10 replaced igneous hornblende of the DP.

In general, chlorites that were formed as stringers in the propylitic alteration are Si-poor, Fe-rich chlorites of ripidolite in compositions (Fig. 19a; Heys, 1954). On the other hand, the chemical compositions of chlorites occurring as stringers associated with chlorite-magnetite alteration is pycnochlorite characterized by higher Si and lower Fe contents, as well as that of the chlorite, which replaced alteration of the igneous hornblende. In contrast, the chemical compositions of chlorite replaced secondary biotite are scattered in the diabanite field (Fig. 19a).

The X_{Mg} values and Si contents of chlorite vary depending on the alteration type and origin (Fig. 19b). X_{Mg} values and Si contents of chlorite stringers that are contemporaneous with the propylitic alteration are the lowest among the chlorite types. X_{Mg} values and Si contents increase systematically towards the chlorites of the chlorite-magnetite alteration, nonetheless, the X_{Mg} values of chlorites of those associated with the

magnetite-rich veinlets are significantly higher. This is possibly due to the decrease in Fe contents of chlorites as a consequence of removal of Fe by magnetite and probably chalcopyrite (Fig. 19c).

Table 5 Chemical composition of chlorites in the alteration assemblages in the Southwest prospect and chlorite geothermometry results.

Sample ID	02-395.10		02-408.35		02-529.10		02-471.10		02-192.10		02-211	
Alteration	chlorite-magnetite		chlorite-magnetite		propylitic		propylitic		chloritic		chloritic	
Number of Analysis	n=4		n=19		n=67		n=30		n=5		n=5	
	ave	(±σ)	ave	(±σ)	ave	(±σ)	ave	(±σ)	ave	(±σ)	ave	(±σ)
SiO_2 (wt%)	28.02	(0.29)	27.91	(0.28)	26.84	(0.68)	26.76	(0.49)	29.37	(1.39)	28.28	(1.50)
TiO_2	0.01	(0.02)	0.03	(0.03)	0.04	(0.04)	0.05	(0.03)	0.10	(0.06)	0.13	(0.15)
Al_2O_3	18.20	(0.25)	17.89	(0.27)	19.34	(0.57)	19.20	(0.31)	17.57	(1.63)	17.99	(0.43)
FeO	16.92	(0.43)	18.35	(0.75)	21.09	(1.17)	19.22	(1.07)	16.38	(1.22)	16.08	(1.33)
Cr_2O_3	0.00	(0.01)	0.02	(0.03)	0.01	(0.02)	0.02	(0.03)	0.01	(0.02)	0.02	(0.02)
MnO	0.82	(0.06)	1.27	(0.31)	1.01	(0.26)	0.95	(0.23)	0.64	(0.35)	0.72	(0.26)
MgO	21.63	(0.27)	19.32	(0.69)	18.27	(1.04)	18.44	(0.90)	20.59	(1.23)	21.27	(1.79)
CaO	0.03	(0.04)	0.08	(0.05)	0.04	(0.03)	0.02	(0.01)	0.38	(0.28)	0.14	(0.12)
Na_2O	0.01	(0.01)	0.03	(0.03)	0.02	(0.02)	0.02	(0.02)	0.07	(0.09)	0.05	(0.09)
K_2O	0.01	(0.02)	0.03	(0.02)	0.01	(0.01)	0.02	(0.03)	0.09	(0.12)	0.10	(0.11)
H_2O_{calc}	11.61	(0.11)	11.40	(0.08)	11.50	(0.21)	11.32	(0.10)	11.59	(0.07)	11.53	(0.36)
total	97.42		96.34		98.66		96.02		96.78		96.30	
cation (O=14)												
Si	2.895	(0.014)	2.937	(0.025)	2.799	(0.039)	2.835	(0.031)	3.037	(0.144)	2.940	(0.07)
Al^{IV}	1.105	(0.014)	1.063	(0.025)	1.201	(0.039)	1.165	(0.031)	0.963	(0.144)	1.060	(0.07)
Al^{VI}	1.112	(0.011)	1.156	(0.024)	1.176	(0.032)	1.234	(0.026)	1.177	(0.088)	1.147	(0.04)
Ti^{VI}	0.001	(0.001)	0.003	(0.002)	0.003	(0.003)	0.004	(0.003)	0.008	(0.005)	0.010	(0.01)
Fe	1.462	(0.036)	1.614	(0.066)	1.840	(0.112)	1.704	(0.103)	1.416	(0.103)	1.403	(0.16)
Cr	0.000	(0.001)	0.002	(0.002)	0.001	(0.001)	0.001	(0.003)	0.001	(0.001)	0.001	(0.002)

Mn	0.072	(0.006)	0.113	(0.028)	0.089	(0.023)	0.086	(0.021)	0.056	(0.031)	0.064	(0.03)
Mg	3.332	(0.028)	3.031	(0.097)	2.840	(0.135)	2.913	(0.128)	3.173	(0.203)	3.294	(0.18)
Ca	0.003	(0.004)	0.009	(0.006)	0.003	(0.003)	0.002	(0.002)	0.042	(0.031)	0.016	(0.01)
Na	0.002	(0.002)	0.005	(0.005)	0.003	(0.004)	0.003	(0.003)	0.014	(0.018)	0.010	(0.02)
K	0.001	(0.003)	0.005	(0.003)	0.001	(0.002)	0.003	(0.004)	0.011	(0.015)	0.014	(0.01)
X_{Mg}	0.695		0.650		0.601		0.631		0.691		0.701	
T (°C)-Cathelineau (1988)	294	(5)	276	(17)	325	(13)	314	(10)	248	(27)	279	(10)
T (°C)-Jowett (1991)	293	(5)	277	(16)	327	(13)	315	(10)	248	(27)	279	(11)

Note: FeO – total Fe content is expressed as FeO; X_{Mg} – atomic Mg/(Mg+Fe).

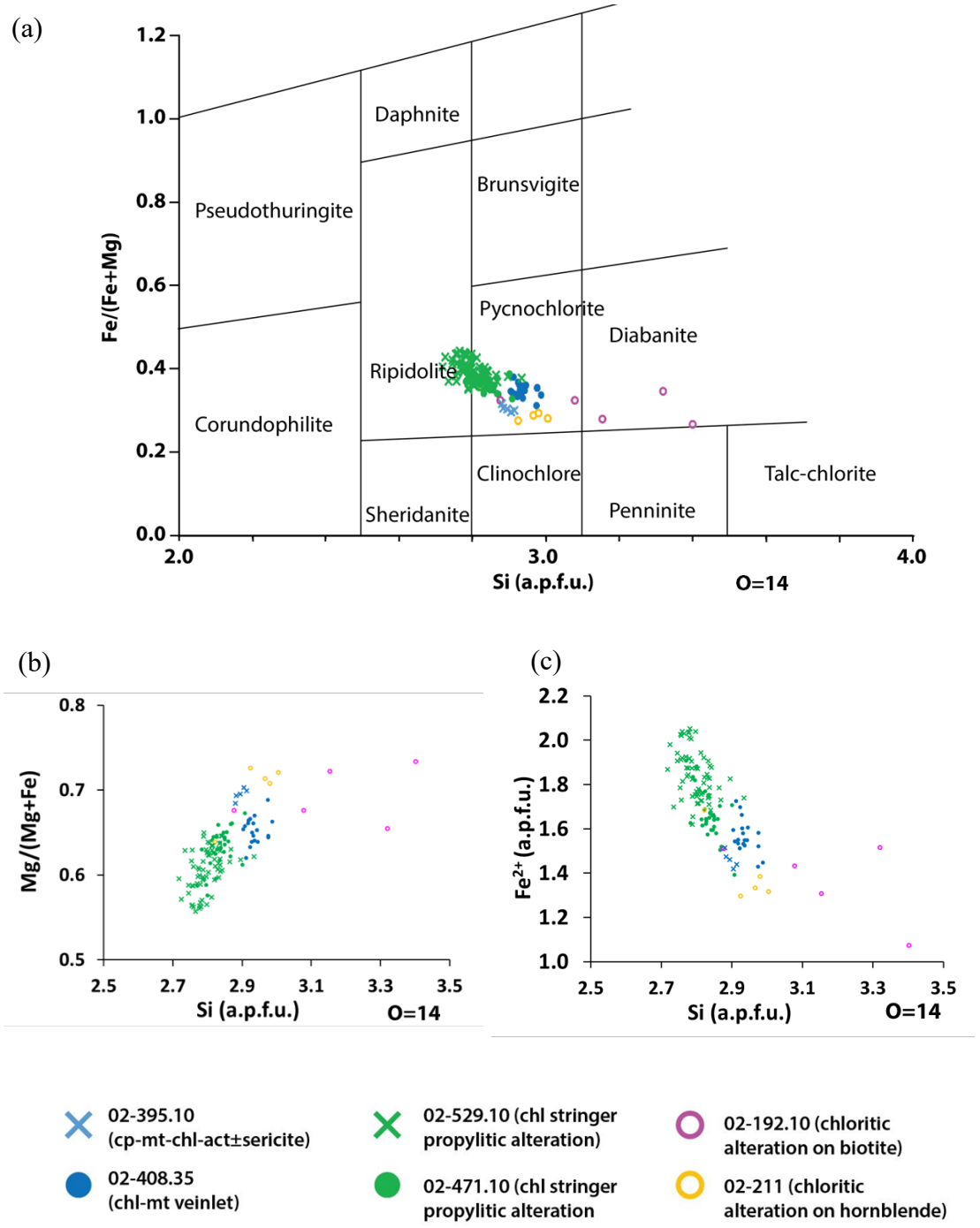

Fig. 19 Chemical compositions of chlorite from the various alteration types in the Southwest prospect. (a) chlorite from the chlorite-magnetite, propylitic and chlorite alteration of igneous hornblende and secondary biotite plotted in the classification of chlorites of Heys (1954), (b)

scatter plot in the Mg/(Mg+Fe) vs Si diagram, (c) scatter plot in the Fe^{2+} vs Si diagram. Note: a.p.f.u. – atoms per formula unit, O=14.

5 Characteristics of hydrothermal alteration

5.1 Formation temperature of hydrothermal alteration and veinlets

The chlorite-magnetite and the sericite-chlorite assemblages are typically quartz-free assemblages. Chlorite is, however, ubiquitous so that the chlorite empirical geothermometer was applied to estimate the temperature of formation (e.g., Cathelineau, 1988; Jowett, 1991). On the other hand, the temperature formation of the potassic alteration was evaluated using the biotite geothermometer of Beane (1974). Fluid inclusion studies employed in this study are focused on the quartz-bearing vein types, which are abundant in the potassic and propylitic alteration. Six samples were selected representing the vein types: granular quartz veinlet, sheeted quartz veinlet and gray banded quartz veinlet from the potassic alteration, drusy quartz veinlet and crystalline quartz veinlets from the propylitic alteration. Two of the sheeted quartz veinlet samples, were collected from the central deeper portion of the prospect hosted in the PMBx1, referred in this text to as the deep sheeted quartz veinlets, while the other sheeted quartz veinlet was collected at the shallower northern periphery of the prospect hosted in the MA, referred to as the shallow sheeted quartz veinlets.

5.1.1 Biotite geothermometry

Based on measured chemical compositions of the biotites in the previous section, formula units, and molar fractions of phlogopite (X_{phl}), proton-deficient oxyannite (X_{pDoxy}) and annite (X_{an}) (Table 4, Fig. 20), representing the substitutions of Mg^{2+} - Fe^{2+} - and Fe^{3+} in the biotites (Beane, 1974).

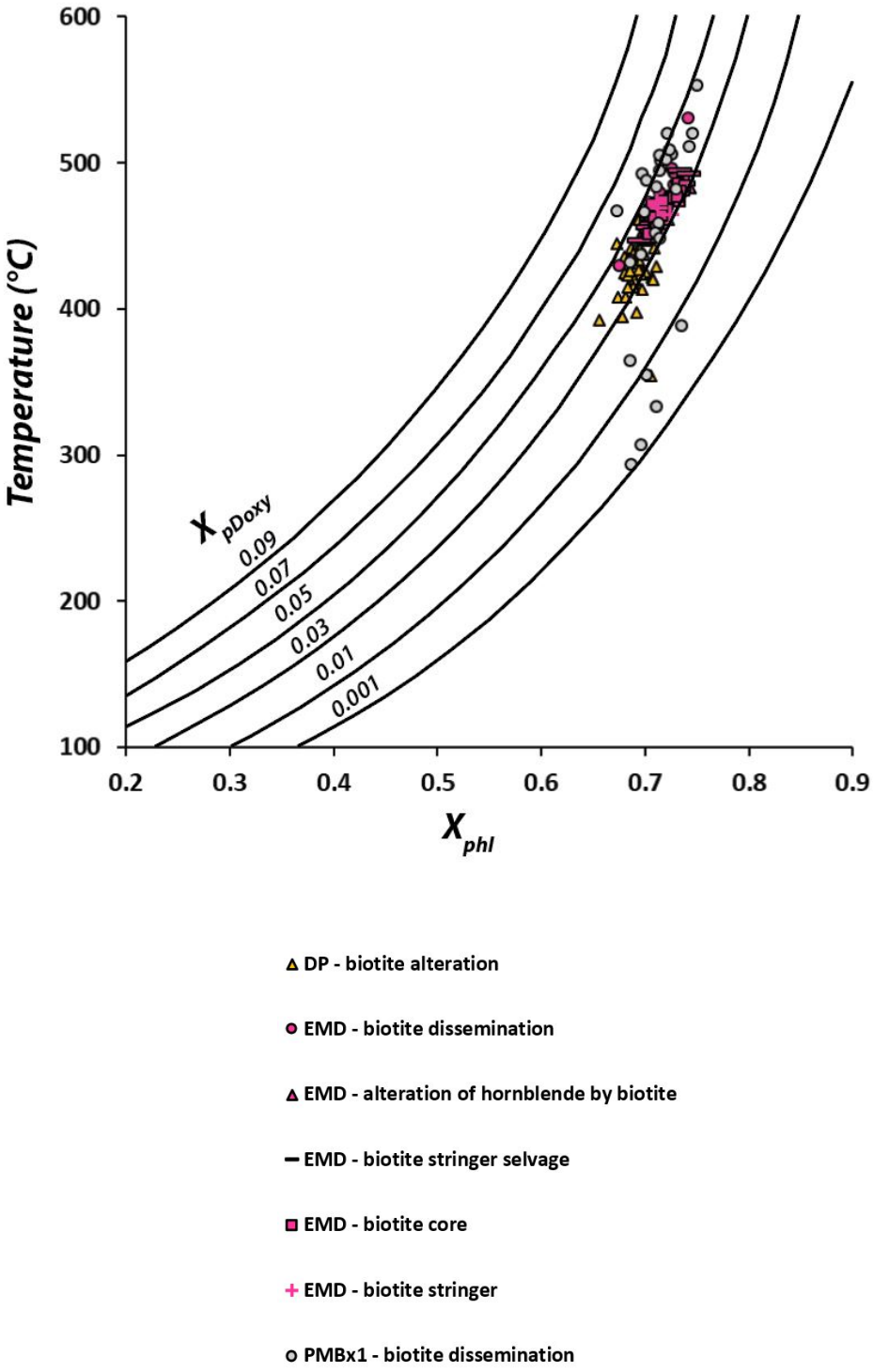

Fig. 20 Compositions of biotite from the various occurrence of potassic alteration in the EMD and PMBx1plotted on the X_{phl} and Temperature (°C) diagram of Beane (1974). The contours indicate the fixed mole fractions of the proton-deficient oxyannite. Abbreviations

denote: X_{phl} = mole fraction of phologite; X_{pDoxy} = mole fraction of proton-deficient oxyannite; DP = Diorite Porphyry, EMD = Early Mineralization Diorite, PMBx1 = Phreatomagmatic Breccia Facies 1

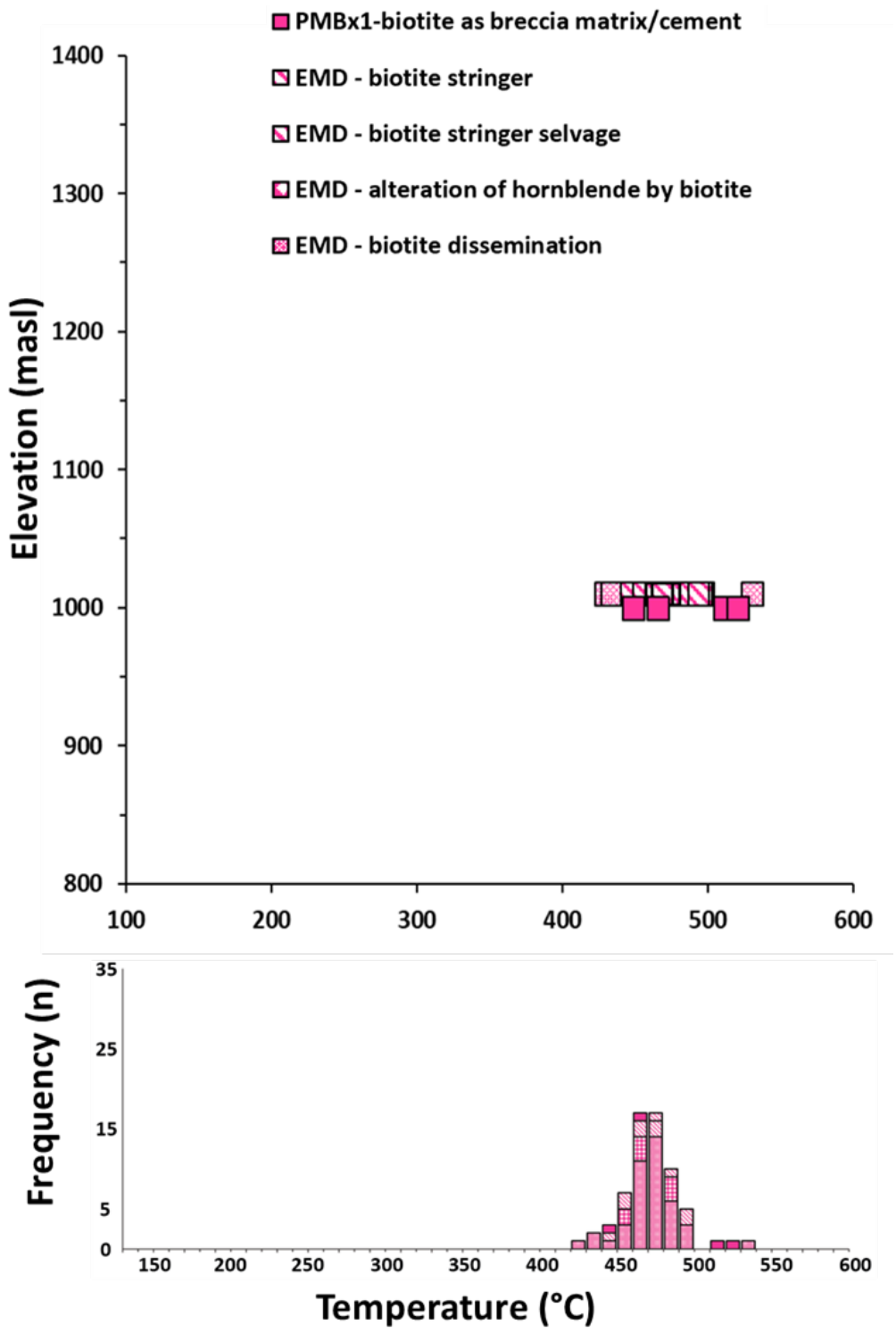

Fig. 21 Histogram of the estimated temperature from the biotite geothermometry applied on the biotites of the potassic alteration occurring as groundmass/matrix disseminations, alteration of hornblende, stringer and stringer selvages in the Southwest prospect cross-referenced with elevation. Abbreviations denote: chl – chlorite, mt – magnetite, act –

actinolite. Abbreviations denote: DP = Diorite Porphyry, EMD = Early Mineralization Diorite Porphyry, PMBx1 = Phreatomagmatic Breccia Facies 1.

Results show a consistent range of temperatures of formation of biotites in the potassic alteration in the EMD, while a wide range is indicated in the PMBx1. Biotites occurring as disseminations in the groundmass, stringers and stringer selvages in EMD were formed between 410°C and 510°C (Fig. 21). Two temperature ranges were indicated by the biotites in the PMBx1, one between 440°C and 540°C, another between 300°C and 400°C. Biotites in the DP that formed as an alteration of hornblende were estimated to form between 400°C and 480°C.

5.1.2 Chlorite geothermometry

Previous workers suggested that Al_{IV} (a.p.f.u.) in chlorites systematically increases at the expense of Si_{IV} with increasing temperature of formation in various geological environments (e.g. McDowell & Elders, 1990; Cathelineau & Nieva, 1985; Cathelineau, 1988; Jahren & Aagaard, 1989; Hillier & Velde, 1991; De Caritat et al., 1993). The Al_{IV} content of chlorites has also been suggested to be independent from any variations in the composition of the host rocks and thus applicable to a wide range of geological environments, including hydrothermal systems (Cathelineau, 1988; Caritat et al., 1993). The relationship between the Al_{IV} content of chlorite and the temperature established by Cathelineau (1988) is as follows:

$$\mathbf{T\ (°C) = -61.92 + 321.98\ Al_{IV}}$$

Based on measured chemical compositions of the chlorites in the previous section, formula units, including Al_{IV} were calculated based on 14 oxygens (Table 5). Results of the chlorite geothermometer of Cathelineau (1988) show a varying range of temperatures

of formation of chlorites depending on the origin and alteration types. Chlorites occurring as stringers in the propylitic alteration (sample ID's: 02-529.35 and 02-471.10) were formed approximately at temperatures between 320°C and 330°C (Fig. 22). Chlorites associated with the chlorite-magnetite alteration (sample ID's: 02-395.10 and 02-408.35) were formed at lower temperature range from 290°C to 300°C. Nevertheless, chlorites that are alteration products of igneous hornblende (sample ID: 02-211.00) and secondary biotite (sample ID: 02-192.10) have widely varying results from 258°C to 317°C and 130°C to 300°C, respectively. This is probably due to the variation in the Al contents of the original mineral, and subsequent low-temperature alteration.

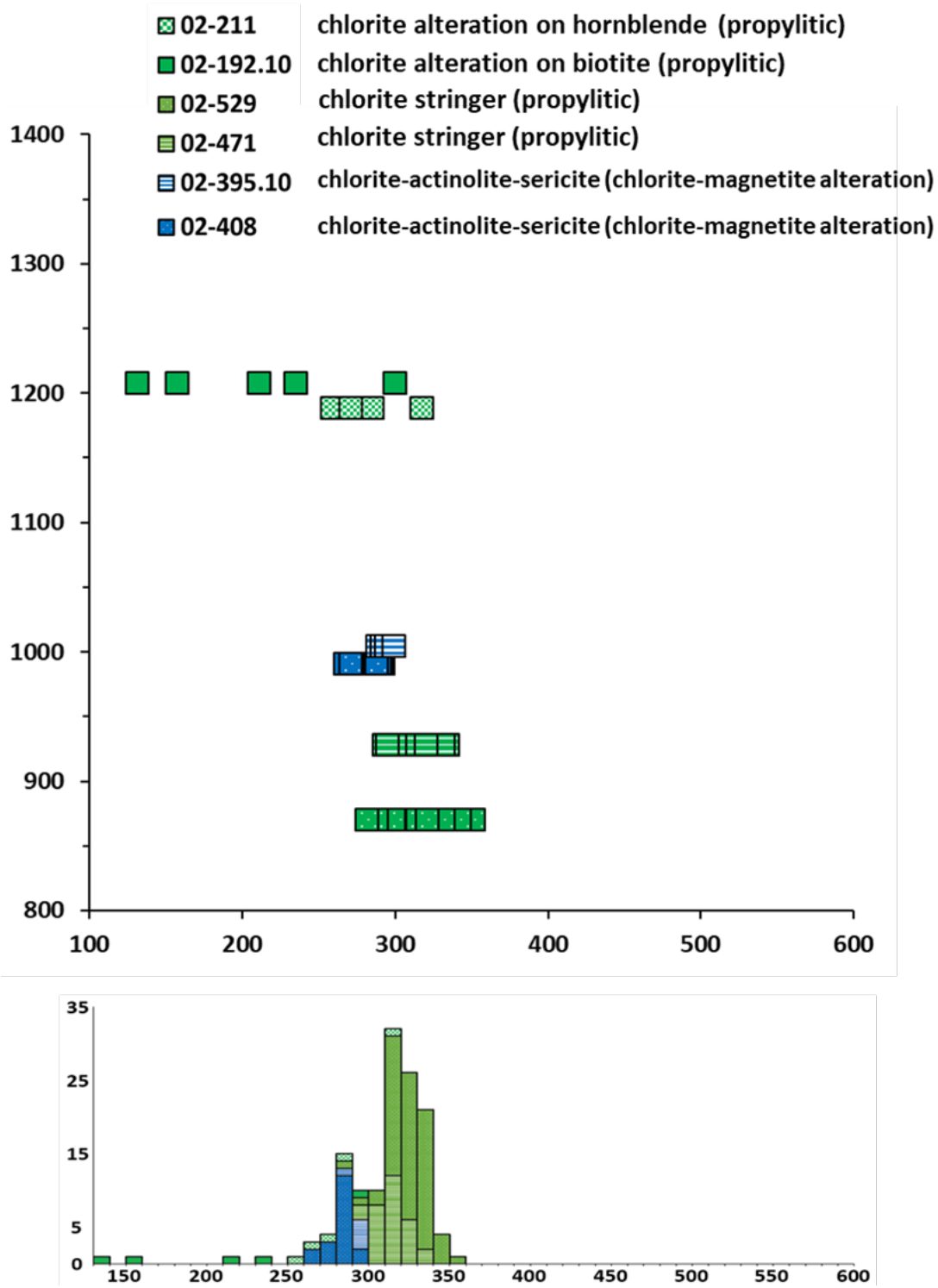

Fig. 22 Histogram of the estimated temperature from the chlorite geothermometry of Cathelineau (1988) applied on the chlorite from the chlorite-magnetite, propylitic and chlorite alteration of igneous hornblende and secondary biotite in the Southwest prospect

cross-referenced with elevation. Abbreviations denote: chl – chlorite, mt – magnetite, act – actinolite.

5.1.3 Fluid Inclusion Studies

The quartz-bearing vein types in the Southwest prospect contain abundant polyphase hypersaline fluid inclusions, which can be classified into at least two types: the liquid-rich (LR) and the vapor-rich (VR) types (Fig. 23a, Table 6). Vapor-liquid ratio in the fluid inclusions widely varies, particularly in the LR types, wherein vapor content can be as low as 10% to as high as 50%. The liquid-rich type has two sub-types, LR-a and LR-b, and are distinguished from one another by the presence of solid components other than halite in the fluid inclusions. LR-a contains a vapor phase, a liquid phase and a halite daughter crystal, while LR-b contains one or more unidentified solid phases, in which one could be sylvite, in addition to hematite and the others as Fe-, Ca-bearing chloride (c.f. Cirineo 2017). Likewise, vapor-rich type inclusions are classified into VR-a and VR-b sub-types. VR-a is usually dominated by a vapor phase, and also typically contains a solid phase, which is most likely halite. On the other hand, vapor content of VR-a type inclusions ranges from 60 to 90%. In contrast to the VR-a, VR-b contains vapor-phase and liquid-phase only, while the vapor-liquid ratio does not vary and remains only between 80 and 90%. VR-b fluid inclusions are similar to the low density, gas-rich fluid inclusions common in porphyry copper deposits (Nash, 1976; Ahmad & Rose 1980).

The fluid inclusion assemblage of the sheeted-shallow veinlet quartz (sample ID: 05-153.20) found at the shallower levels mostly consists of LR-a and LR-b with variable vapor-liquid proportions and scarce VR-b (Fig. 23b). Fluid inclusions of about 20 to 40% vapor are more dominant as compared to the those with less than 10% vapor. The fluid inclusions contain opaque daughter minerals and various salt phases that dissolved at

different temperatures when heated. Hematite daughter crystals are also present but are not abundant.

In contrast, the fluid inclusion assemblage of the sheeted-deep veinlet quartz (sample ID: 02-395.10) consists of LR-a, LR-b and VR-a types and rarely VR-b in the trail of fluid inclusions (Fig. 23c). The vapor-liquid ratio in the fluid inclusions also vary widely. In the LR-a and LR-b, vapor content varies from 10% to 50% and the assemblage is dominated by fluid inclusions with 40% vapor content. Meanwhile, VR-a inclusions typically contain 70-90% vapor with the dominance of those having 80% vapor. Opaque phases, most likely pyrite and chalcopyrite and red hematite flakes are contained and abundant.

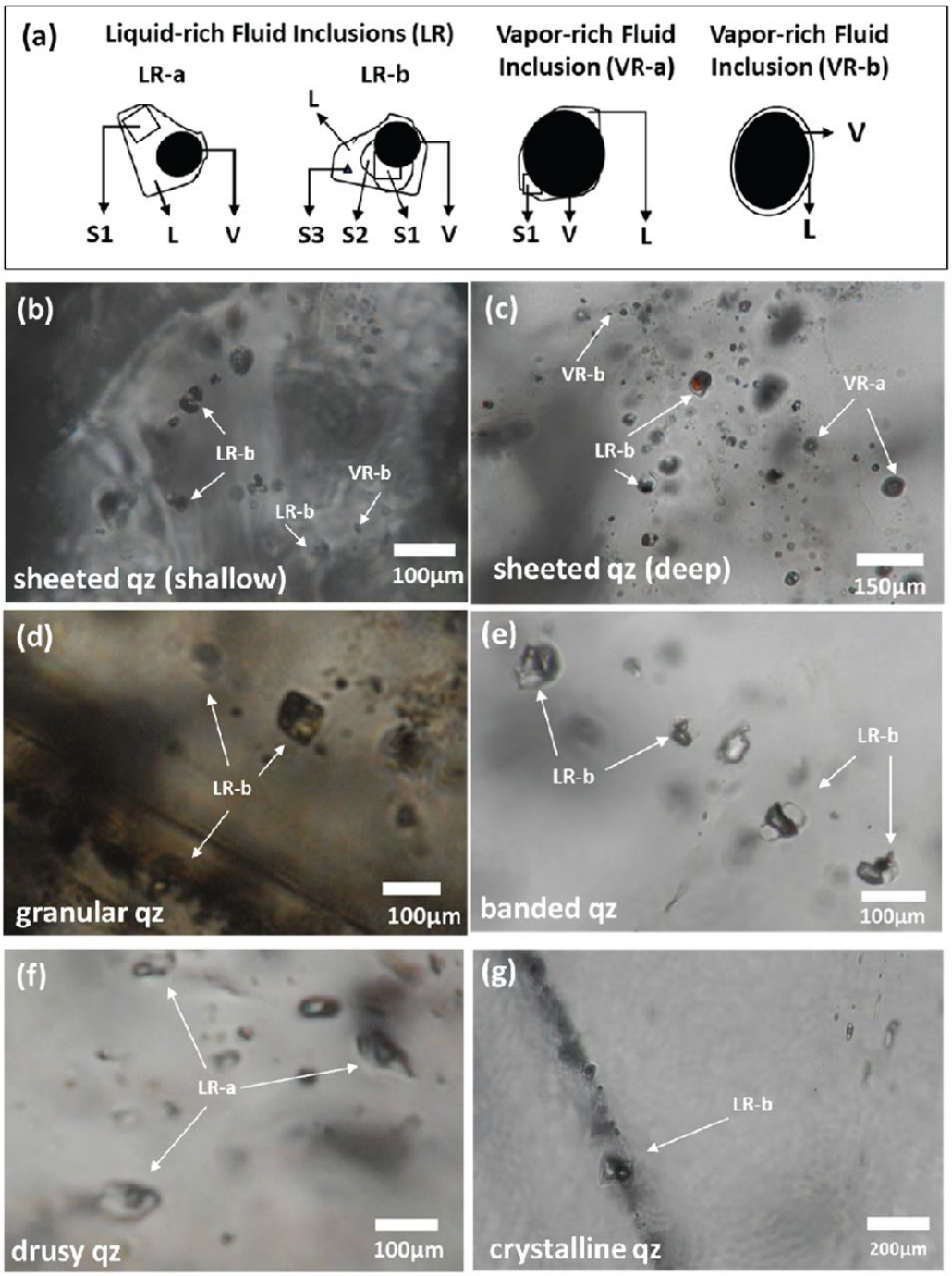

Fig. 23 Fluid inclusion assemblages found in the quartz veinlets of the Southwest prospect. (a) sketch of the fluid inclusion types: LR-a and LR-b are liquid-rich polyphase hypersaline fluid inclusions, VR-a is a liquid-rich polyphase hypersaline, while VR-b is a vapor-rich low-density fluid inclusion; (b) LR-b and VR-b fluid inclusions in shallow sheeted quartz veinlet (05-153.2), (c) LR-b, VR-a and VR-b fluid inclusions in deep sheeted quartz veinlet

(02-395.10), (d) LR-b fluid inclusions and a trail of secondary fluid inclusions of LR-b in granular quartz veinlet (02-401), (e) LR-b fluid inclusions in banded gray quartz veinlet (02-387.5), (f) drusy quartz veinlet containing LR-a fluid inclusions (02-387.5) and, (g) crystalline quartz veinlet with LR-b fluid inclusions and liquid-rich two phase fluid inclusions (02-472.05). Abbreviations denote: qz – quartz and mt – magnetite.

In the granular quartz veinlets in the PMBx1 (sample ID: 02-401.00), the trails of fluid inclusions are abundant LR-a and LR-b type fluid inclusions, dominated by the fluid inclusions with 30% vapor content. LR-a fluid inclusions also appear to form a trans-granular trail (Fig. 23d), indicating a possibility of being secondary and/or pseudo-secondary fluid inclusions. VR-a type inclusions with 60% vapor are also present but are not abundant (Table 6).

The gray quartz banded quartz veinlet hosted in the LD (sample ID: 02-387.50) also contain abundant LR-a and LR-b type inclusions in its trails of fluid inclusions. LR-a and LR-b type inclusions are dominated by fluid inclusions with 30% vapor (Fig. 24e), though the range also widely varies from 10% to 50%. VR-b fluid inclusions are also present but are not abundant. Red hematite flakes and opaque daughter minerals are also contained in the fluid inclusions but are not as abundant as those found in the sheeted quartz veinlets. Various transparent salt phases are also present.

The vuggy quartz veinlet re-opened the banded quartz veinlets in this sample (02-387.50). It also contains LR-a and LR-b fluid inclusions but are dominated by fluid inclusions with 10 to 20% vapor content (Fig. 24f). Opaque daughter minerals are rare, as well as the hematite flakes. The most abundant fluid inclusions in this veinlet are the two-phase liquid-rich type inclusions.

Lastly, crystalline quartz veinlet in the LD (sample ID: 02-472.00), contains trails of polyphase hypersaline fluid inclusions, which are classified as LR-a and LR-b with 10 to 40% vapor content dominated by those having about 40% vapor. Pseudo-secondary trails of two-phase liquid-rich type fluid inclusions are the most abundant (Fig. 24g).

Heating experiments on the different types of polyphase hypersaline fluid inclusions indicated that almost all of the fluid inclusions homogenize by the liquid-vapor homogenization. A small number of fluid inclusions, particularly those hosted in the crystalline veinlet quartz in the LD reach the final homogenization by halite dissolution. It was also observed that further heating at around 450° resulted in the conversion of red hematite flakes to opaque. Upon quenching, the converted hematite flakes did not revert to its original red hues. Several solid phases identified as salts other than halite were also observed to dissolve at between 210 and 420°C (Table 6). Salinity was calculated using the dissolution temperature of halite (T_d) by the equation of Sterner et al. (1988) for fluid inclusions that homogenize by liquid-vapor homogenization.

Liquid-vapor homogenization temperatures [T_h(L-V)] on the polyphase hypersaline fluid inclusions of LR-a and LR-b types in the granular quartz veinlets hosted in the EMD (sample ID: 02-401.00) exceed 720°C (Fig. 24). The measured T_d widely vary from 375°C to 513°C and cluster at 414°C. The salinity of the fluid inclusions in this vein type is 48.7 wt% $NaCl_{eq}$ (Table 6).

Table 6 Fluid inclusion assemblages, microthermometric results and estimated salinity and pressure of homogenization of the liquid-rich fluid inclusion in the Southwest prospect.

Vein type	Depth (m)	Elevation (masl)	Host Rock	opaque phase	hematite	LR-a	LR-b	VR-a	VR-b	minimum T_h (°C)	T_h mode (°C)		T_d mode (°C)	Salinity (Wt% NaCl eq)
granular quartz	401.0	+1065.6	EMD	O	O	8	4	0	2	**---**	**721**	**>**	**414**	**48.7**
shallow sheeted quartz	153.2	+1313.4	MA	O	O	27	9	0	2	**559**	**615**	**>**	**445**	**52.5**
deep sheeted quartz	395.1	+1071.5	PMBx1	O	O	32	49	18	6	**436**	**721, 640**	**>**	**551, 366, 340**	**67, 41**
banded gray quartz	387.5	+1079.1	LD	O	O	6	36	0	4	**687**	**721**	**>**	**520, 570**	**62.7, 70.0**
drusy quartz	387.5	+1079.1	LD	X	X	9	3	0	0	**177**	**337**	**>**	**196**	**31.6**
crystalline quartz	472.05	+994.6	LD	X	X	12	3	0	0	**246**	**263**	**<**	**317**	**35.5**

Note: LR – liquid-rich fluid inclusions; VR-vapor-rich fluid inclusions; T_h mode – mode of homogenization temperatures; T_d mode– dissolution temperatures of halite; masl – meters above sea level; EMD – Early Mineralization Diorite, MA – Meta-andesite, PMBx1 - Phreatomagmatic Breccia Facies 1; LD – Late Diorite

Polyphase hypersaline fluid inclusions of the sheeted quartz veinlet in the MA (sample ID: 05-153.20) at the shallower levels homogenized to liquid at the minimum T_h(L-V) 559°C for the LR-b fluid inclusions, and minimum T_h(L-V) 580°C for the LR-a fluid inclusions (Fig. 24). All fluid inclusions were homogenized by the disappearance of the vapor bubble. Several transparent salt phases were also present and the Td clustered at 445°C. The calculated salinity is 52 wt% NaCleq.

The homogenization and dissolution temperatures of halite of polyphase hypersaline fluid inclusions of the sheeted quartz veinlet in the PMBx1 (sample ID: 02-395.10) at the deeper levels range widely. However, T_h(L-V) of the LR-a fluid inclusions homogenized by the disappearance of the vapor bubble between the values of >720°C and 554°C (Fig. 24). Two groups of T_h(L-V) of the LR-b fluid inclusions were observed, one in between >720°C and 681°C, and the other widely spread in between 552°C and 436°C. The minimum T_h(L-V) of the LR-a and LR-b fluid inclusions are 554°C and 436°C, respectively (Fig. 24). Two modes of T_d of LR-a and LR-b fluid inclusions were measured, one at approximately 551°C and the other at 366°C. The mode of T_h(L-V) and T_d of VR-a fluid inclusions are 640°C and 340°C, respectively. The widely varying T_h(L-V) and T_d of the fluid inclusions in this veinlet type have delineated at least two fluids with salinities of 67 and 41wt% NaCleq.

The mode of T_h(L-V) of polyphase hypersaline fluid inclusions of the banded vein in the LD (02-387.50) is >720°C for all fluid inclusion types and a minimum T_h(L-V) of 687°C (Fig. 24). However, statistical analyses indicate bimodal distribution of T_d, one at about 520°C and the other at about 570°C on LR-a fluid inclusions with corresponding salinities of 62 and 68 wt% $NaCl_{eq}$, respectively. On the other hand, T_h(L-V) and T_d of

the fluid inclusions on the vuggy quartz veinlets (02-387.50) are low and the T_h (L-V), T_d and salinities are clustered at 337°C, 196°C and 31.6 wt% $NaCl_{eq}$, respectively.

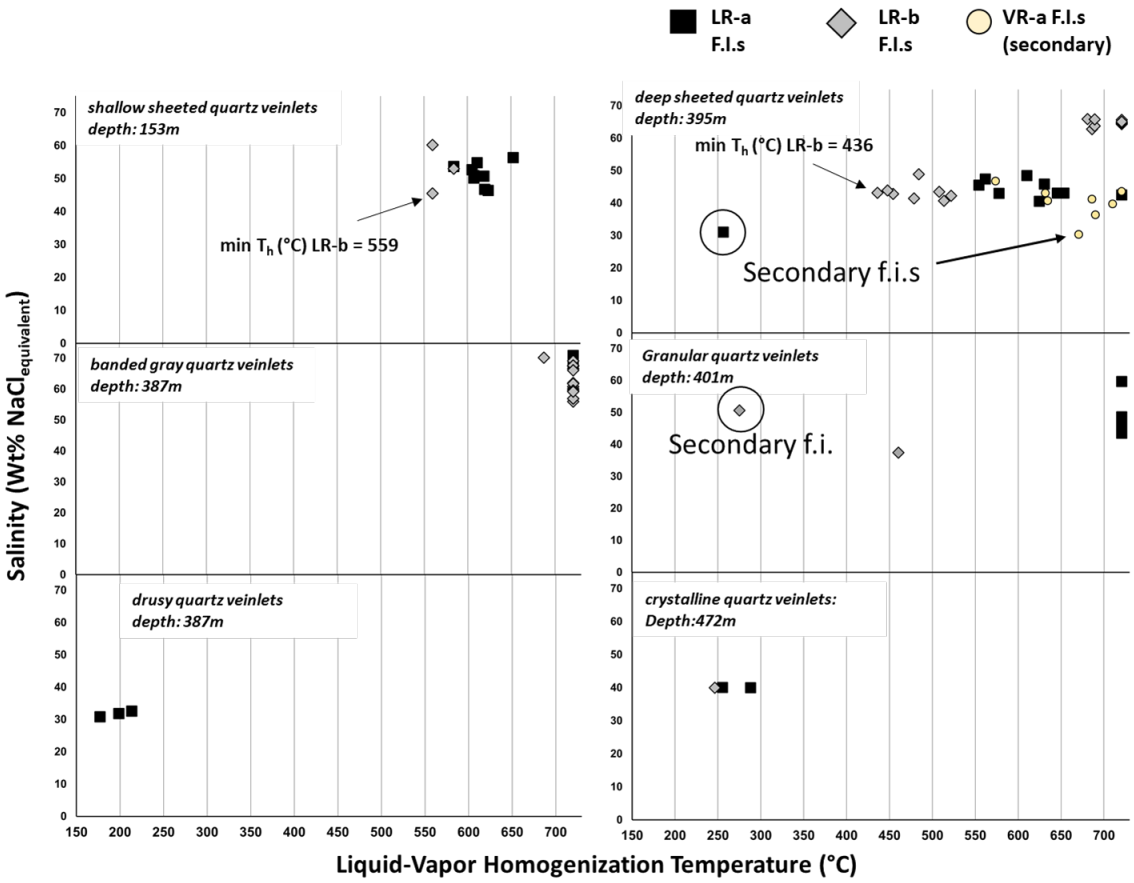

Fig. 24 Salinity vs L-V homogenization temperatures plot showing the results of the heating experiments on the polyphase hypersaline fluid inclusions. Abbreviations denote: LR – liquid-rich fluid inclusions; VR – vapor-rich fluid inclusions.

Lastly, polyphase hypersaline fluid inclusions of the crystalline quartz veinlets in the LD consistently homogenize through halite dissolution. The T_h(L-V), T_d and salinity are clustered at of 263°C, 317°C and 35.5 wt% NaCleq, respectively. The T_h(L-V) of two-phase liquid-rich fluid inclusions with no visible salt at room temperature is 345°C (Fig. 24).

5.2 Veinlet off-setting relationships

The off-setting relationships of veinlets in the Southwest prospect were counted individually particularly downhole along the drillholes SWD-02 and SWD-17-07 and were tabulated in a Vein Off-setting Matrix (Fig. 25) (e.g. Seedorff & Einaudi, 2004). The matrix was configured, such that the veinlets listed in the columns represent the veinlets that were offset, thus older in timing. On the other hand, those that were listed in the rows represent the younger offsetting veinlets. The veinlets were also arranged based on the assumed temperature of formation from highest to lowest based the associations with the hydrothermal assemblage (Seedorff et al., 2005; Sillitoe, 2010).

The majority of the vein-off setting relationship (255 out of 317) documented show off-setting of the veinlets in the potassic alteration by veinlets contemporaneous with the chlorite-magnetite and sericite-chlorite alteration, indicating normal off-setting by the lower temperature veinlets. The results also show off-setting relationships of veinlets within the potassic alteration, corresponding to 54 out of the 317 documented off-setting relationships, indicated as the yellow field in the Vein Off-setting Matrix (Fig. 25). Furthermore, veins contemporaneous with the potassic alteration were observed to off-set lower temperature veinlets in the chlorite-magnetite alteration, such as chlorite-magnetite veinlets being off-set by magnetite-biotite and gray-banded veinlets in the PMBx1 facies, indicated in the Vein Off-setting Matrix as the orange field corresponding to 8 out of 229 (Fig. 25). These reverse off-setting relationships were observed particularly in the EMD, indicating a repetitive vein formation as a result of prolonged duration of the crystallization and cooling of the EMD. Nonetheless, the reverse off-setting relationships in the EMD are limited with respect to the normal ones, suggesting

that the time gap between the syn-mineralization and late-mineralization porphyry intrusions (c.f. Sillitoe, 2010) could have not been significant.

			Assemblage of Offsetting Veinlets (Lower Temperature)															
			Potassic							Chlorite-Magnetite			Sericite-Chlorite		Propylitic			
		Minimum Estimated Formation Temperature (°C)	>720	>720			436	430			280				290	330	160	
		Method	fim	fim			fim	btth			chlth				chlth	fim	fim	
			qz+/-mt	gray qz (banded)	qz-K-spar	qz (wispy)	qz (sheeted)	mt-bt	qz (re-opened)	chl-mt	chl-act-mt	chl-ser	ser-chl	py-chl	chl	qz (crystalline)	qz (vuggy)	cal
Assemblage of Veinlets that was Offset (Higher Temperature)	Potassic	qz+/-mt	60	7		4	9	31		9	10	4	5		14			
		gray qz (banded)	5			2		10							4			
		qz-K-spar	2					2										
		qz (wispy)	9	3			2	7			3				4			
		qz (sheeted)	1					2		10	40				4	1		
		mt-bt	4	2		8	1			15	15							
		qz (re-opened)		3													1	
	Chlorite-Magnetite	chl-mt		3				2		1					3			
		chl-act-mt																
		chl-ser																
	Sericite Chlorit	ser-chl																
		py-chl																
	Propylitic	chl		1														
		qz (crystalline)																1
		qz (vuggy)																
		cal																

Fig. 25 Vein Offsetting Matrix of veinlets contemporaneous with the hydrothermal alteration. Yellow field indicates veinlets associated potassic alteration cut one another, while the orange field indicate chlorite-magnetite veinlets offset by veins associated with potassic alteration. Columns represent the veins that are offset, while rows are the offsetting veinlets. Modified from Seedorf and Einaudi (2004). Abbreviations mean: mt – magnetite; bt – biotite; qz – quartz; K-felds – K-feldspar; chl – chlorite; ser – sericite; py – pyrite, chl – chlorite, act-

actinolite, epi – epidote; fim – fluid inclusion microthermometry; btth – biotite geothermometry (Beane, 1974), chlth – chlorite geothermometry (Cathelineau, 1988).

5.3 Sulfur isotope systematics

Sulfur isotopic ratios of chalcopyrite and pyrite were analyzed. Due to the significant lack of sulfates, only the sulfur isotopic ratios of sulfide grains were analyzed. Some chalcopyrite grains are fine-grained and are inter-locked with bornite, particularly those which are associated with the earlier-formed veinlets such as the sheeted-deep quartz veinlets and granular quartz veinlets. The analyzed sulfides from these samples were a mixture of chalcopyrite and bornite. Chalcopyrite-bornite mixture was also collected from the sheeted-shallow quartz veinlets from the shallow portions of the prospect. This veinlet was overprinted by chlorite-sericite-pyrite stringers associated with sericitic alteration. Sulfur isotopic ratios of the pyrite concentrate from these stringers were also determined. Some of the chalcopyrite concentrates were also collected from the coarse-grained chalcopyrite-rich veinlets associated with magnetite and trace bornite, with chlorite-magnetite alteration overprint on the crenulated sheeted quartz veinlets near the contact between the PMBx1 and LD. On the other hand, pyrite concentrates were collected from later stage pyrite-rich veinlets associated with propylitic and sericitic alteration.

The $\delta^{34}S$ of the sulfides range from +1.8‰ to +5.1‰, and most of the data lie in between +2.8‰ and +4.6‰ (Table 7, Fig. 26). The $\delta^{34}S$ remain broadly constant throughout the vertical extent of the prospect. Furthermore, the $\delta^{34}S$ of sulfides from various vein stages overlapped. The $\delta^{34}S$ of sulfides associated with the earlier vein assemblage consisting of the granular quartz veinlets and sheeted-deeper quartz veinlets range from +1.8‰ to +4.1‰, while the $\delta^{34}S$ of sulfides of the sheeted-shallow quartz

range from +3.0‰ and +4.1‰. The $\delta^{34}S$ of sulfides contemporaneous with the chlorite-magnetite alteration consisting of the chalcopyrite-rich veinlet fall in between +3.9‰ and +4.1‰. $\delta^{34}S$ of late stage pyrite in the propylitic alteration and hydrothermal breccia cement on the PMBx2b range from +2.8‰ to +5.1‰.

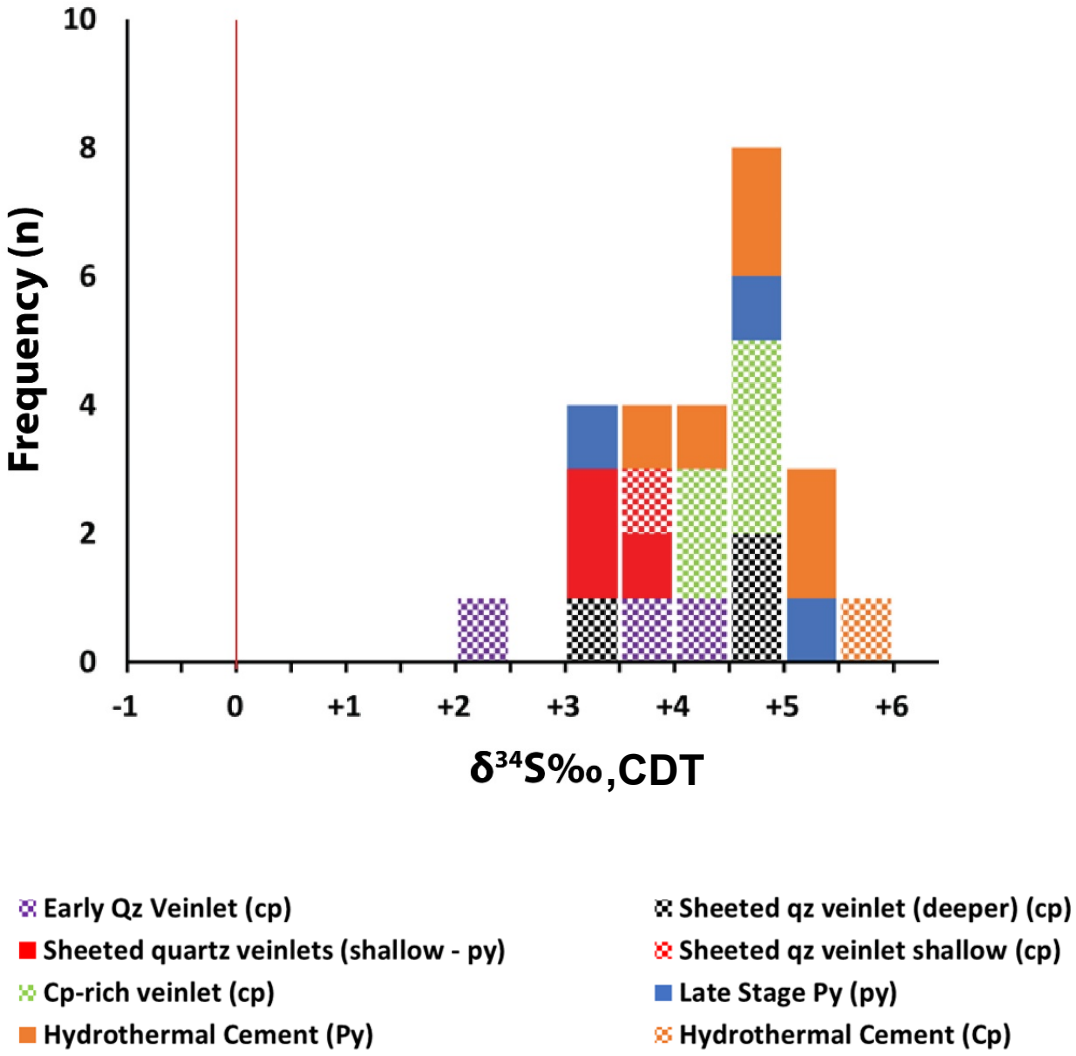

Fig. 26 Histogram showing the distribution of $\delta^{34}S$ values $\delta^{34}S$ of chalcopyrite (hatched pattern) and pyrite (solid color) associated with the different vein types in the Southwest prospect.

Table 7 Sulfur isotope analysis on the sulfides associated with veinlets in the Southwest prospect.

Sample ID	Elevation (masl)	Host Rock	Mineral	Host / Veinlet Association	$\delta^{34}S$ (‰)
11-102.20	+1428.6	MA	chalcopyrite	granular quartz	+1.8
11-117.50	+1413.3	MA	chalcopyrite	granular quartz	+3.0
11-110.35	+1420.5	MA	chalcopyrite	granular quartz	+4.0
07-377.20	+1089.4	PMBx1	chalcopyrite	deep sheeted quartz	+2.8
02-401.40	+1065.2	EMD	chalcopyrite	deep sheeted quartz	+4.1
02-401.40	+1065.2	EMD	chalcopyrite> bornite	deep sheeted quartz	+4.1
05-153.30a	+1377.5	MA	chalcopyrite	shallow sheeted quartz	+2.9
05-153.30	+1377.5	MA	chalcopyrite> bornite	shallow sheeted quartz	+2.9
05-153.30	+1377.5	MA	pyrite>chalcopyrite	shallow sheeted quartz	+3.1
05-153.30b	+1377.5	MA	pyrite	shallow sheeted quartz	+3.1
02-459.70	+1006.9	PMBx1	chalcopyrite	chalcopyrite-magnetite-chlorite-actinolite±sericite	+4.1
02-395.40	+1071.2	PMBx1	chalcopyrite	chalcopyrite-magnetite-chlorite-actinolite±sericite	+4.3
02-409.70	+1056.9	PMBx1	chalcopyrite	chalcopyrite-magnetite-chlorite-actinolite±sericite	+3.9
02-395.40	+1071.2	PMBx1	chalcopyrite> bornite	chalcopyrite-magnetite-chlorite-actinolite±sericite	+4.3
02-409.70	+1056.9	PMBx1	chalcopyrite> bornite	chalcopyrite-magnetite-chlorite-actinolite±sericite	+3.9
11-99.40a	+1431.4	MA	pyrite	pyrite-chlorite	+2.8
07-505.55	+961.1	LD	pyrite	pyrite-chlorite	+4.3
02-177.25	+1289.4	LD	pyrite	pyrite-chlorite	+4.8
08-273.40a	+1172.5	PMBx2b	pyrite	hydrothermal breccia cement	+3.3
07-390.40a	+1076.2	PMBx2b	pyrite	hydrothermal breccia cement	+4.1
08-71.55	+1374.3	PMBx2b	pyrite	hydrothermal breccia cement	+4.4
08-65.30	+1380.6	PMBx2b	pyrite	hydrothermal breccia cement	+4.6
08-64.75	+1381.1	PMBx2b	pyrite	hydrothermal breccia cement	+4.6
08-105.85	+1340	PMBx2b	pyrite	hydrothermal breccia cement	+3.9
02-398.55a	+1068.1	PMBx1	chalcopyrite>>>bornite	hydrothermal breccia cement	+5.1

Note: EMD – Early Mineralization Diorite, LD – Late Diorite, MA – Meta-andesite, PMBx1 – Phreatomagmatic Breccia Facies 1, PMBx2b – Phreatomagmatic Breccia Facies 2b.

6 K-Ar radiometric dating

K-Ar ages were determined on mineral concentrates from two samples: (1) secondary biotite concentrates from the EMD and (2) hornblende concentrates from the LD.

The EMD sample was from SWD-17-02 197.00m, which is intensely hydrothermally biotitized, typical at the potassic alteration of the Southwest prospect. The body of the EMD at this elevation was interpreted to be a megaclast in one of the phreatomagmatic breccia facies, which is older than the LD based on crosscutting relations. Under the microscope, hornblende grains were completely altered by shredded polyaggregates of secondary biotite. On the other hand, the LD sample was from SWD-17-07 554.00m, which is located at the central deeper portion interpreted to be the least altered core of the intrusion. Hornblende grains are not hydrothermally altered.

K-Ar ages on both samples are 3.5±0.3Ma (Table 8). The results also show that most of the excess ^{40}Ar is due to the atmospheric Ar that was adsorbed on the grain boundaries and microfractures of the analyzed mineral concentrates.

Table 8 K-Ar Age determinations on the hand-picked mineral concentrates of the selected intrusive rocks in the Southwest prospect.

Sample ID	Rock Type	Mineral Concentrate	K_2O(wt %)±σ	^{40}Ar rad, (ng/g)	%^{40}Ar air	K-Ar Age(Ma)
02-196	fine-grained diorite porphyry (bt-EMD)	secondary biotite	0.481±0.010	0.119±0.005	94.0	3.5±0.3
07-554	medium-grained diorite porphyry (LD)	hornblende	0.435±0.010	0.104±0.003	93.0	3.5±0.3

Note: (bt) denotes hydrothermally biotitized sample. Abbreviations denote: EMD – Early Mineralization Diorite, LD – Late Diorite.

The returned ages on the early mineralization and late mineralization phases of diorite porphyries are the same, indicating one of the three possible scenarios: (1) multiple phases of intrusive and the magmatic-hydrothermal events in the Southwest prospect are short-lived and have occurred in a span of less than 300 thousand years, or (2) the two diorite porphyries (EMD and LD) maybe part of a single intrusive phase but different pulses, (3) K-Ar age of the older event was reset by an overprinting thermal event.

7 Discussion

7.1 Evolution of hydrothermal system in the Southwest prospect

The intrusive rocks and breccias at the Southwest prospect principally consist of at least three episodes of intrusions, co-eval breccias of magmatic-hydrothermal and phreatomagmatic events and overlapping porphyry copper-type quartz veins onto the volcano-sedimentary sequence of Pugo and Zigzag Formations. Each of the group of intrusions and breccias defines a timeline in the development of the porphyry copper-type mineralization in the Southwest prospect.

The timeline defined by the pre-mineralization volcanic and intrusive rocks, the KTP and ODP, however, have not been constrained by any age dating methods yet. Nevertheless, spatial and temporal relationships with the country rocks should indicate that this timeline is not related to the development of porphyry copper mineralization in the Southwest prospect, and that the KTP is supposedly coeval with the CGL. Most of the exposures of the ODP are found at the shallow levels, based on the exposures on outcrop and drillcores. This led to the interpretation that the ODP at the surface could be a pre-mineralization sill that is probably associated with the widely distributed “Hornblende Andesite Body” overlying the CGL and Klondyke Formation in around the Southwest prospect.

The timeline corresponding to the early stage of the development of porphyry-type copper mineralization is defined by a series of intrusions that were altered by potassic alteration dominated by secondary biotite accompanied with magnetite, chlorite, epidote and rare K-feldspar with chalcopyrite and bornite (Fig. 12). These rocks have consistent grades greater than 0.20% and 0.3ppm of copper and gold, respectively. Quartz veining

with abundant magnetite (e.g. granular quartz and sheeted-shallow quartz veinlet) and potassic alteration enveloped the EMD and adjacent wallrocks, inducing a biotite alteration halo in the peripheries. Granular and sheeted quartz are abundant in the EMD, where they occur as sinuous and crenulated veinlets, such as the granular quartz veinlet sample at 02-401.00. These veinlets were supposed to have been developed at the H_2O-saturated carapace of the EMD, the top portion of the intrusion wherein the rising EMD magma is supposed to separate pressurized fluid rich in volatile components (Burnham, 1969, 1979; Burnham & Ohmoto, 1980). Multi-directional granular quartz veinlets representing the multi-directional stockworks deposited as radial and concentric veinlets on the host rocks (Seedorff et al., 2005) are clearly observed in the shallow peripheral CGL rocks coincided with elevated copper and gold grades as well as the sheeted-shallow quartz veinlet hosted in the MA (Fig. 27a). This occurrence probably suggests multiple forceful intrusion of the EMD, imparting incipient fractures and joint patterns to the wallrocks, depositing several cycles of vein formation. This interpretation is consistent with the evidence of offsetting contemporaneous veinlets in the potassic alteration from the offsetting matrix of veinlets (Fig. 25), which suggests multiple intrusion events within the paragenetic stage (Sillitoe, 2010), despite the information obtained from the K-Ar age estimates, which probably suggests a short gap or instantaneous break in between the syn-mineralization and late-mineralization intrusions. However, the likelihood of thermal reset in the recorded age of the secondary biotite is more reasonable also due to the overprinting of veinlets. Explosive brecciation affected the EMD (e.g. Burnham, 1968, 1979; Burnham & Ohmoto, 1980). represented as hydrothermally-altered, breccia pipes (EMDBx) that were formed adjacent to the EMD, and transitionally changed to the PMBx1 toward the shallower levels. As a result, the breccia facies are dominated by the

EMD fragments and to a lesser degree, by the MA fragments and various quartz vein fragments of various shapes and sizes, including the granular and sheeted quartz-magnetite veinlets. Randomly-oriented granular veinlets, as well as subvertical sheeted quartz veinlets, the sinuous and crenulated porphyry-type veinlets that overprint the PMBx1, sourced from the EMD magma while the breccia facies are still not solidified (Fig. 27a).

The intrusion of the LD defines the late-mineralization in the Southwest prospect (Fig. 27b). The LD is encountered to be in contact with the EMD and PMBx1 at the central deeper portion adjacent to its supposed apical portion. The apical portions are hosted by crenulated banded quartz veinlets with widespread sericitization and chloritization. The adjacent rocks, mainly consisting of the PMBx1 are pervasively altered by chlorite-magnetite alteration, rather than potassic alteration. This results in the formation of veinlets contemporaneous with the chlorite-magnetite alteration, including the chalcopyrite-magnetite-chlorite-actinolite±sericite veinlets (Fig. 12) that overprinted the earlier formed veinlets, particularly the subvertical sheeted quartz veinlets and fill the fractures in the PMBx1.

The late development of the hydrothermal system is represented by intrusion of barren porphyry dikelets (DP), diatreme brecciation of the PMBx2 and pebble dikes, and sericite-chlorite-pyrite hydrothermal alteration (Fig. 27c). The PMBx2 may have rooted from the DP suggested by the presence of the ODP, EMD, LD and DP clasts. The PMBx1 clasts may also be present but identification was obscured by alteration and weathering. Late hydrothermal alteration in the PMBx2 is present as cavity infills and cement in the breccias consisting of sericite, chlorite, calcite and coarse-grained pyrite cubes.

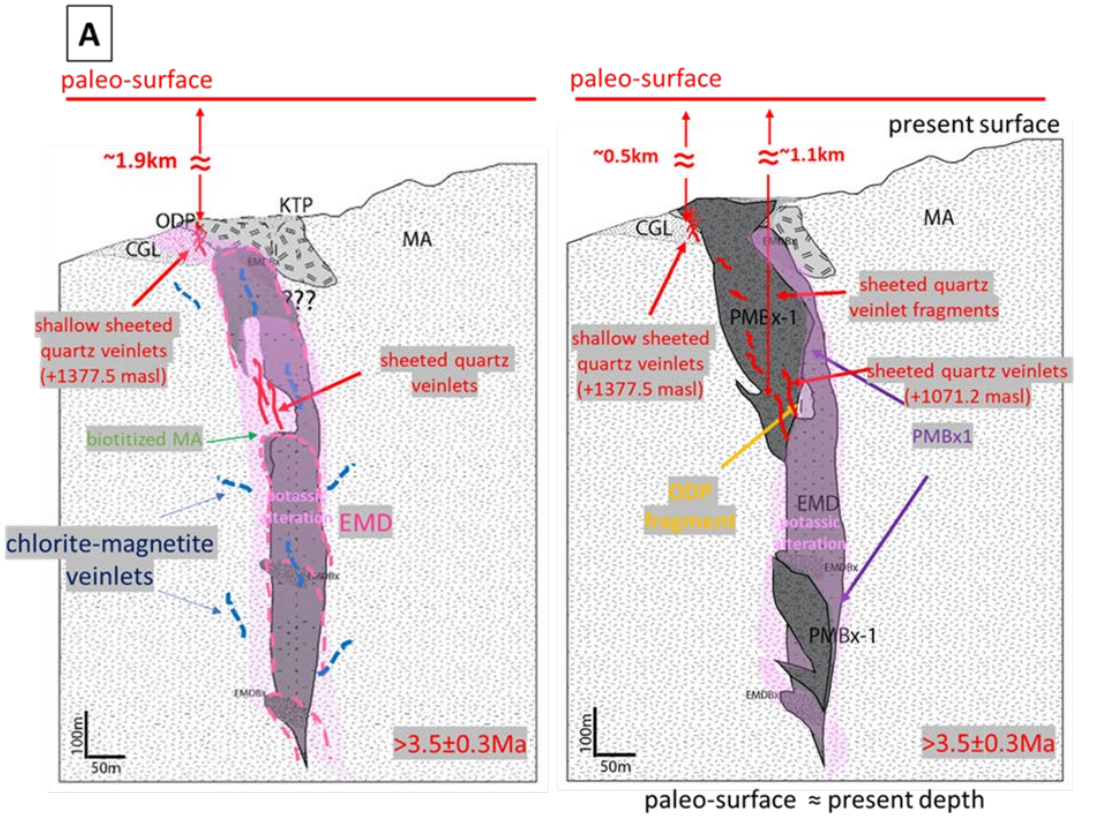

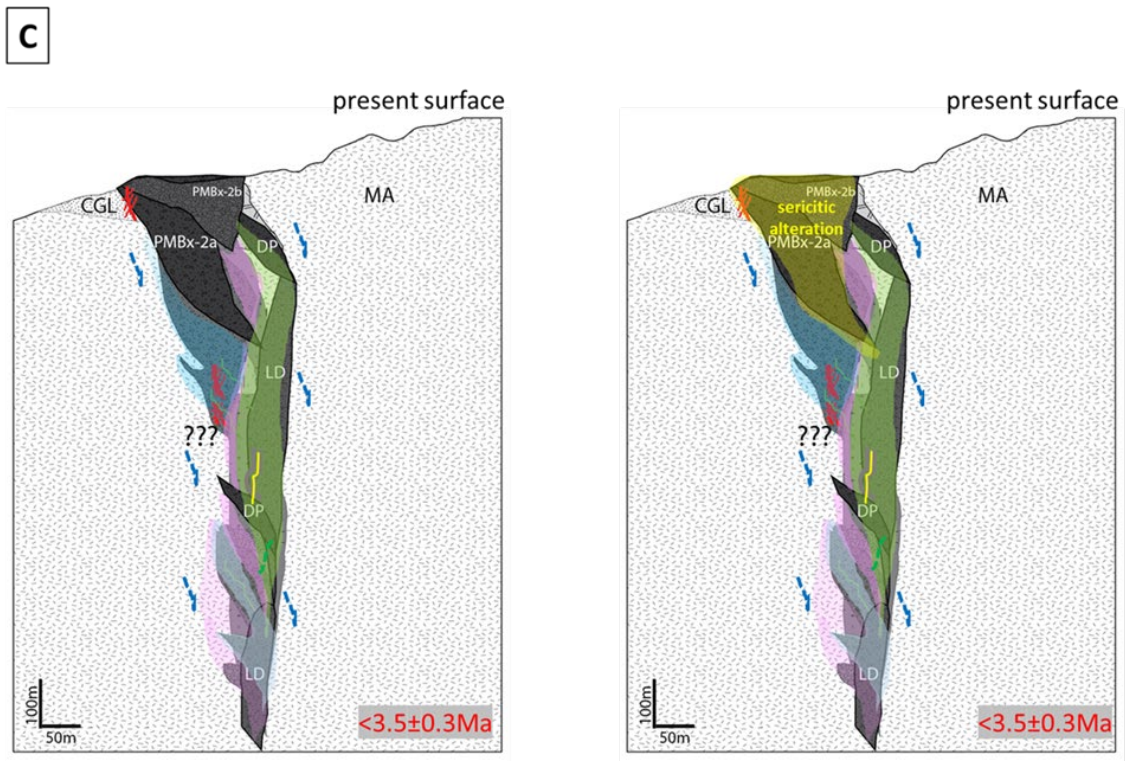

Fig. 27 Evolution of the Southwest prospect. Base image modified from Philex Mining Corporation (Unpublished). a.) Syn-mineralization timeline indicating the early stage of porphyry copper mineralization in the Southwest prospect. The diagram shows the multiple phases of intrusion of the EMD magma and the effect of the potassic alteration to the wall-rocks. The diagram also shows that PMBx-1 destroyed the pre-existing rocks and alteration envelope, along with the deposition of the contemporaneous sheeted quartz veinlets at their estimated depth of formation and distal chlorite-magnetite veinlets; b.) Late-mineralization timeline marked by the intrusion of the LD magma, resulting to the dilution of potassic alteration and mineralization, and consequent overprinting chlorite-magnetite alteration and propylitic alteration in the adjacent rocks; (c) Post – porphyry copper mineralization timeline and late development of the hydrothermal system in the Southwest prospect. Abbreviations mean: MA – Meta-andesite; CGL – Conglomerate; KTP – Keratophyre, ODP – Old Diorite Porphyry; EMD – Early Mineralization Diorite; PMBx-1 – Phreatomagmatic Breccia Facies 1; LD – Late Diorite; DP – Diorite Porphyry; PMBx-2a – Phreatomagmatic Breccia Facies 2a; PMBx-2b – Phreatomagmatic Breccia Facies 2b

7.2 Nature of the hydrothermal system

Remarkable copper and gold grades coincide with the syn- to late-mineralization intrusive rocks and breccias, as well as with the potassic and chlorite-magnetite alteration types and related hydrothermal vein types.

The X_{Mg} of magnesiohornblende phenocrysts, the core and rims, as well as the chlorite alteration products are high (>0.7), indicating high f_{O2} since the early stages of emplacement of the EMD (e.g. Czamanske & Wones, 1973; Kawakatsu and Yamaguchi, 1987; Imai, 2001) even before the development of potassic alteration. The X_{Mg} of chlorite and actinolite vein infill associated with the chalcopyrite-magnetite-chlorite-actinolite±sericite veinlets also are high (0.7), probably indicating formation at high f_{O2}.

Most of the polyphase hypersaline fluid inclusions in the granular quartz veinlets in the EMD and banded quartz veinlets in the LD did not reach liquid-vapor homogenization even at temperatures >720°C. The measured minimum Th(L-V) of fluid inclusions, particularly in the banded quartz veinlets was 687°C, a temperature too high to precipitate copper-iron sulfides, thus the lack of bornite and chalcopyrite in the assemblage. Moreover, the fluid inclusion assemblage on these types of veinlets also lack the two-phase (liquid-vapor) liquid-rich fluid inclusions common in low salinity fluids probably suggesting that meteoric water was not involved (Takenouchi, 1980) at the syn- to late-mineralization stages.

Boiling of the fluids is indicated by the fluid inclusion assemblage, characterized by the trapping of immiscible fluids (i.e. co-existence of the low-density vapor-rich (VR-b fluid inclusions) and hypersaline fluid inclusions (LR-a) and (LR-b), as well as the wide range of liquid-vapor homogenization temperatures measured by the heating experiments

attributing to the variations in the proportions in the vapor bubble on the sheeted quartz veinlets, both at the shallow and deep levels (Fig. 24). There is, however, a significant scarcity of low-density vapor-rich fluid inclusions in the assemblage, that probably indicates that due to the high degree of boiling, a bulk of the low-density vapor-rich fluid inclusions have ascended (Imai & Nagai, 2009). Meanwhile, the abundant VR-a fluid inclusions in sheeted-deep quartz veinlets are interpreted as secondary fluid inclusions (Fig.24). These fluid inclusions are likely a result of healing of cracks in quartz crystals, otherwise known as “necking down”, thus the secondary origin (Roedder, 2002).

Due to boiling, the minimum recorded liquid-vapor homogenization temperature would imply minimum trapping temperature, thus pressure of homogenization and estimated depths can be estimated (Hurai et al., 2015b). Vapor pressures were then estimated based on the intersection of the liquid-vapor homogenization temperature and the liquid+vapor curve at the calculated salinities of 49 and 41 wt% NaCleq for the shallow and deep sheeted quartz veinlets, respectively (Bodnar & Vityk 1994; Driesner & Heinrich, 2007). Based on the measured minimum Th(L-V) of fluid inclusions of 554°C and 436°C for the shallow and deep sheeted quartz veinlets, respectively, the minimum pressures of homogenization are estimated to be ca. 50MPa and 30MPa, respectively (Fig. 28). The calculated depths of formation based on lithostatic load are 1.9km and 1.1km, respectively. This implies decompression, considering that the shallow sheeted quartz veinlets were formed earlier than the deep sheeted quartz. Furthermore, using the sheeted-shallow quartz veinlets as reference, the depth uplifted was estimated to be 0.5km (Fig. 27a).

The ore-forming fluids in the syn-mineralization timeline precipitated chalcopyrite and bornite as interstitial sulfides in between quartz grains in quartz veinlets.

The presence of LR-b fluid inclusions implies the trapping of a multi-cation solution due to the presence of daughter crystals such as sylvite (KCl), and other unidentified Ca-, Mg-, $FeCl_2$. These fluids probably reacted with the crystallized mineralized and wallrocks developing the widespread potassic alteration. The fluids must have cooled at temperatures below 532°C, the temperature the assemblage of chalcopyrite and bornite (bnss) is stable (Barton, 1973; Imai, 2001).

Toward the late-mineralization stage, involvement of external waters, possibly meteoric water, to form the later quartz veinlets, including the crystalline and vuggy quartz veinlets, as suggested by the presence of two-phase liquid-rich fluid inclusions as secondary inclusions. Nevertheless, these types of fluid inclusions are scarce, thus the involvement of external waters are probably minor.

In addition, crystalline quartz veinlets contain fluid inclusions that homogenized by the dissolution of halite, rather than by L-V homogenization (Td>Th; Fig. 29). Such occurrence also indicates that halite crystals were already present during the entrapment of a highly saline fluid (Shepherd et al., 1985; Suerte, 2007; Imai & Nagai, 2009). Heating experiments will result to over-estimation of the calculated salinity and estimated pressure of homogenization of the fluid inclusions (Shepherd et al., 1985; Suerte, 2007).

The fluid inclusions in the vuggy quartz veinlets homogenized at 317°C. Similarly, the chlorite geothermometer applied on chlorite stringers contemporaneous with the propylitic alteration estimated a temperature range of 320 to 340°C, indicating the temperature of the system during the late-mineralization stage. Some of the earlier-formed quartz veinlets were re-opened, while some show vuggy textures, indicating continued injection of magmatic fluids through the incipient fractures, joints and veinlets.

Furthermore, the vuggy texture implies dissolution and probably remobilization of earlier formed minerals, probably including anhydrite due to its solubility in more saline fluids in the higher temperature (Blount & Dickson, 1969; Imai, 2001).

The estimated temperature of the chlorite associated with the chalcopyrite-magnetite-chlorite-actinolite±sericite veinlets is between 290 to 300°C, significantly lower than the chlorites formed by propylitic alteration. The lower temperature may also imply late-stage mineralization. Moreover, a significant difference in the X_{Mg} values was illustrated among the chlorites from various alteration types (Fig. 19b). The X_{Mg} of chlorite associated chalcopyrite-magnetite-chlorite-actinolite±sericite veinlets are higher than the chlorite stringers in the propylitic alteration. This probably indicates the co-genetic precipitation with chalcopyrite and magnetite, as Fe would have been partitioned in these minerals.

Clay sericitization and subordinate chloritization overprinted the shallow levels of the prospect, implying hydrogen metasomatism by hydrothermal fluids with a possible significant meteoric water contribution (Takenouchi, 1980).

The $\delta^{34}S$ values of the sulfides from the various paragenetic stages range mostly lie within the narrow range of +2.8‰ and +4.6‰ and remained constant throughout the vertical extent of the prospect implying a similar source of sulfur of the sulfides associated

with the different vein types, which is from hydrothermal ore deposits associated with igneous rocks (Sasaki & Ishihara, 1979; Imai, 1993, 2001, 2002)

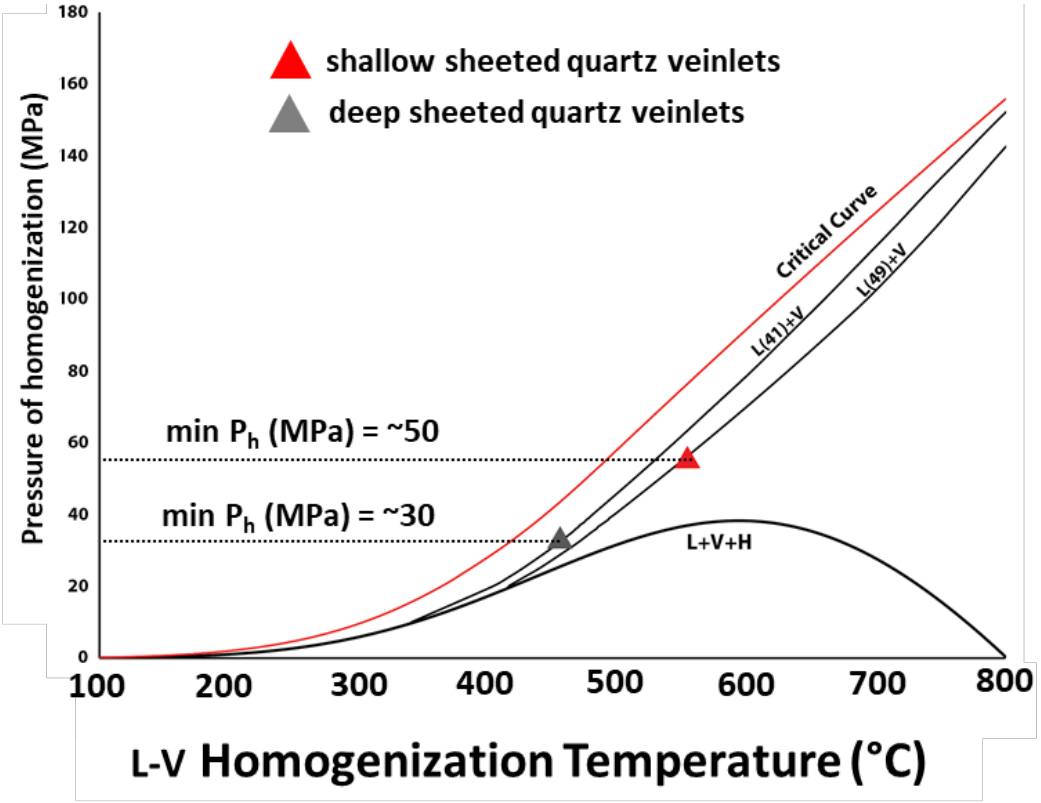

Fig. 28 L-V homogenization temperature (Th) vs pressure of homogenization (Ph) Diagram showing plotting the L-V Homogenization Temperature (Th) along the L+V curve to estimate the pressure of homogenization. Gray triangle and red triangle correspond to the minimum Th of the deep sheeted quartz veinlets and shallow sheeted quartz veinlets, respectively. The liquid-vapor-halite three phase, L+V and critical curve were computed based on the equations provided by Driesner and Heinrich (2007). The halite liquidus line was computed based on the procedure outlined by Cline and Bodnar (1994) and Bodnar and Vityk (2004)

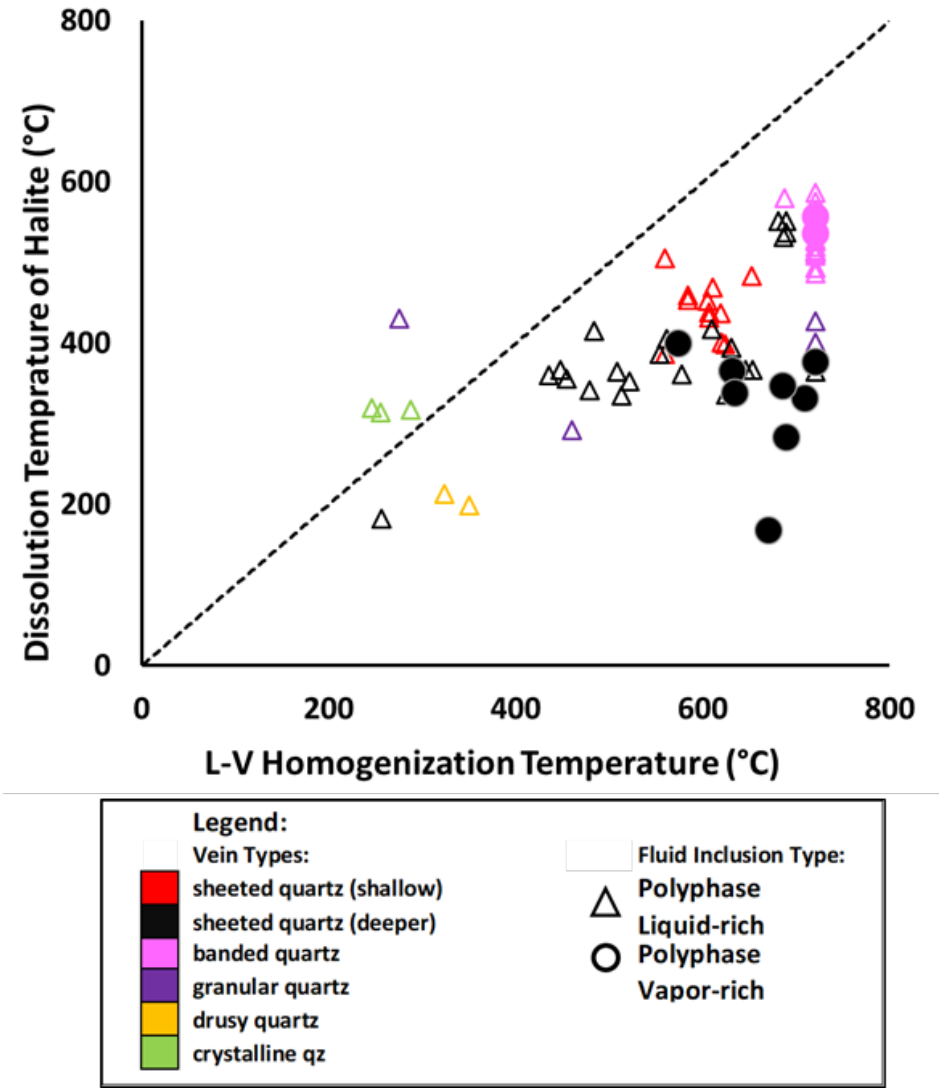

Fig. 29 Dissolution temperature of halite (Td) vs L-V Homogenization Temperature (Th) of the polyphase hypersaline fluid inclusions in the Southwest prospect. The diagonal dashed line indicates Td=Th. Polyphase hypersaline fluid inclusions that plot above the line are fluid inclusions that homogenize by halite dissolution, while those that plot below the line are fluid inclusions that homogenize by liquid-vapor homogenization. Adopted from Shepherd et al. (1985) and Suerte et al. (2007).

7.3 Overprinting porphyry copper type veinlets

The Vein Off-setting Matrix and paragenetic diagram summarized that the assemblages of veinlets associated with each of the intrusion and breccia facies were deposited in two manners, (Fig. 12 & 25). Two relationships can be observed, normal and reverse off-setting relationships. Reverse off-setting relationships is common only within the EMD. In this scenario, the earlier formed assemblages of veins consisting of the high temperature quartz veinlets and lower temperature distal chlorite veinlets were continuously being overprinted by a later assemblage of quartz and chlorite veinlets (Fig. 27a). This led to the observed offsets of lower temperature chlorite veinlets by the higher temperature quartz veinlets, and indicates a prolonged, repetitive emplacement of EMD pulses. In contrast, cyclic occurrences of normal off-setting relationships were observed in the LD and the later breccia facies, PMBx-1 and PMBx-2, indicating a probable short-lived vein formation in each intrusive and breccia event.

Basing on these parameters, porphyry copper type veinlets, including the sheeted quartz veinlets and chalcopyrite-rich chlorite-magnetite veinlets must have been sourced from the adjacent intrusive rocks, EMD and LD. Nonetheless, limited exposures and severe overprinting masked the continuities of these veinlets toward the intrusive rocks. It is also possible that some of these veinlets are sourced from an intrusion sitting at a deeper level due to the cyclic deposition of veinlets from the intrusions. Furthermore, the hole SWD-17-07 bottoming at the LD may imply the presence of another intrusion that is yet to be identified.

7.4 Brecciation in the Southwest Prospect

At least two genetic breccia types Southwest prospect are found: hydrothermal and phreatomagmatic breccias. Hydrothermal brecciation, which is represented by the breccia facies such as EMDBx and DPBx that involved the fracture development induced by the release of pressure that was built-up by the forceful intrusion of an underlying magma and succeeded by cementing of hydrothermal minerals (Sillitoe, 2010). On the other hand, phreatomagmatic brecciation, which are represented by the various PMBx facies involved the direct interaction of a hydrothermal fluid with the magma (Lawless & White, 1990).

Modelling on the wallrock failure during the emplacement of a hydrous silicic magma (e.g. Burnham & Ohmoto, 1980; Burnham, 1985) indicates that fracture intensity and explosivity are a function of depth of emplacement or confining pressure, and mechanical energy released by the hydrous magma (i.e. expansion or internal pressure of the magma body). The mechanical energy exerted by the magma body to the confining wallrock is a consequence of second boiling and decompression processes in porphyry copper deposits (Burnham, 1985). The development of the explosive breccia facies in the Southwest prospect is a result of the decompression process, as implied by the difference in the Al content between the hornblende cores and rims in the EMD and LD (Imai, 2001). Amphibole geobarometer applied on the EMD and least altered quartz diorite ((Hammarstrom & Zen, 1986; Imai, 2001) implies shallow crustal level of emplacement at pressures <400MPa, both at highly oxidizing conditions and decompressed to pressures <100MPa based on the presence of tremolitic rims on hornblende phenocrysts (Fig. 17). The pressure and depth estimates by fluid inclusion studies shows consistent results indicating shallow level emplacement of the intrusive rocks.

On the other hand, phreatomagmatic breccias were formed from the complex interaction of magma involved in a volcanic activity and external source of water, most likely groundwater as reasoned by Lorenz (1985). This is also consistent with descriptions of Sillitoe (2010) on the diatreme breccias as late stage additions to porphyry copper deposits at the time when magmas are in proximity with external source of water.

7.5 Implications to the mineralization in the Southern Baguio District

A number of clusters of porphyry copper, epithermal gold and skarn deposits have been discovered in the Baguio District. At the central southern part of the district, the Sto. Tomas II deposit, along with Clifton prospect and Bumolo deposit defines a cluster of intrusions endowing porphyry copper mineralization (Waters et al., 2010). Several radiometric ages are available on these intrusions. Waters et al. (2010) delineated a 2.1 to 1.4 Ma for this cluster, particularly corroborated by $^{40}Ar/^{39}Ar$ dating on hydrothermal biotite of the intra-mineralization rocks (1.48±0.05 Ma and 1.47±0.05 Ma) and K-Ar dating the altered "ore-generating andesite porphyry" (Imai, 2001) corresponding to the "dark diorite" (Baluda & Galapon, 2005) or main stage intrusion in the Sto. Tomas II deposit. Similarly, available age data on Clifton and Bumolo are well within this range (Fig. 19) (Bellon & Yumul, 2000; Imai, 2001; Waters et al., 2011). Findings in the Southwest prospect provide information in the early development of the magmatic-hydrothermal system in the Sto. Tomas II vicinity.

Due to the overlapping magmatic, phreatomagmatic and hydrothermal events in the Southwest prospect and proximity of the intrusions and breccias, the K-Ar age of the hydrothermal biotite was most likely thermally reset, thus the development of the potassic

alteration could have been older. K-Ar age on the LD constrains the high-grade mineralization in the Southwest prospect related to the potassic and chlorite-magnetite alteration types and the initial phreatomagmatic brecciation to be not any younger than 3.5 ± 0.3 Ma, contrary to the idea that it could have been an intra-mineralization diatreme as indicated by the initial exploration results (Sillitoe, 2011; Philex Mining Corporation, 2017). While the ages of the late-stage breccia facies, are not constrained, multi-stage brecciation events are indicated by the varieties of clasts such as later intrusive rocks such as the DP.

Overprinting relationships of the intrusions and breccia facies and results of the K-Ar ages suggest short-lived cycles of intrusions and breccia events in the Southwest prospect, particularly beginning the syn-mineralization timeline after the emplacement of EMD. The cycles of intrusions and breccia events in the Southwest prospect is significantly shorter than the oldest intrusive rocks in the Sto. Tomas II have reported whole rock K-Ar ages on the “dark diorite” are 5.9±1.6 Ma (least altered), 3.8±1.1 Ma (altered) by Togashi et al. (1990) (Fig. 30). However, new K-Ar and Ar-Ar age data (Imai, 2001; Waters et al., 2011) indicate that the main hydrothermal mineralization event in the Sto. Tomas II deposit is also characterized by short-lived cycles of multiple intrusions, along with the Clifton and Bumolo deposits (Fig. 30). Such characteristic has been observed in the Grasberg deposit, Ertsberg District (Pollard & Taylor, 2005).

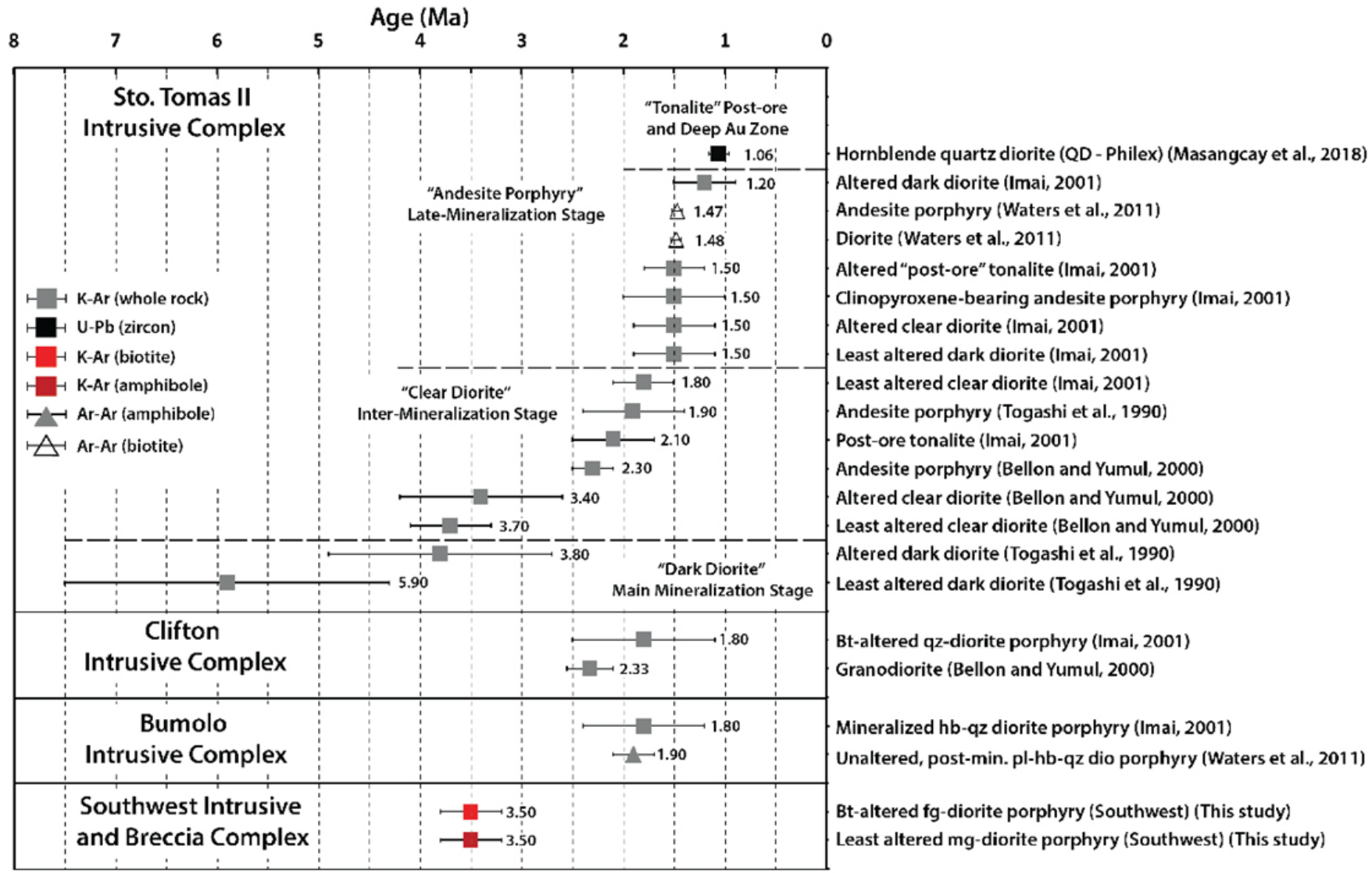

Fig. 30 Geochronology of the Sto. Tomas II – Bumolo – Clifton cluster. K-Ar ages of the Southwest potassic alteration and late-intermineralization diorite (LD) were plotted as bright red box (potassic alteration) and dark red box (LD). Data on the Sto. Tomas II, Clifton and Bumolo Intrusive complexes were compiled from Togashi et al. (1990), Bellon & Yumul (2000), Imai (2001), Waters et al. (2011), and Masangcay et al. (2018). Abbreviations mean: bt – biotite; hb – hornblende; pl- plagioclase ; qz – quartz ; por – porphyry ; QD – Quartz Diorite; LD – Late Diorite; fg-diorite porphyry – fine-grained diorite porphyry; mg-diorite porphyry – medium-grained diorite porphyry; qtz dio porphyry – quartz diorite porphyry; post-min. – post-mineralization.

The $\delta^{34}S$ of sulfides hosted throughout the paragenetic sequence of the Southwest prospect overlaps with the $\delta^{34}S$ of sulfides of the other porphyry copper deposits distributed particularly in the southern half of the Baguio District and some epithermal gold deposits (Fig. 31). The $\delta^{34}S$ of chalcopyrite from the syn-mineralization to late-mineralization stages, in the Southwest prospect fall within the range of the $\delta^{34}S$ of sulfides in the Sto. Tomas II deposit, which ranges from +2.2‰ to +5.7‰ (Imai, 2001), and the Clifton prospect, also ranges from +1.0‰ and +5.2‰ (Cirineo, 2017). Furthermore, the $\delta^{34}S$ of sulfides of gold-rich mineralization closely associated with pyrite, sphalerite and galena in the "V3" veins below 773ML of the Sto. Tomas II deposit (Masangcay et al., 2018) fall in between +4.9‰ and +7.2‰ (Yoneda, 2015; Cirineo, 2017), a range that overlaps with that of the pyrites in the late hydrothermal stage in the Southwest prospect. The overlapping of $\delta^{34}S$ of sulfides indicates the possibility of same origin of sulfur for the abovementioned deposits, and thus probably defines a cluster of porphyry copper-related deposits developed from the same source.

Nevertheless, it is not possible to determine the $\Sigma\delta^{34}S$ of the magma and mineralizing fluids in the Southwest prospect due to the absence of coexisting sulfide-sulfate mineral pair in the cogenetic igneous rocks, and lack of sulfates throughout the paragenetic sequence due to the possibility of late hydrothermal leaching that occurred during the overprinting of hydrothermal events. The source of sulfur in the wester Luzon arc, however, was discussed by several authors (e.g., Hattori, 1993; Imai, 1993, 1996, 2000, 2001, 2002; Cooke et al., 2011). $\Sigma\delta^{34}S$ values of nearby deposits within the Baguio District such as the Sto. Tomas II and Kelly deposits probably lie in between +4.4‰ and +13.7‰, and +0.8‰ and +15‰, respectively. Cooke et al. (2011) estimated a value of +5‰ for the $\Sigma\delta^{34}S$ of the magma and mineralizing fluids in the Baguio District. The magma and mineralizing fluids in the Lepanto-FSE located further north, in the Mankayan District have a $\Sigma\delta^{34}S$ of ca. +6‰ (Imai, 2000b), while hydrochloric leached sulfur from the Mt. Pinatubo dacitic pumice $\Sigma\delta^{34}S$ ranging from +7.8‰ and +9‰ (Imai, 1993, 1996, 2001, 2002). These data indicate a source of sulfur that is enriched in the ^{34}S for the hydrous magmas that gave rise to the western Luzon arc (Imai, 2001, 2002), a common feature seen in hydrous magmas emplaced in arc setting (Imai, 2001) and granitiods and associated ore deposits emplaced in continental margins (Sasaki & Ishihara, 1979; Ishihara et al., 2000; Imai & Anan, 2000; Imai, 2001; 2002). This feature is interpreted as the result of the sulfur being transported by the aqueous phase that originated from the subducting slab of the oceanic lithosphere. The sulfur was derived from the sulfides and sulfates that were formed in the oceanic seafloor through the sea water advection and subsequent hydrothermal alteration (Sasaki & Ishihara, 1979; Imai, 1993, 2001, 2002).

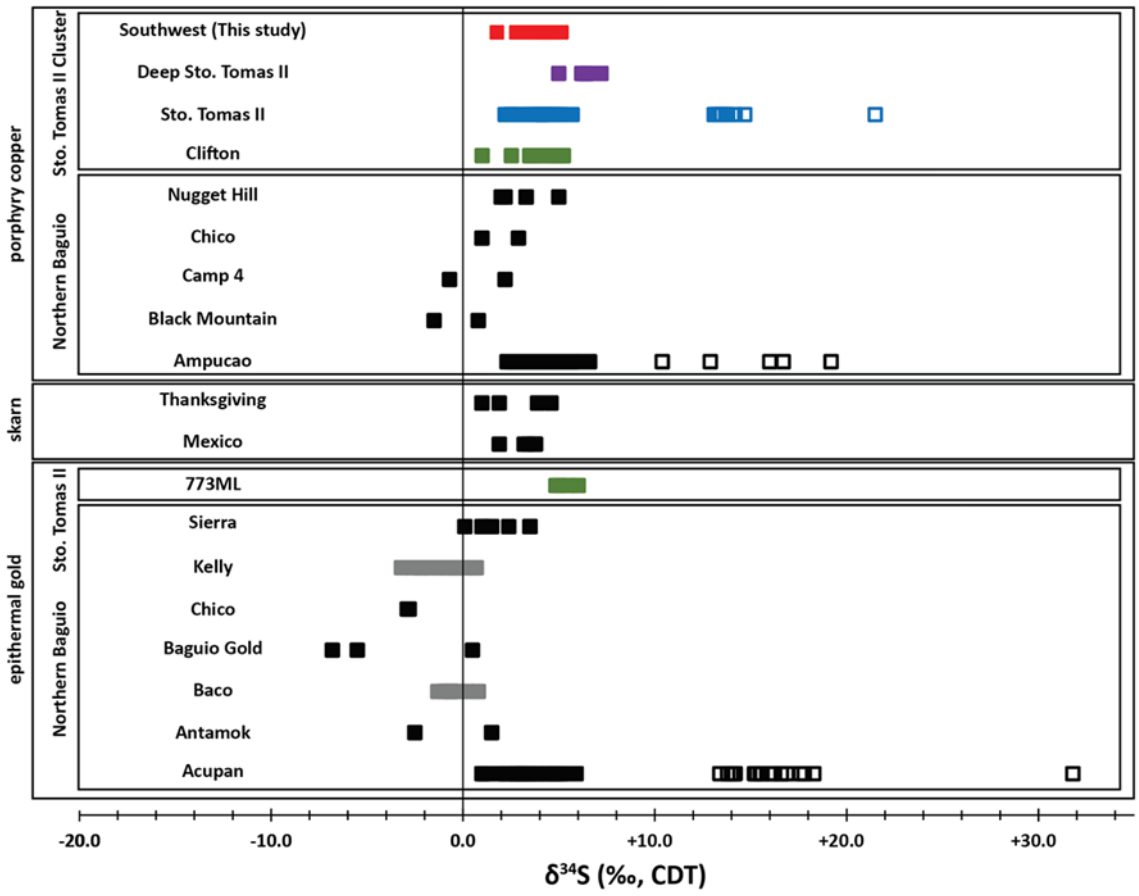

Fig. 31 Comparison of sulfur isotope ranges (‰, CDT) for the sulfides and sulfates from the porphyry and epithermal deposits in the Baguio District. Data from the Southwest prospect (Table 7) are sulfides only, marked in red circles. Data from the Sto. Tomas II deposit, sulfides in blue circles and sulfates in blue diamonds, are taken from Imai (2001); sulfides in green circles from the Clifton prospect (Cirineo, 2017); sulfides in violet circles from the Deep Gold Zone of Sto. Tomas II (Yoneda, 2015). Data from the other deposits in the Baguio district from Cooke et al. (2011) in black circles and black diamonds and from Deyell and Cooke (2003). Note: CDT – Canyon Diablo Troilite.

8 Conclusions

The development of the magmatic-hydrothermal system responsible for the formation of porphyry copper-type mineralization in the Southwest prospect was a consequence of the succession of intrusions, breccias and hydrothermal alteration and vein formation. High grade copper and gold mineralization were intimately associated with (1) chalcopyrite-bornite assemblage in the potassic alteration in the EMD (Early Mineralization Diorite) and contemporaneous veinlets and (2) chalcopyrite-rich mineralization associated with the chalcopyrite-magnetite-chlorite-actinolite±sericite veinlets contemporaneous with the chlorite-magnetite alteration. These were formed during the syn-mineralization and late-mineralization defined by the development of potassic alteration by the emplacement of the EMD and chlorite-magnetite alteration by the crystallization of the LD (Late Diorite). K-Ar ages of the potassic alteration and the LD intrusion are both 3.5±0.3 Ma, suggesting a short gap between the two events or thermal reset by overprinting.

The ore-formation in the Southwest prospect involved boiling of magmatic fluids. Based on the fluid inclusion study on the sheeted quartz veinlets, these fluids were trapped in the subcritical immiscible region at pressures of 50 and 30MPa and temperatures of 554 and 436°C, forming the potassic alteration at depths 1.9km and 1.1km. The chalcopyrite-rich mineralization associated with the chlorite-magnetite alteration occurred at a much lower temperature (ca. 290°C) than the potassic alteration.

The Southwest prospect further defines the cluster of intrusions endowed with porphyry copper mineralization in the Sto. Tomas II vicinity. The Southwest prospect likely represents a pre-mineralization breccia during the early development of the magmatic-hydrothermal system in the Sto. Tomas II and nearby prospects. The range of

$\delta^{34}S$ of sulfide minerals from +1.8‰ to +5.1‰ in the Southwest prospect closely overlaps with those of the Sto. Tomas II, Clifton and Bumolo porphyry copper deposits and epithermal vein prospects within the vicinity, indicating a homogeneous source of sulfur.

References

Ahmad, S. N. and Rose, A. W. (1980) Fluid Inclusions in Porphyry and Skarn Ore at Santa Rita, New Mexico. Econ. Geol., 75, 229-250.

Aoki, M. Comsti, E. C., Lazo, F. B. and Matsuhisa, Y. (1993) Advanced argillic alteration and geochemistry of alunite in an evolving hydrothermal system at Baguio, northern Luzon, Philippines. Resource Geol., 43, 155-164.

Ault, W. Y. and Jensen, M. L. (1963) Summary of sulfur isotope standards. *in* : Jensen, M. L. (ed.), Biogeochemistry of Sulfur Isotopes: Natl. Sci. Found., Symposium Proc., Yale University, 16-29.

Aurelio, M. A. (2000) Tectonics of the Philippines revisited. Jour. Geol. Soc. Philippines, 55, 119-184.

Aurelio, M. A. (2006) Preliminary Structural Geological Analysis of Mineral Deposits/Prospects between Padcal & Ansagan, Tuba, Benguet. Internal Report, Philex Mining Corporation, Pasig City, Philippines, 71p.

Aurelio, M. A. (2007a) Fieldwork Report: Bumolo Prospect. Internal Report, Philex Mining Corporation, Pasig City, Philippines, 8p.

Aurelio, M. A. (2007b) Fieldwork Report: Clifton Prospect. Internal Report, Philex Mining Corporation, Pasig City, Philippines, 6p.

Aurelio, M. A. (2007c) Fieldwork Report 1: Tapaya Prospect. Internal Report, Philex Mining Corporation, Pasig City, Philippines, 5p.

Aurelio, M. A., Alejan, L., Baluda, R. P., Cuyos, F. Q., Francisco, G. G., Galapon, J. B. and Sucilan, J. (2009) Timing of faulting events along the Albian and Sta. Fe Faults in the Sto. Tomas II orebody, Tuba, Benguet, Philippines: new insights from Leapfrog TM modelling and implications to fault conditions favorable for

ore deposition. Geological Society of the Philippines: GEOCON. 3-5, December, 2008, Makati, Philippines.

Aurelio, M. A. and Peña, R. E. (2004) Tectonics. *in* : Aurelio, M. A. and Peña, R. E. (eds.), Geology and Mineral Resources of the Philippines, 1, 18-47.

Balce, G. R. (1979) Geology and ore genesis of the porphyry copper deposits in Baguio District, Luzon Island, Philippines. Jour. Geol. Soc. Philippines, 32, 1-43.

Balce, G. R., Encina, R. Y., Momongan, A. and Lara, E. (1980) Geology of the Baguio district and its implication on the tectonic development of the Luzon Central Cordillera. Geology and Paleontology of Southeast Asia, 21, 265-287.

Baluda, R. P. and Galapon, J. B. (2005) Geology of Sto. Tomas II porphyry copper deposit. Jour. Geol. Soc. Philippines, 49, 1-11.

Barton, P. B., Jr. (1973) Solid solutions in system Cu-Fe-S. Part I. The Cu-S and Cu-Fe-S join. Econ. Geol., 68, 455-465.

Beane, R. E. (1974). Biotite stability in the porphyry copper environment. Econ. Geol., 69, 241-256.

Bellon, H. and Yumul, G. P., Jr. (2000) Mio-Pliocene magmatism in the Baguio Mining District (Luzon, Philippines): Age clues to its geodynamic setting. Comptes Rendus de l'Academie des Sciences, Sciences de la Terre et Des Planetes, 331, 295-302.

Blount, C. W. and Dickson, F. W. (1969) Solubility of anyhydrite (CaSO4) in NaCl-H_2O from 100 to 450°C and 1 to 1000 bars. Geochim. Cosmochim. Acta, 33, 227-245.

Bodnar, R. J. and Vityk, M. O. (1994) Interpretation of microthermometric data for H_2O-NaCl fluid inclusions. *in* : de Vivo, B. and Frezzotti, M. L. (eds.), Fluid

Inclusions in Minerals, Methods and Applications. Virginia Tech., Blacksburg, 117-130.

Bureau of Mines and Geosciences (2004) Mineral Resource Information Series No. 5: Copper. Mines and Geosciences Bureau, Department of Environment and Natural Resources, Quezon City, Philippines, 21p.

Burnham, C. W. (1979) Magmas and hydrothermal fluids. *in* : Barnes, H. L. (ed.) Geochemistry of Hydrothermal Ore Deposits. 2nd edn. John Wiley, New York, 71-136.

Burnham, C. W. (1985) Energy release in subvolcanic environments: implications for breccia formation. Econ. Geol., 80, 1515-1522.

Burnham, C. W. and Ohmoto, H. (1980) Late-stage processes of felsic magmatism. *in* : Ishihara, S. and Takenouchi, S. (eds.), Granitic Magmatism and Related Mineralization. Mining Geol. Spec. Issue, 8, 1-11.

Cathelineau, M. (1988) Cation site occupancy in chlorites and illites as a function of temperature. Clay Miner., 23, 471-485.

Cathelineau, M. and Nieva, D. (1985) A chlorite solid solution geothermometer. The Los Azufres (Mexico) geothermal system. Contrib. Mineral. Petrol., 91, 235-244.

Chivas, A. R. (1981) Geochemical evidence for magmatic fluids in porphyry copper mineralization. Part I. Mafic silicates from the Koloula igneous complex. Contrib. Mineral. Petrol., 78, 389-403.

Cirineo, A. V. L. (2017) Characteristics and Ore Genesis of the Clifton Porphyry Copper-gold Prospect, Northern Luzon, Philippines. Unpublished Master Thesis, Akita University, Akita, Japan.170p.

Clark, A. L. (1994) The Philippines Mineral Sector to 2010: Policy and Recommendations. Report to the Asian Development Bank on T.A. No 1984-PHI, Honolulu, Hawaii.

Cline, J. S. and Bodnar, R. J. (1994) Direct evolution of brine from a crystallizing silicic melt at the Questa, New Mexico, Molybdenum Deposit. Econ. Geol., 89, 1780-1802.

Coderis, G. J. R. (2011). Results of the Southwest Breccia Fieldwork. Internal Report. Philex Mining Corporation, Pasig City, Philippines, 5p.

Cooke, D. R. and Berry, R. F. (1996) Porphyry-epithermal relationships in the Baguio district, Philippines – telescoping of low sulfidation mineralization by transpressional uplift and erosion. Geol. Soc. Amer. Program with Abstracts, 28, A155.

Cooke, D. R., Deyell, C. L., Waters, P. J., Gonzales, R. I. and Zaw, K. (2011) Evidence for magmatic-hydrothermal fluids and ore-forming processes in Epithermal and Porphyry deposits of the Baguio district, Philippines. Econ. Geol., 106, 1399-1424.

Czamanske, C. G. and Wones, D. R. (1973) Oxidation during magmatic differentiation, Finnmarke Complex, Oslo area, Norway: Part II, The mafic silicates. Jour. Petrol., 14, 349-380.

De Caritat, P., Hutcheon, I. and Walse, J. L. (1993) Chlorite geothermometer: A review. Clay Miner., 41, 219-239.

Deyell, C. L. and Cooke, D. R. (2003) Mineralogical and isotopic evidence for the genesis of the Kelly gold-silver deposit, Baguio district, Philippines: Diverse mineral assemblages in a hybrid epithermal system. *in* : Eliopoulos, D., et al. (eds.),

Mineral Exploration and Sustainable Development – Proceedings of the Seventh Biennial SGA Meetings: Millpress, Rotterdam, 1, 469-472.

Driesner, T. and Heinrich, C. A. (2007) The system H_2O-NaCl. Part I: correlation formulae for phase relations in temperature-pressure-composition space from 0 to 1000°C, 0 to 5000 bar, and 0 to 1 XNaCl. Geochim. Cosmochim. Acta, 71, 4880-4901.

Fernandez, H. R. and Damasco, F. V. (1979) Gold deposition in the Baguio gold district and its relationship to regional geology. Econ. Geol., 74, 1852—1868.

Foster, M. D. (1960). Interpretation of the composition of trioctahedral micas. US Geol. Survey. Prof. Pap. 354-B, 1-146.

Gill, R. (2010) Andesite, dacite and rhyolite. *in* : Gill, R. (ed.), Igneous Rocks and Processes: A Practical Guide. John Wiley & Sons. Ltd., London, 161-208.

Hammarstrom, J. M. and Zen, E. (1986) Aluminum in hornblende: An empirical igneous geobarometer. Amer. Mineral., 71, 1297-1313.

Hattori, K. (1993) High sulfur magma, a product of fluid discharge from underlying mafic magma: Evidence from Mount Pinatubo, Philippines. Geology, 21, 1083-1086.

Heys, M. H. (1954) A new review of the chlorites. Mineral. Mag., 30, 277-292.

Hillier, S. and Velde, B. (1991) Octahedral occupancy and the chemical composition of diagenetic (low-temperature) chlorites. Clay Miner., 26, 149-168.

Hollings, P., Wolfe, R., Cooke, D. R. and Waters, P. J. (2011) Geochemistry of Tertiary igneous rocks of northern Luzon, Philippines: Evidence for a back-arc setting for alkalic porphyry copper-gold deposits and a case for slab roll-back? Econ. Geol., 106, 1257-1277.

Hurai, V., Huraiova, M., Slobodnik, M. and Thomas, R. (2015a) Fluid and melt inclusion microthermometry. *in* : Hurai, V., M., Slobodnik, M. and Thomas, R. (eds.), Geofluids, Developments in Microthermometry, Spectroscopy, Thermodynamics, and Stable Isotopes. Elsevier, Massachusetts, USA, 59-170.

Hurai, V., Huraiova, M., Slobodnik, M. and Thomas, R. (2015b) Interpretation of Microthermometric Data. *in* : Hurai, V., M., Slobodnik, M. and Thomas, R. (eds.), Geofluids, Developments in Microthermometry, Spectroscopy, Thermodynamics, and Stable Isotopes. Elsevier, Massachusetts, USA, 117-170.

Imai, A. (2000a) Genesis of the Mamut porphyry copper deposit, Sabah, East Malaysia, Resource Geol. 49, 151-168.

Imai, A. (2000b) Mineral paragenesis, fluid inclusions and sulfur isotope systematics of the Lepanto Far Southeast porphyry Cu-Au deposit, Mankayan, Philippines. Resource Geol., 50, 151-168.

Imai, A. (2001) Generation and evolution of ore fluids for porphyry Cu-Au mineralization of the Santo Tomas II (Philex) deposit, Philippines. Resource Geol., 51, 71-96.

Imai, A. (2002) Metallogenesis of porphyry cu deposits of the western Luzon Arc, Philippines: K-Ar ages, SO3 contents of microphenocrystic apatite and significance of intrusive rocks. Resource Geol., 52, 147-161.

Imai, A. (2005) Evolution of hydrothermal system at the Dizon porphyry Cu-Au deposit, Zambales, Philippines. Resource Geol., 55, 73-90.

Imai, A. and Anan, S. (2000) Sulfur isotope study and re-examination of ore mineral assemblage of the Hol Koland the Tul Mi Chung skarn-type copper-gold deposits of the Suan mining district, Korean Peninsula. Resource Geol., 50, 213-228.

Imai, A. and Nagai, Y. (2009) Fluid inclusion study and Opaque mineral assemblage at the deep and shallow part of the Batu Hijau porphyry copper-gold deposit, Sumbawa, Indonesia. Resource Geol., 59, 231-243.

Ishihara, S., Jin, M. S. and Sasaki, A. (2000) Source diversity of ore sulfur from Mesozoic-Cenozoic mineral deposits in the Korean Peninsula region. Resource Geol., 50, 203-212.

Jahren, J. S. and Aagaard, P. (1989) Compositional variations in diagenetic chlorites and illites, and relationships with formation-water chemistry. Clay Miner. 24, 157-170.

Jowett, E. C. (1991) Fitting iron and magnesium into the hydrothermal chlorite geothermometer. GAC/MAC/SEG Joint Annual Meeting. Program with Abstracts, 27-29 May, 1991, Toronto, 16, A62.

Kawakatsu, K, and Yamaguchi, Y. (1987) Successive zoning of amphiboles during progressive oxidation in the Daito-Yokota granitic complex, San'in belt, southwest Japan. Geochim. Cosmochim. Acta, 51, 535-540.

Kranidoitis, I. and MacLean, W. H. (1987) Systematics of chlorite alteration at the Phelps Dodge massive sulfide deposit, Matagami, Quebec. Econ. Geol., 82, 1898-1911.

Lawless, J. V. and White, P. J. (1990) Ore-related breccias: a revised genetic classification with particular reference to epithermal deposits. 12th New Zealand Geothermal Workshop, Auckland, New Zealand, 197-201.

Leake, B. E., Woolley, A. R., Arps, C. E. S., Birch, W. D., Gilbert, M. C., Grice, J. D., Hawthorne, F. C., Kato, A., Kisch, H. J., Krivovichev, V. G., Linthout, K., Laird, J., Mandarino, J. A., Maresch, W. V., Nickel, E. H., Rock, N. M. S., Schumacher, J. C., Smith, D. C., Stephenson, N. C. N., Ungaretti, L. Whittaker, E. J. W. and

Youzhi, G. (1997) Nomenclature of amphiboles: report of the subcommittee on amphiboles of the International Mineralogical Association, Commission on New Minerals and Mineral Names. Can. Mineral., 35, 219-246.

Lorenz, V. (1985) Maars and diatremes of phreatomagmatic origin, a review. Transactions Geol. Soc. South Africa, 88, 459-470.

Lorenz, V. (1986) On the growth of maars and diatremes and its relevance to the formation of tuff rings. Bull. Volcanol., 48, 265-274.

Malihan, T. D. (1982) Geology of the Dizon porphyry copper-gold orebody. in Proceedings of Seminar on Developing New Open Pit Mines in the Philippines. First University of the Philippines Geology Lectures, 1982, 27–49.

Mason, D. R. (1978) Compositional variation in ferromagnesian minerals from porphyry copper generating and barren intrusions of the Western Highlands, Papua New Guinea. Econ. Geol., 73, 878-890.

McDowell, S. D. and Elders, W. A. (1980) Authigenic layer silicate minerals in borehole Elmore 1, Salton Sea geothermal field, California, USA, Contrib. Mineral. Petrol., 74, 293-310.

Masangcay, B. S. M. Luis, R. R. C., Irorita, K. I. N., Cellona, G. D. Maglambayan, V. B. and Baluda, R. P. (2018) Mineralization controls of the gold-rich zone below Santo Tomas II porphyry copper-gold deposit, Tuba, Benguet, Philippines. Jour. Geol. Soc. Philippines, 74, 1-13.

Mitani, A. (2013) Characteristics and Age of Copper Mineralization at Tapaya Prospect, Northern Luzon, Philippines. Unpublished Master Thesis, Kyushu University, Fukuoka, Japan, 51p.

Mitchell, A. H. G. and Leach, T. M. (1991) Epithermal Gold in the Philippines: Island Arc Metallogenesis, Geothermal Systems and Geology. Academic Press, London, 457p.

Nash, J. (1976) Fluid-Inclusion Petrology - Data from Porphyry Copper Deposits and Application to Exploration. *in* : Nash, J. (ed.), Geology and Resources of Copper Deposits, United States Government Printing Office, Washington, D1-D16.

Obial, R. and Cinco, J. C., Jr. (2013) Technical Report: Exploration results and mineral resources of the Sto. Tomas II Copper-Gold Deposit located in Padcal, Tuba, Benguet Province, Philippines. R. C. Obial & Associates – Mining Geology, Exploration and Analytical Geochemistry, Pasig City, Philippines, 142p.

Ohmoto, H., & Rye, R. (1979). Isotopes of Sulfur and Carbon. *in* : Barnes, H. L. (ed.) Geochemistry of Hydrothermal Ore Deposits. 2nd edn. John Wiley, New York, 509-567.

Peña, R. E. (2008) Lexicon of the Philippine Stratigraphy. Geological Society of the Philippines, Mandaluyong City. 364p.

Philex Mining Corporation (2017) Annual Report 2017. Philex Mining Corporation, Mandaluyong City, 1-90.

Philex Mining Corporation (2018) Annual and Sustainability Report 2017. Philex Mining Corporation, Mandaluyong City, 1-122.

Pollard, P. J., and Taylor, R. G. (2002) Paragenesis of the Grasberg Cu-Au deposit, Irian Jaya, Indonesia: Results from logging section 13. Mineralium Deposita, 37, 117-136.

Pollard, P. J., Taylor, R. G., and Peters, L. (2005) Ages of Intrusion, Alteration, and Mineralization at the Grasberg Cu-Au Deposit, Papua, Indonesia. Econ. Geol., 100, 1005-1020.

Queaño, K.L., Ali, J. R., Milsom, J., Aitchison, J. C. and Pubellier, M. (2007) North Luzon and the Philippine Sea Plate motion model: Insights following paleomagnetic, structural, and age-dating investigations. Jour. Geophys. Res., 112, B05101, 1-44.

Rangin, C. (1991) The Philippine Mobile Belt: A complex plate boundary. Jour. SE Asian Earth Sci., 6, 209–220.

Roedder, E. (2002) Fluid Inclusions. *in* : Meyer, R. A. (ed.), Encyclopedia of Physical Science and Technology. 3rd edn. Academic Press, London, 71-77.

Sasaki, A. and Ishihara, S. (1979) Sulfur isotopic composition of magnetite-series and ilmenite-series granitoids in Japan. Contrib. Mineral. Petrol., 68, 107-115.

Seedorff, E., Dilles, J. H., Proffett, J. M., Jr., Einaudi, M. T., Zurcher, L., Stavast, W. A. and Barton, M. D. (2005) Porphyry deposits: Characteristics and origin of hypogene features. Econ. Geol., 100th Anniversary Volume, 251-298.

Seedorff, E. and Einaudi, M. (2004) Henderson porphyry molybdenum system Colorado: I. Sequence and abundance of hydrothermal mineral assemblages, flow paths of evolving fluids and evolutionary style. Econ. Geol., 99, 3-37.

Serafica, V. S. and Baluda, R. P. (1977) Geology of the Philex Sto. Tomas II orebody. 5th Symposium on Mineral Resource Development, (Paper 3). Baguio City.

Shepherd, T., Rankin, A. H. and Alderton, D. H. M. (1985) A Practical Guide to Fluid Inclusion Studies. Blackie, London, 239p.

Sillitoe, R. H. (2010) Porphyry copper systems. Econ. Geol., 105, 3-41.

Sillitoe, R. H. (2011) Exploration Potential of the Sto. Tomas Deeps and Nearby Porphyry Copper-gold Prospects, Philippines. Internal Report, Philex Mining Corporation, Pasig City, Philippines, 12p.

Sillitoe, R. H. and Gappe, I. M. Jr. (1984) Philippine Porphyry Copper Deposits: Geologic Setting and Characteristics. United Nations ESCAP CCOP Technical Publication, Bangkok, Thailand, 14, 89p.

Sterner, S., Hall, D. L. and Bodnar, R. J. (1988) Synthetic fluid inclusions. V. Solubility relations in the system NaCl-KCl-H2O under vapor-saturated conditions. Geochim. Cosmochim. Acta, 52, 989-1005.

Suerte, L. O., Nishihara, S., Imai, A., Watanabe, K., Yumul, G. P., Jr. and Maglambayan, V. B. (2007) Occurrences of ore minerals and fluid inclusion study on the Kingking porphyry copper-gold deposit, eastern Mindanao, Philippines. Resource Geol., 57, 219-229.

Takenouchi, S. (1980) Preliminary studies on fluid inclusions of the Santo Tomas II (Philex) and Tapian (Marcopper) deposits in the Philippines. *in* : Ishihara, S. and Takenouchi, S. (eds.), Granitic Magmatism and Related Mineralization. Mining Geol. Spec. Issue, 8, 141-150.

Tarkian, M. and Koopmann, G. (1995) Platinum-group minerals in the Santo Tomas II (Philex) porphyry copper-gold deposit, Luzon Island, Philippines. Mineral. Deposita, 30, 39-47.

Togashi, Y., Domingo, E. G., Sta. Cruz, J. R. and Nakagawa, M. (1990) K-Ar ages of intrusive rocks from the Santo Tomas II (Philex) gold-bearing porphyry copper deposit, Philippines. *in* : Professor Yukitoshi Urashima Commemoration

Volume on the Occasion of His Retirement, Organization of Professor Yukitoshi Urashima Retirement Ceremony, Kagoshima, 217–224.

Waters, P. J., Cooke, D. R., Gonzales, R. I. and Phillips, D. (2011) Porphyry and epithermal deposits and 40Ar/39Ar geochlonology of the Baguio District, Philippines. Econ. Geol., 106, 1335-1363.

Wolfe, J. A., Manuzon, M. S. and Divis, A. F. (1978) The Taysan porphyry copper deposit, southern Luzon Island, Philippines. Econ. Geol., 73, 608-617.

Wolfe, R. C. and Cooke, D. R. (2011) Geology of the Didipio region and genesis of the Dinkidi alkalic porphyry Cu-Au deposit and related pegmatites, northern Luzon, Philippines. Econ. Geol., 106, 1279-1315.

Yavuz, F. (2003) Evaluating micas in petrologic and metallogenic aspect: part II – applications using the computer program Mica^{+}. Comput. Geosci., 29, 1215-1228.

Yoneda, N. (2015) Geological Characteristics and Ore-forming Conditions of a New Ore-body at Deeper Portion of the Sto. Tomas II Porphyry Copper Deposit, Luzon, Philippines. Unpublished Bachelor Thesis, Akita University, Akita, Japan, 42p.